LINEAR TIME INVARIANT APPROXIMATIONS OF LINEAR TIME PERIODIC SYSTEMS FOR INTEGRATED FLIGHT AND VIBRATION CONTROL

A Dissertation
Presented to
The Academic Faculty

By

Mark Joseph Santos Lopez

In Partial Fulfilment
Of the Requirements for the Degree
Doctor of Philosophy in Aerospace Engineering

Georgia Institute of Technology

August 2016

Linear Time Invariant Approximations of Linear Time Periodic Systems for Integrated
Flight and Vibration Control

Approved by:

Dr. J.V.R. Prasad, Advisor
School of Aerospace Engineering
Georgia Institute of Technology

Dr. Lakshmi N. Sankar
School of Aerospace Engineering
Georgia Institute of Technology

Dr. Mark F. Costello
School of Aerospace Engineering
Georgia Institute of Technology

Dr. Mark B. Tischler
Aviation Development Directorate
U.S. Army RDECOM

Dr. Marc D. Takahashi
Aviation Development Directorate
U.S. Army RDECOM

Date Approved: May 20, 2016

To my parents and brother for all of their love and support

ACKNOWLEDGEMENTS

TABLE OF CONTENTS

LIST OF TABLES

LIST OF FIGURES

NOMENCLATURE

A LTI state matrix

B LTI input matrix

$b_{P_1,C}$ Generalized stability margin of the feedback connection $[P_1,C]$

C LTI output matrix

$c_{j,k,n}$ n^{th} harmonic coefficient of $V_{j,k}(t)$ in complex-exponential form

D LTI direct transmission matrix

$F(\psi)$ LTP state matrix

F_x Hub longitudinal shear

F_y Hub lateral shear

F_z Hub vertical shear

G_1 normalized right graph of P_1

$\tilde{G}_2$ normalized left graph of P_2

$G(\psi)$ LTP input matrix

H Dynamic crossfeed controller

J Cost function

K Feedback loop gain

M_x Hub lateral moment

M_y Hub longitudinal moment

M_z Hub torque

n_ω Number of frequency points used in cost function computation

$P(\psi)$ LTP output matrix

$R(\psi)$ LTP direct transmission matrix

T Transfer matrix relating HHC inputs to 4/rev loads

t Time (sec)

U LTI augmented input vector

u LTP input vector

$V_{j,k}(t)$ Periodic eigenvector element associated with the jth state and kth mode

W_g Relative weight for magnitude squared errors used in cost function computation

W_p Relative weight for phase squared errors used in cost function computation

W_γ Weighting function dependent on the coherence function used in cost function computation

X LTI augmented state vector

x LTP state vector

Y LTI augmented output vector

y LTP output vector

β Flapping angle

ΔZ Vertical displacement of the rotor hub

δ_{DR} Disturbance associated with disturbance rejection response

δ_g Gap metric

δ_v Nu-gap metric

ε Error-response function

η_k Floquet exponent associated with the kth mode

θ Blade pitch angle input

θ_0 Swashplate collective pitch input

θ_{1c} Swashplate lateral cyclic pitch input

θ_{1s} Swashplate longitudinal cyclic pitch input

Λ_k Characteristic multiplier associated with the kth mode

$\Phi(t)$ State transition matrix

$\phi_{j,k,n}$ Modal participation for n^{th} complex-exponential harmonic coefficient of $V_{j,k}(t)$

ψ Non-dimensional time, $\psi = \Omega t$

Ω Rotor rotational speed (rad/sec)

ω_1 Starting frequency used in cost function computation

ω_c Broken-loop crossover frequency

ω_{n_ω} Ending frequency used in cost function computation

Operator

$(\dot{\ })$ First derivative with respect to time

$[P_1, C]$ Feedback connection of P_1 with compensator C

$\|\cdot\|_\infty$ H_∞ norm

$|\ \ |$ Magnitude (dB)

$\angle$ Phase (deg)

$(\ )^*$ Conjugate transpose

$(\ )^+$ Pseudo inverse

x'_{nc} n^{th} cosine harmonic component of $\dot{x}$

x'_{ns} n^{th} sine harmonic component of $\dot{x}$

H_{oM} Average harmonic analysis operator of periodic matrix $M(\psi)$

H_{icM} i^{th} cosine harmonic analysis operator of periodic matrix $M(\psi)$

H_{isM} ith sine harmonic analysis operator of periodic matrix $M(\psi)$

Subscript

$()_0$ Average or 0th harmonic term

$()_{nc}$ n^{th} cosine harmonic component

$()_{ns}$ n^{th} sine harmonic component

Abbreviations

AFCS   Automatic flight control system

GM   Gain margin

HHC   Higher harmonic control

IBC   Individual blade control input

LTI   Linear time invariant

LTP   Linear time periodic

MTE   Mission task element

NL   Nonlinear

P2P   Peak-to-peak

PM   Phase Margin

PSD   Power spectral density

RMS   Root mean square

STD   Standard deviation

SUMMARY

Recent developments in active rotor control have shown significant coupling between flight and vibration control systems which are traditionally designed independently. This coupling results in performance degradation of the vibration controller particularly during maneuvering flight. Thus, an integrated flight and rotor control design is desired to address coupling and improve performance. Due to the strong periodic nature of rotorcraft at higher forward speeds, accurate models for rotorcraft must take the form of linear time periodic (LTP) models which are inconvenient for control design and handling qualities evaluations. Instead, linear time invariant (LTI) model approximations are desired, as they provide a convenient and well understood framework for analysis, control design, and handling qualities assessments. While LTI approximations for LTP systems have been recently developed to include states to represent the vibrations of the rotor harmonics, the fidelity of such LTI systems has not been well validated. Furthermore, the current formulation of a full LTI state space approximation relies on an LTP system which is in second order form; this presents difficulties for degrees of freedom not explicitly in second order form such as body and inflow degrees of freedom.

This work develops methodologies for assessing the fidelity of LTI approximations of LTP systems. Having a complete fidelity assessment, these LTI approximations are then used in the development and evaluation of a full flight envelope integrated flight and vibration reduction controller. This full flight envelope integrated

controller is evaluated in a nonlinear simulation using realistic piloted maneuvers. Specifically, this work accomplishes the following: 1) Development of a generalized LTI approximation of first order LTP models. 2) Verification of the LTI approximation against the original nonlinear model. 3) Evaluation of the fidelity of LTI system dynamics compared to LTP system dynamics using modal participation. 4) Formulation of reduced order models based on modal participation. 5) Evaluation of input-output fidelity of reduced order models using additive uncertainty, nu-gap metric, and generalized stability margin techniques. 6) Design and analysis of a single fixed point vibration controller, integrated with a stabilized flight control system, that is assessed using realistic maneuvers. 7) Robustness evaluations of the fixed point controller, and 8) Further improvements using controller scheduling to create a full flight envelope controller.

An example is given for each step using a UH-60A rotorcraft model in the context of development of an integrated flight and vibration controller.

CHAPTER 1. INTRODUCTION

1.1 Motivation

Active rotor control is an ongoing area of research which has been shown to allow vast improvements in many areas currently plaguing rotorcraft. Applications of active rotor control include improvements in power consumption, vibration reduction, noise reduction (Refs. 1 and 2), gust response alleviation, and reduction of blade vortex interactions (Ref. 3). This work focuses on the application to active vibration control. Implementations of active rotor control include: 1) swashplate higher harmonic control (HHC) where the swashplate is actuated at higher harmonic frequencies (Ref. 4), 2) individual blade control (IBC) where each blade input is actuated independently (Refs. 5 and 6), and on-blade control (OBC) where HHC inputs are created by actuators or devices on each blade – such as blade flaps or micro-flaps (Ref. 1). Although IBC and OBC implementations have the most promise, the HHC approach is effective and thus many active rotor controls rely on an HHC control system architecture (Ref. 1). The majority of previous work concentrates on the HHC itself and not its interaction with the automatic flight control system (AFCS). Although active rotor control has shown much promise, significant coupling between the AFCS and vibration control systems has been observed. Therefore, when the AFCS and vibration control system are designed independently, a resulting performance degradation of the latter may occur when they interact. This was demonstrated in flight tests (Ref. 7) and in analysis using linear

simulation models (Refs. 8 and 9), which showed significant performance degradation of vibration controllers using HHC during maneuvering flight.

To address coupling between the AFCS and active rotor control system while maintaining performance, an integrated flight and rotor control system is needed. To facilitate design of an integrated flight and rotor control system, models are needed which accurately capture both flight and rotor dynamics.

Due to the strong periodic nature of helicopter rotors, rotorcraft nonlinear (NL) models can often be linearized and represented by linear time periodic (LTP) models. These LTP models have matrix coefficients which are time varying but periodic with a period of one rotor revolution. There are several established techniques for analysis of linear time periodic (LTP) systems. One such method is Floquet Theory, developed by Gaston Floquet (Ref. 10). This theory has been shown to provide a thorough analysis of LTP system dynamics through the use of modal participation factors as by Peters and Lieb (Ref. 11). Modal participation factors describe the mode shapes (periodic eigenvectors) through the relative magnitude of each harmonic component for each state and mode. Although this theory has been shown to provide a thorough analysis of LTP systems (Ref. 11), they are still very inconvenient when trying to perform controller design or evaluate handling qualities. Therefore, a linear time invariant (LTI) model is still desired for both controller synthesis and handling qualities assessments because of the availability of numerous techniques to handle LTI systems.

1.2 Present Work

Analysis of LTP systems were also examined for discrete time systems using both LTP methods and LTI reformulation methods. Varga and Van Dooren discussed the stability analysis of discrete time periodic systems using the periodic Schur decomposition (Ref. 12). Bittanti, Colaneri, and Varga discussed linear time invariant reformulations using cyclic, Fourier, time and frequency lifting techniques (Refs. 13 and 14). Most recently, Lovera and Celi et al explored LTI reformulations of rotorcraft LTP systems for applications to active rotor control (Refs. 15 and 16).

In continuous time, an LTI model approximation can be formulated by expansion of the LTP system states into various harmonic state coefficients and formulating corresponding linear time invariant models. This harmonic decomposition of LTP states was first demonstrated by Hill for motions of the sun and moon (Ref. 17), with Crimi, Piarulli, and White being the first to do so for rotorcraft (Refs. 18 and 19).

Alternatively, Cheng, Tischler, and Celi (Ref. 8) developed a numerical method to directly extract an LTI model by including higher harmonic states from a nonlinear (NL) system. They accomplished this by making higher harmonic perturbations directly in a nonlinear simulation. While the LTI extracted using this direct higher harmonic perturbation method showed promise, the model used in the study was limited to rigid blades and a 3 state Pitt-Peters dynamic inflow model.

Most recently, Prasad and Olcer et al (Refs. 20-23) use a two-step approach for formulating an LTI model from a nonlinear system model. An accurate LTP model about a selected periodic equilibrium is obtained first, and then, an LTI model of selected order is constructed from the LTP model using the derived closed form expressions for the system matrices. The advantage of using this method is that it provides a means to

characterize the system as an LTI system, where controller synthesis and design methods are well understood.

The models developed by Prasad et al were studied and used in design by Friedmann et al (Ref. 24) for OBC implementations of HHC. In addition, Abraham et al (Ref. 9) used these LTI models to develop an integrated HHC/AFCS design through the use of dynamic crossfeeds.

Although the method developed by Prasad et al has shown success, the fidelity of the LTI approximations with respect to the LTP system has not been comprehensively addressed. Current studies of fidelity for these LTI approximations were primarily time response comparisons and eigenvalue comparisons, with some limited frequency response comparisons. Although the eigenvalue comparisons do give some indication of fidelity in terms of the system dynamics, a more thorough approach is needed. Previous time response comparisons may not adequately excite the full spectrum of the system dynamics, and previous frequency response comparisons were focused on body response and total loads which may not adequately reflect the richness of the rotor dynamics seen in vibratory response.

Furthermore, the formulation developed by Prasad et al relies on a second order formulation of the original LTP system. This second order formulation can prove problematic for degrees of freedom not explicitly represented in second order form. Specifically, difficulties arise when performing the harmonic decomposition of body and inflow states as well as interpretation of LTI model velocities. Thus, a more general formulation is desired in order to capture and study higher harmonic dynamics associated with degrees of freedom that are not explicitly in second order form. Once a generalized

4

LTI formulation has been developed, its fidelity can be assessed thoroughly using modal participation to evaluate system dynamics and also additive uncertainty techniques and nu-gap metric analysis to evaluate input-output fidelity.

Once the fidelity of these LTI approximations are studied, they will be used to develop an integrated flight and rotor control system at specific design flight speeds. This integrated flight and rotor control system design will address control interaction and improved performance. Full evaluation of each design point will be performed for performance and robustness with the original nonlinear model using realistic piloted maneuvers. These design point evaluations will then be used to develop a full flight envelope integrated flight and vibration controller using a speed schedule.

1.3 Objective

The purpose of this work is to develop methodologies for assessing the fidelity of LTI approximations of LTP systems, and then using them for integrated flight and rotor control design. Specifically, the following objectives are to be examined:

1) Develop a generalized linear time invariant (LTI) approximation of linear time periodic (LTP) models using first order form of the LTP model

2) Validate the linear time invariant approximation against the original nonlinear model

3) Evaluate the fidelity of LTI system dynamics compared to LTP system dynamics using modal participation

4) Formulate reduced order models for computational efficiency based on modal participation and state energy

5) Evaluate input-output fidelity of reduced order models

6) Develop a closed-loop HHC system based on a reduced order LTI approximation, and evaluate against the nonlinear (NL) model

7) Analyze the interactions between AFCS and HHC using piloted NL simulation maneuvers

8) Optimize closed-loop HHC performance using CONDUIT®

9) Develop dynamic crossfeeds to improve HHC performance during a maneuver

10) Evaluate the robustness of the improved HHC with respect to changes in flight condition, weight, and C.G. location

11) Develop a full flight envelope integrated flight and vibration controller using controller scheduling techniques

12) Verify improved HHC performance on a NL model with a realistic piloted maneuver

CHAPTER 2. LTI MODEL FORMULATION

2.1 LTI Formulation

In 2008, Prasad et al developed a process to approximate LTP state space models as a LTI state space models using harmonic decomposition techniques. This methodology was successfully used and studied in Refs. 9, 20-24. However, the fidelity of these models has not been comprehensively addressed. Furthermore, the method relied on a second order representation for the original LTP system, and extra work is required to address degrees of freedom not explicitly in second order form (e.g adding pseudo states or coming up with a mixed representation). An easier approach is used herein, where a first order representation for the LTP system is used to extract LTI approximations of LTP systems. This first order representation of the LTP system is more generic and allows for an overall simplified calculation since all states (displacements and velocities) are treated identically.

2.2 LTI Model Extraction

The LTI model extraction for an LTP model using the first order formulation is now discussed.

2.2.1 State Equation of the LTI Model

Consider a linear time periodic (LTP) model with the state equation given as

$$\dot{x} = F(\psi)x + G(\psi)u \tag{1}$$

An LTP model can be obtained from a nonlinear model using a perturbation scheme, linearizing about a periodic equilibrium at every azimuthal position (Ref. 20). In order to extract an approximate LTI model from Eq. (1), consider the following approximation of x:

$$x = x_o + \sum_{n=1}^{N} x_{nc} \cos n\psi + x_{ns} \sin n\psi \tag{2}$$

where x_o is the average component and x_{nc} and x_{ns} are respectively the n/rev cosine and sine harmonic components of x. Likewise, the control u is expanded in terms of harmonic components as

$$u = u_o + \sum_{m=1}^{M} u_{mc} \cos m\psi + u_{ms} \sin m\psi \tag{3}$$

Differentiation of Eq. (2) with respect to time results in

$$\dot{x} = \dot{x}_o + \sum_{n=1}^{N} x'_{nc} \cos n\psi + x'_{ns} \sin n\psi \tag{4}$$

where

$$x'_{nc} = \dot{x}_{nc} + n\Omega x_{ns} \qquad n = 1, 2, \dots, N \tag{5}$$

$$x'_{ns} = \dot{x}_{ns} - n\Omega x_{nc} \qquad n = 1, 2, \dots, N \tag{6}$$

Substituting Eq. (2) through Eq. (6) into Eq. (1) results in

8

$$\dot{x}_o + \sum_{n=1}^{N}(x'_{nc}\cos n\psi + x'_{ns}\sin n\psi) =$$

$$[F(\psi)](x_o + \sum_{n=1}^{N}(x_{nc}\cos n\psi + x_{ns}\sin n\psi)) \tag{7}$$

$$+[G(\psi)](u_o + \sum_{m=1}^{M}(u_{mc}\cos m\psi + u_{ms}\sin m\psi))$$

Equations for the individual harmonic components of x can be obtained by multiplying Eq. (7) on both sides by cos iψ or sin iψ, i= 1, 2, …, N, and integrating the result over one rotor revolution. The equation for the average component x_o is obtained by integrating Eq. (7) over one rotor revolution.

$$\dot{x}_o = \frac{1}{2\pi}\int_0^{2\pi} \{[F(\psi)](x_o + \sum_{n=1}^{N}(x_{nc}\cos n\psi + x_{ns}\sin n\psi))$$

$$+[G(\psi)](u_o + \sum_{m=1}^{M}(u_{mc}\cos m\psi + u_{ms}\sin m\psi))\}d\psi \tag{8}$$

Likewise, the equation for the ith harmonic cosine component x_{ic} can be obtained as

$$x'_{ic} = \frac{1}{\pi}\int_0^{2\pi} \{[F(\psi)](x_o + \sum_{n=1}^{N}(x_{nc}\cos n\psi + x_{ns}\sin n\psi))$$

$$+[G(\psi)](u_o + \sum_{m=1}^{M}(u_{mc}\cos m\psi + u_{ms}\sin m\psi))\}\cos i\psi d\psi \tag{9}$$

$$i = 1,2,3,.....,N$$

and the equation for the ith harmonic sine component x_{is} can be obtained as

$$x'_{is} = \frac{1}{\pi}\int_0^{2\pi} \{[F(\psi)](x_o + \sum_{n=1}^{N}(x_{nc}\cos n\psi + x_{ns}\sin n\psi))$$

$$+[G(\psi)](u_o + \sum_{m=1}^{M}(u_{mc}\cos m\psi + u_{ms}\sin m\psi))\}\sin i\psi d\psi \tag{10}$$

$$i = 1,2,3,.....,N$$

Using the following notation

9

$$F^{nc}(\psi) = F(\psi)\cos n\psi$$
$$F^{ns}(\psi) = F(\psi)\sin n\psi$$
$$G^{mc}(\psi) = G(\psi)\cos m\psi$$
$$G^{ms}(\psi) = G(\psi)\sin m\psi$$
$$n = 1, 2, 3, \ldots, N \qquad and \quad m = 1, 2, \ldots, M \tag{11}$$

and substituting Eq. (11) into Eqs. (8) – (10) yields

$$\dot{x}_o = \frac{1}{2\pi}\int_0^{2\pi}\{F(\psi)x_o + \sum_{n=1}^{N}(F^{nc}(\psi)x_{nc} + F^{ns}(\psi)x_{ns})$$
$$+ G(\psi)u_o + \sum_{m=1}^{M}(G^{mc}(\psi)u_{mc} + G^{ms}(\psi)u_{ms})\}d\psi \tag{12}$$

$$\dot{x}_{ic} = -i\Omega x_{is} + \frac{1}{\pi}\int_0^{2\pi}\{F(\psi)x_o + \sum_{n=1}^{N}(F^{nc}(\psi)x_{nc} + F^{ns}(\psi)x_{ns})$$
$$+ G(\psi)u_o + \sum_{m=1}^{M}(G^{mc}(\psi)u_{mc} + G^{ms}(\psi)u_{ms})\}\cos i\psi d\psi \tag{13}$$
$$i = 1, 2, 3, \ldots, N$$

$$\dot{x}_{is} = i\Omega x_{ic} + \frac{1}{\pi}\int_0^{2\pi}\{F(\psi)x_o + \sum_{n=1}^{N}(F^{nc}(\psi)x_{nc} + F^{ns}(\psi)x_{ns})$$
$$+ G(\psi)u_o + \sum_{m=1}^{M}(G^{mc}(\psi)u_{mc} + G^{ms}(\psi)u_{ms})\}\sin i\psi d\psi \tag{14}$$
$$i = 1, 2, 3, \ldots, N$$

Now defining the following operators

$$H_{oM} = \frac{1}{2\pi}\int_0^{2\pi}M(\psi)d\psi$$

$$H_{icM} = \frac{1}{\pi}\int_0^{2\pi}M(\psi)\cos i\psi d\psi \tag{15}$$

$$H_{isM} = \frac{1}{\pi}\int_0^{2\pi}M(\psi)\sin i\psi d\psi$$
$$i = 1, 2, 3, \ldots, N$$

Eqs. (12), (13), and (14) can be written as

$$\dot{x}_o = H_{oF} x_o + \sum_{n=1}^{N}(H_{oF^{nc}} x_{nc} + H_{oF^{ns}} x_{ns})$$
$$+ H_{oG} u_o + \sum_{m=1}^{M}(H_{oG^{mc}} u_{mc} + H_{oG^{ms}} u_{ms})$$

(16)

$$\dot{x}_{ic} = -i\Omega x_{is} + H_{icF} x_o$$
$$+ \sum_{n=1}^{N}(H_{icF^{nc}} x_{nc} + H_{icF^{ns}} x_{ns})$$
$$+ H_{icG} u_o + \sum_{m=1}^{M}(H_{icG^{mc}} u_{mc} + H_{icG^{ms}} u_{ms})$$
$$i = 1, 2, 3, \ldots, N$$

(17)

$$\dot{x}_{is} = i\Omega x_{ic} + H_{isF} x_o$$
$$+ \sum_{n=1}^{N}(H_{isF^{nc}} x_{nc} + H_{isF^{ns}} x_{ns})$$
$$+ H_{isG} u_o + \sum_{m=1}^{M}(H_{isG^{mc}} u_{mc} + H_{isG^{ms}} u_{ms})$$
$$i = 1, 2, 3, \ldots, N$$

(18)

2.2.2 Output Equation of LTI Model

Given the output equation of a LTP model as

$$y = P(\psi)x + R(\psi)u$$

(19)

an approximation to y in terms of its harmonic components is sought as

$$y = y_o + \sum_{l=1}^{L} y_{lc} \cos l\psi + y_{ls} \sin l\psi$$

(20)

11

where y_o is the average component and y_{lc} and y_{ls} are respectively the lth harmonic cosine and sine components of y. Substituting Eqs. (2), (3) and (20) into Eq. (19) results in

$$y_o + \sum_{l=1}^{L} y_{lc} \cos l\psi + y_{ls} \sin l\psi) =$$
$$[P(\psi)](x_o + \sum_{n=1}^{N} (x_{nc} \cos n\psi + x_{ns} \sin n\psi))$$
$$+ [R(\psi)](u_o + \sum_{m=1}^{M} (u_{mc} \cos m\psi + u_{ms} \sin m\psi))$$

(21)

Equation (21) is multiplied with $\cos l\psi$ or $\sin l\psi$, $l=0, 1, 2,..,L$ and is integrated over one rotor revolution, resulting in the following expressions for y_o, y_{lc} and y_{ls}.

$$y_o = \frac{1}{2\pi} \int_0^{2\pi} \{[P(\psi)](x_o + \sum_{n=1}^{N} (x_{nc} \cos n\psi + x_{ns} \sin n\psi))$$
$$+ [R(\psi)](u_o + \sum_{m=1}^{M} (u_{mc} \cos m\psi + u_{ms} \sin m\psi))\} d\psi$$

(22)

$$y_{lc} = \frac{1}{\pi} \int_0^{2\pi} \{[P(\psi)](x_o + \sum_{n=1}^{N} (x_{nc} \cos n\psi + x_{ns} \sin n\psi))$$
$$+ [R(\psi)](u_o + \sum_{m=1}^{M} (u_{mc} \cos m\psi + u_{ms} \sin m\psi))\} \cos l\psi d\psi$$
$$l = 1, \ 2, 3, ..., L$$

(23)

$$y_{ls} = \frac{1}{\pi} \int_0^{2\pi} \{[P(\psi)](x_o + \sum_{n=1}^{N} (x_{nc} \cos n\psi + x_{ns} \sin n\psi))$$
$$+ [R(\psi)](u_o + \sum_{m=1}^{M} (u_{mc} \cos m\psi + u_{ms} \sin m\psi))\} \sin l\psi d\psi$$
$$l = 1, 2, 3, ..., L$$

(24)

Using similar notation as before, for example, $P^{nc}=P(\psi)\cos n\psi$, etc., and the H operator, yields

$$y_o = H_{oP}x_o + \sum_{n=1}^{N}(H_{oP^{nc}}x_{nc} + H_{oP^{ns}}x_{ns})$$
$$+ H_{oR}u_o + \sum_{m=1}^{M}(H_{oR^{mc}}u_{mc} + H_{oR^{ms}}u_{ms}) \tag{25}$$

$$y_{lc} = H_{lcP}x_o + \sum_{n=1}^{N}(H_{lcP^{nc}}x_{nc} + H_{lcP^{ns}}x_{ns})$$
$$+ H_{lcR}u_o + \sum_{m=1}^{M}(H_{lcR^{mc}}u_{mc} + H_{lcR^{ms}}u_{ms}) \tag{26}$$
$$l = 1,2,3,......,L$$

$$y_{ls} = H_{lsP}x_o + \sum_{n=1}^{N}(H_{lsP^{nc}}x_{nc} + H_{lsP^{ns}}x_{ns})$$
$$+ H_{lsR}u_o + \sum_{m=1}^{M}(H_{lsR^{mc}}u_{mc} + H_{lsR^{ms}}u_{ms}) \tag{27}$$
$$l = 1,2,3,......,L$$

2.2.3   LTI Models in Matrix Form

Equations (16) – (18) and (25) – (27) can be represented in matrix form by defining the augmented state vector as

$$X = \begin{bmatrix} x_o{}^T ..x_{ic}{}^T & x_{is}{}^T ..x_{jc}{}^T & x_{js}{}^T .. \end{bmatrix}^T \tag{28}$$

and the augmented control vector as

$$U = \begin{bmatrix} u_o{}^T .. & u_{mc}{}^T & u_{ms}{}^T .... \end{bmatrix}^T \tag{29}$$

where x_o is the zeroth harmonic component, x_{ic}, x_{is} are the ith harmonic cosine and sine components of x, x_{jc}, x_{js} are the jth harmonic cosine and sine components of x, and u_{mc},

13

u_{ms} are the mth harmonic cosine and sine components of u, respectively. It is important to note that all states are considered individually (hence, a first order formulation); there is no difference in treatment between any kinematically related states such as in a second order formulation, where velocities and displacements are treated differently. The state equation of the resulting LTI model is

$$\dot{X} = [A]X + [B]U \tag{30}$$

Likewise, the augmented output vector of the LTI model is defined as

$$Y = \begin{bmatrix} y_o^T .. & y_{lc}^T & y_{ls}^T ... \end{bmatrix}^T \tag{31}$$

Then the output equation of the LTI model can be written as

$$Y = [C]X + [D]U \tag{32}$$

The LTI model matrices of Eqs. 30 and 32 are obtained as

$$A = \begin{bmatrix} H_{oF}...H_{oF^{ic}} & H_{oF^{is}}...H_{oF^{jc}} & H_{oF^{js}}.................... \\ .... \\ H_{icF}...H_{icF^{ic}} & -i\Omega + H_{icF^{is}}...H_{icF^{jc}} & H_{icF^{js}}......... \\ H_{isF}...i\Omega + H_{isF^{ic}} & H_{isF^{is}}....H_{isF^{jc}} & H_{isF^{js}}............. \\ .... \\ H_{jcF}...H_{jcF^{ic}} & H_{jcF^{is}}...H_{jcF^{jc}} & -j\Omega + H_{jcF^{js}}... \\ H_{jsF}...H_{jsF^{ic}} & H_{jsF^{is}}...j\Omega + H_{jsF^{jc}} & H_{jsF^{js}}... \\ .... \end{bmatrix} \tag{33}$$

$$B = \begin{bmatrix} H_{oG} \dots H_{oG^{mc}} & H_{oG^{ms}} \dots \\ \dots\dots\dots\dots\dots\dots\dots\dots\dots \\ H_{icG} \dots H_{icG^{mc}} & H_{icG^{ms}} \dots \\ H_{isG} \dots H_{isG^{mc}} & H_{isG^{ms}} \dots \\ \dots\dots\dots\dots\dots\dots\dots\dots\dots \\ H_{jcG} \dots H_{jcG^{mc}} & H_{jcG^{ms}} \dots \\ H_{jsG} \dots H_{jsG^{mc}} & H_{jsG^{ms}} \dots \\ \dots\dots\dots\dots\dots\dots\dots\dots\dots \end{bmatrix}$$

(34)

$$C = \begin{bmatrix} H_{oP} \dots H_{oP^{ic}} & H_{oP^{is}} \dots H_{oP^{jc}} & H_{oP^{js}} \dots \\ \dots\dots\dots\dots\dots\dots\dots\dots\dots\dots\dots\dots\dots \\ H_{lcP} \dots H_{lcP^{ic}} & H_{lcP^{is}} \dots H_{lcQ^{jc}} & H_{lcP^{js}} \dots \\ H_{lsP} \dots H_{lsP^{ic}} & H_{lsP^{is}} \dots H_{lsP^{jc}} & H_{lsP^{js}} \dots \\ \dots\dots\dots\dots\dots\dots\dots\dots\dots\dots\dots\dots\dots \end{bmatrix}$$

(35)

$$D = \begin{bmatrix} H_{oR} \dots H_{oR^{mc}} & H_{oR^{ms}} \dots \\ \dots\dots\dots\dots\dots\dots\dots\dots \\ H_{lcR} \dots H_{lcR^{mc}} & H_{lcR^{ms}} \dots \\ H_{lsR} \dots H_{lsR^{mc}} & H_{lsR^{ms}} \dots \\ \dots\dots\dots\dots\dots\dots\dots\dots \end{bmatrix}$$

(36)

where the LTI matrices can be expressed in closed form using linear combinations of the LTP matrix Fourier coefficients. These matrix Fourier coefficients can be computed via a fast Fourier transform method to avoid any issues of computation via integration.

2.2.4   Closed Form Expressions for LTI Model

Closed form expressions for various terms in the A, B, C and D matrices above can be obtained if one considers harmonic expansions of the LTP model matrices. If a time periodic matrix M(ψ) is expanded in terms of its harmonic components as

$$M(\psi) = M_o + \sum_{k=1}^{\infty}(M_{kc}\cos k\psi + M_{ks}\sin k\psi) \tag{37}$$

then it can be shown that

$$H_{oM} = \frac{1}{2\pi}\int_0^{2\pi}M(\psi)d\psi = M_o$$

$$H_{oM^{ic}} = \frac{1}{2\pi}\int_0^{2\pi}M(\psi)\cos i\psi\,d\psi = \frac{M_{ic}}{2} \tag{38}$$

$$H_{oM^{is}} = \frac{1}{2\pi}\int_0^{2\pi}M(\psi)\sin i\psi\,d\psi = \frac{M_{is}}{2}$$

$$i = 1,2\,3,.......$$

$$H_{icM} = \frac{1}{\pi}\int_0^{2\pi}M(\psi)\cos i\psi\,d\psi = M_{ic}$$

$$H_{isM} = \frac{1}{\pi}\int_0^{2\pi}M(\psi)\sin i\psi\,d\psi = M_{is} \tag{39}$$

$$i = 1,2\,3,.......$$

$$H_{icM^{jc}} = \frac{1}{\pi}\int_0^{2\pi}M(\psi)\cos j\psi\cos i\psi\,d\psi$$

$$= M_o + \frac{M_{kc}}{2}\quad for\ i = j\ where\ k = i + j$$

$$= \frac{M_{kc} + M_{lc}}{2}\quad for\ i \ne j\ and\ i > j$$

$$where\ k = i + j,\ \ l = i - j$$

$$= \frac{M_{kc} + M_{mc}}{2}\quad for\ i \ne j\ and\ j > i \tag{40}$$

$$where\ k = i + j,\ \ m = j - i$$

$$i = 1,2,..\ \ and\ \ j = 1,2,..$$

$$H_{icM^{js}} = \frac{1}{\pi} \int_0^{2\pi} M(\psi) \sin j\psi \cos i\psi \, d\psi$$

$$= \frac{M_{ks}}{2} \quad for \ i = j \ where \ k = i + j$$

$$= \frac{M_{ks} - M_{ls}}{2} \quad for \ i \neq j \ and \ i > j$$

$$where \ k = i + j, \ l = i - j$$

$$= \frac{M_{ks} + M_{ms}}{2} \quad for \ i \neq j \ and \ j > i$$

$$where \ k = i + j, \ m = j - i$$

$$i = 1,2,..and \ j = 1,2,....$$

(41)

$$H_{isM^{jc}} = \frac{1}{\pi} \int_0^{2\pi} M(\psi) \cos j\psi \sin i\psi \, d\psi$$

$$= \frac{M_{ks}}{2} \quad for \ i = j \ where \ k = i + j$$

$$= \frac{M_{ks} + M_{ls}}{2} \quad for \ i \neq j \ and \ i > j$$

$$where \ k = i + j, \ l = i - j$$

$$= \frac{M_{ks} - M_{ms}}{2} \quad for \ i \neq j \ and \ j > i$$

$$where \ k = i + j, \ m = j - i$$

$$i = 1,2,... \ and \ j = 1,2,....$$

(42)

$$H_{isM^{js}} = \frac{1}{\pi} \int_0^{2\pi} M(\psi) \sin j\psi \sin i\psi \, d\psi$$

$$= M_o - \frac{M_{kc}}{2} \quad for \ i = j \ where \ k = i + j$$

$$= \frac{M_{lc} - M_{kc}}{2} \quad for \ i \neq j \ and \ i > j$$

$$where \ k = i + j, \ l = i - j$$

$$= \frac{M_{mc} - M_{kc}}{2} \quad for \ i \neq j \ and \ j > i$$

$$where \ k = i + j, \ m = j - i$$

$$i = 1,2,.. \ and \ j = 1,2,..$$

(43)

The key difference between the newly presented first order formulation, Eqs. (30) and (32), and the previous second order formulation (Ref. 20) is the treatment of the velocity states. In the previous second order formulation, the LTI harmonic states associated with velocities are not directly the harmonic decomposition of the LTP velocity states. Rather, they are kinematically related via terms involving multiples of the rotor speed Ω as shown in Eqs. (5) and (6). Thus, to properly determine information about the LTP velocities, one would need to perform extra work to relate the LTI harmonic states and the harmonic decomposition of the LTP velocity states. In particular, to determine modal participation (Ref. 11) from the LTI appropriately, one would need to convert the LTI harmonic terms associated with velocities into the harmonic decomposition of the LTP velocities. Furthermore, since LTP body and inflow states do not readily come in the second order form required for the second order formulation (where the time derivatives of the displacement states are exactly given by the velocity states), extra work is again needed to transform those states into a usable form.

In the first order LTI formulation presented here, there is no difference in the treatment of LTP velocity and displacement states. This allows for an overall simplified calculation, and any information about LTP velocities can be given directly by the LTI states associated with velocities (such as modal participation of velocity states). Consequently, since there is no difference in treatment between any LTP states, this formulation easily encompasses body and inflow states which are often formulated in a more generalized first order form. Thus, this first order LTI formulation directly and efficiently approximates any LTP which can be cast in first order form.

2.3 LTI Numerical Example: UH-60A

2.3.1 Nonlinear Model

The model examined here is a full vehicle nonlinear (NL) model in FLIGHTLAB® (Ref 25.) The full vehicle model is a 4 bladed UH-60A with coupled elastic blade flap-lag degrees of freedom in multi blade coordinates (MBC) and a 33 state Peters-He dynamic inflow model. The model has previously been validated (Ref. 9) and been found to be consistent in the prediction of harmonic hub loads with trends from wind tunnel data. The NL is linearized at each azimuthal position with a discrete increment of 1.875 degrees of azimuth about a periodic equilibrium at 120 knots to generate an LTP model. The azimuth step size of 1.875 degrees is selected as a multiple of the default step size in FLIGHTLAB® which accurately captures at least the 8th harmonic terms.

The example here is considered in the context of N/rev vibration reduction. Specifically, for the 4 bladed rotor examined here, the objective of vibration reduction would be to reduce the 4/rev sine and cosine components of hub shears and hub moments except rotor torque ($F_{x4C}, F_{y4C}, F_{z4C}, M_{x4C}, M_{y4C}, F_{x4S}, F_{y4S}, F_{z4S}, M_{x4S}, M_{y4S}$). To achieve this, individual blade control (IBC) inputs are considered; specifically, the cosine and sine components of 3rd, 4th, and 5th harmonic individual blade controls (IBC3C, IBC3S, IBC4C, IBC4S, IBC5C and IBC5S) are the most effective at reducing 4/rev loads. The IBC inputs can be combined with swashplate inputs ($\theta_0, \theta_{1c}, \theta_{1s}$) to achieve the total pitch input for the kth blade $\theta^{(k)}$ as follows:

$$\theta^{(k)}(\psi^{(k)}) = \theta_0 + \theta_{1c}\cos(\psi^{(k)}) + \theta_{1s}\sin(\psi^{(k)})$$
$$+ \sum_{n=3}^{5}[IBCnC\cos(n\psi^{(k)}) + IBCnS\sin(n\psi^{(k)})] \tag{44}$$

2.3.2   LTI Model Validation

The full order LTI is extracted from the LTP using the first order methodology developed here, including the 0th up to the 24th harmonic states for each body, inflow, and rotor state resulting in a total of 3577 LTI states (LTI model referred to as LTIfull3577). The linear model is compared against the nonlinear model using the error-response functions ε, described by Tischler (Ref. 26), between linear and nonlinear model bare airframe (open-loop) responses. Specifically, the error-response ε is the difference between the truth (NL model) and the approximation (LTI model). The error response can be computed by sweeping each IBC input and comparing the resulting responses in the frequency domain using CIFER® (Ref. 26).

An example error-response plot is given in Figure 1 in capturing the transfer function of the LTP model from individual blade control, 4th harmonic cosine (IBC4C) input to the 4/rev cosine and sine components of vertical hub shear (F_{z4C} and F_{z4S} respectively) by the LTI model. These particular transfer functions would be most relevant to vibration reduction. It is important to note that while the HHC inputs are pitch variations that occur at 3Ω, 4Ω, and 5Ω, HHC systems normally operate with crossover frequencies ω_c between 1 and 3 rad/s. What this means is that for a 4/rev signal, the controller modulates the amplitude of a 4/rev signal at up to 3 rad/s. Thus, the actual frequency range of interest for the controller is 1 to 10 rad/s (approximately 3 times the maximum expected crossover frequency).

20

The mismatch bounds in the Figure 1 are known as the Maximum Unnoticeable Added Dynamics (MUAD) bounds. The MUAD bounds are used here as a guideline to indicate how much error can be tolerated without any significant changes in dynamics on a point wise frequency basis. Although the MUAD bound guidelines are based on flight-dynamics modeling, they are also used here as a guideline for the purposes of vibration controller design.

The error-response can also be measured using a single cost function as J described by Tischler (Ref. 26). The cost function J can be computed as

$$J = \frac{20}{n_\omega} \sum_{\omega_1}^{\omega_{n_\omega}} W_\gamma [W_g (|\varepsilon|)^2 + W_p (\angle \varepsilon)^2] \qquad (45)$$

where ε is the error-response function, ω_1 and ω_{n_ω} are the starting and ending frequencies used in the cost function computation, n_ω is the number of frequency points used in cost function computation, and W_g, W_p, W_γ are weights associated with the magnitude, phase, and coherence respectively. It is important to note that while

Guidelines for the cost function J are given as follows: $J < 100$ represents an acceptable level of accuracy for flight-dynamics modeling, while $J < 50$ is expected to produce a model that that is nearly indistinguishable from flight data (Ref. 26). These flight-dynamics modeling guidelines are also taken as guidelines here for the purposes of predicting vibratory hub loads. Here, the average cost function over all IBC input and 4/rev output transfer functions is 4.92, meaning that the LTIfull3577 data is nearly indistinguishable from the nonlinear model data.

At this point, the LTIfull3577 model has been validated to be nearly indistinguishable from the nonlinear model in terms of IBC inputs and 4/rev output transfer functions.
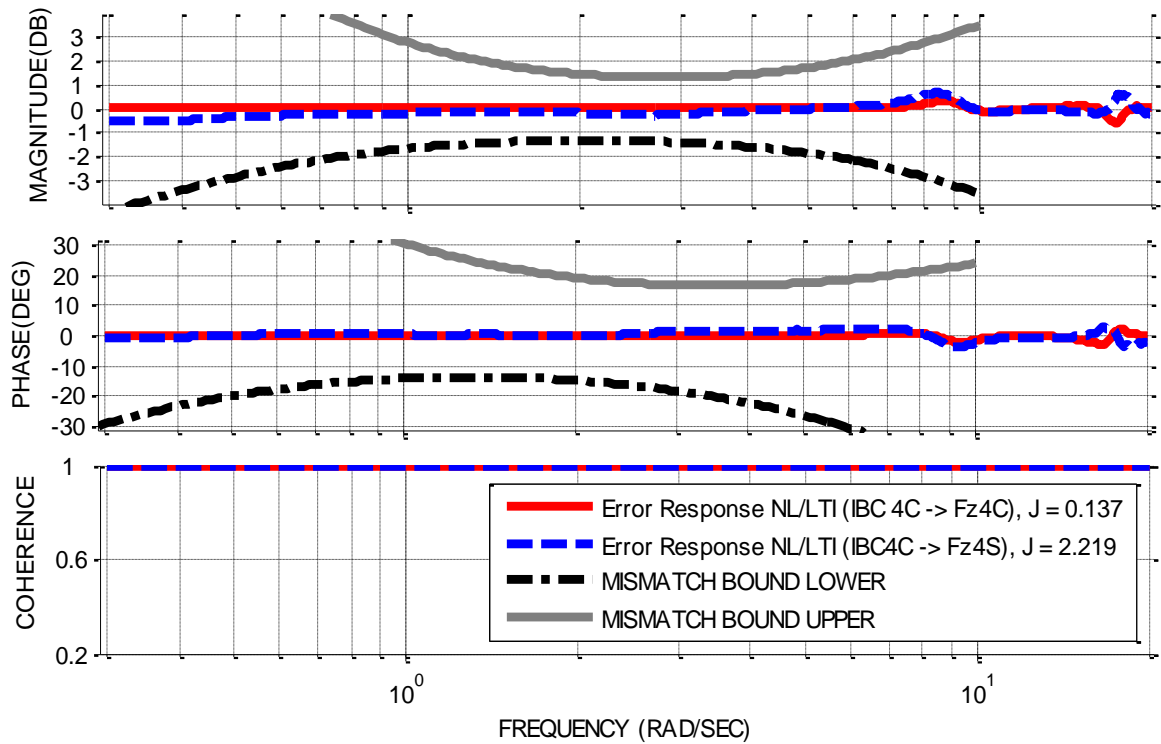
Figure 1. Error Response Plot for F_{z4C} and F_{z4S} for LTIfull3577

CHAPTER 3. MODAL PARTICIPATION

3.1 LTP Modal Participation

There are several established techniques for analysis of linear time periodic (LTP) systems. One such method is Floquet theory which has been shown to provide a thorough analysis of LTP system dynamics through the use of modal participation factors as discussed by Peters and Lieb (Ref. 11). Modal participation factors describe the mode shapes (periodic eigenvectors) through the relative magnitude of each harmonic component for each state and mode. Modal participation factors are also referred to as "modal participation" or "participation factors." The computation of modal participation using Floquet theory may involve bookkeeping and computational issues, although Peters and Leib have shown that the actual harmonic content described by modal participation is invariant of any bookkeeping choices made. One method for computation of modal participation using traditional Floquet theory can be done through the following steps (Ref. 11):

1) Consider an LTP model with the state equation given as

$$\dot{x} = F(t)x, \qquad F(t+T) = F(t) \tag{46}$$

where x, is the state vector, $F(t)$ is the system matrix of the periodic system and T is the period of the LTP system.

2) Compute the state transition matrix by solving the following matrix differential equation over one period

$$\dot{\Phi}(t) = F(t)\Phi(t), \qquad \Phi(0) = I \tag{47}$$

where I is the identity matrix. The state transition matrix evaluated at the end of one period is known as the Floquet transition matrix $\Phi(T)$.

3) Solve for the eigenvalues and eigenvectors of the Floquet transition matrix. The eigenvalues of the Floquet transition matrix are commonly known as the characteristic multipliers of the LTP system. The characteristic multiplier associated with the kth mode is denoted as Λ_k. The eigenvector matrix of the Floquet transition matrix is denoted as $V(T)$.

4) Compute the Floquet exponents and periodic eigenvectors. The Floquet exponents are also known as the characteristic exponents, Floquet system exponents, or system eigenvalues. The Floquet exponent associated with the kth mode η_k is computed as

$$\eta_k = \frac{1}{T} Log(\Lambda_k) \tag{48}$$

where the logarithm is a complex logarithm. The Floquet exponents have non-unique imaginary parts which come about as a result of a multivalued arctangent used in taking the complex logarithm of the characteristic multipliers. The periodic eigenvector matrix $V(t)$ can be computed as

$$V(t) = [\Phi(t)] [V(T)] \begin{bmatrix} \ddots & & \\ & \exp(-\eta_k t) & \\ & & \ddots \end{bmatrix} \qquad (49)$$

It should be noted that when the periodic eigenvector matrix $V(t)$ is evaluated at both $t = 0$ and $t = T$, the periodic eigenvector matrix is simply the eigenvector matrix of the Floquet transition matrix $V(T)$.

5) Expand each periodic eigenvector element into its corresponding complex Fourier series

$$V_{j,k}(t) = \sum_{n=-N_H}^{n=+N_H} c_{j,k,n} \exp(in\Omega t) \qquad (50)$$

where $V_{j,k}(t)$ is the periodic eigenvector element corresponding to the j$^{\text{th}}$ state and the k$^{\text{th}}$ mode, $c_{j,k,n}$ is the n$^{\text{th}}$ complex-exponential harmonic coefficient of $V_{j,k}(t)$, and N_H is the maximum harmonic term number used in the harmonic decomposition.

6) The modal participation is then the normalized magnitude of a particular harmonic (normalized with respect to the sum of the magnitudes of all harmonics for that particular state and mode)

$$\phi_{j,k,n} = \left| c_{j,k,n} \right| \left(\sum_{l=-N_H}^{l=+N_H} \left| c_{j,k,l} \right| \right)^{-1} \qquad (51)$$

Computation of the state transition matrix and Floquet transition matrix themselves can involve integrating the matrix differential equation, Eq. (47). This process itself may introduce computational errors and may also result in ill-conditioned

25

state and Floquet transition matrices. An ill-conditioned state transition matrix can result in inaccuracies in the Floquet exponents and periodic eigenvectors. These numerical errors can be mitigated by instead using fast Floquet theory (Refs. 27 and 28), which can reduce time over which Eq. (47) is integrated from T to $\dfrac{T}{N_B}$, where N_B is the number of blades. Furthermore, singular value decompositions (Ref. 27) can be also used to reduce spurious eigenvalues of heavily damped modes.

Besides numerical issues, computing the Floquet exponents can involve a complex logarithm (multivalued arctangent) of the characteristic multipliers that introduces bookkeeping issues (Ref. 11). Specifically, the imaginary part of the Floquet exponents can be shifted by any integer multiple of Ω. Adding multiples of Ω does not change the actual harmonic content of each mode, rather it is a bookkeeping decision that simply affects the naming of each harmonic term. Often, the bookkeeping integer choice is selected as one that best suits the mode of interest.

Alternatively, LTI can also be used to directly compute the LTP modal participation, which is simpler and avoids many of the issues that may be encountered in the Floquet method.

3.2 LTI Modal Participation

Once the LTI state matrix has been formed, the modal participation can be computed by the following procedure:

1) Solve for the eigenvectors and eigenvalues of the LTI state matrix A. X_k is the eigenvector corresponding to the kth mode which will be in the form

$$X_k = \left[x_{k,o}{}^T .. x_{k,nc}{}^T \quad x_{k,ns}{}^T \right]^T \tag{52}$$

where $x_{k,o}$ is the zeroth harmonic component, and $x_{k,nc}$, and $x_{k,ns}$ are the nth harmonic cosine and sine components of the periodic eigenvector corresponding to the kth mode $V_k(t)$. The eigenvalues of the A matrix are equavelent to the Floquet exponents of the LTP system (hence the alternative name: system eigenvalues).

2) Convert eigenvector harmonic states from real-trigonometric Fourier coefficients into complex-exponential Fourier coefficients

3) The modal participation is then the normalized magnitude of a particular harmonic (normalized with respect to the sum of the magnitudes of all harmonics for that particular state and mode)

Once the LTI eigenvectors X_k have been computed, the LTI eigenvector components are the harmonic components of the LTP periodic eigenvector. It is important to note that while the LTI model is formulated using real-trigonometric harmonic series in Eq. (2), modal participation is evaluated using a complex-exponential harmonic series in Eq. (50). Thus, to compute modal participation, the Fourier coefficients should be in the complex-exponential form in Eq. (50). The LTI eigenvector harmonic states can be converted from real-trigonometric to complex-exponential form via the following equations:

$$c_{j,k,+0} = x_{j,k,+0} \tag{53}$$

27

$$c_{j,k,+n} = \frac{x_{j,k,nc} - i\, x_{j,k,ns}}{2} \tag{54}$$

$$c_{j,k,-n} = \frac{x_{j,k,nc} + i\, x_{j,k,ns}}{2} \tag{55}$$

where $x_{j,k,+0}$, $x_{j,k,nc}$, and $x_{j,k,ns}$ are respectively the 0th, n^{th} cosine, and n^{th} sine real-trigonometric harmonic LTI eigenvector elements corresponding to the jth LTP state and k^{th} mode.

Once the complex-exponential harmonic coefficients have been obtained, the modal participation can then be directly computed via the definition of modal participation in Eq. (51).

It should be noted that the LTI modes corresponding to system eigenvalues with imaginary parts between $\pm \dfrac{\Omega}{2}$ are referred to as the base modes. These base modes are equivalent to taking the principal Arctangent and not adding any multiples of Ω to the imaginary part of the Floquet exponents in the Floquet method. Only the base modes are needed to completely describe the system with the understanding that higher frequency modes simply shift the naming of harmonics and do not affect the actual modal participation content; this is equivalent to book keeping issues of adding integer multiples of Ω to the imaginary part of Floquet exponents in the Floquet method. This is advantageous over the Floquet method in that instead of making a bookkeeping decision for the integer multiple to add to the Floquet exponent before any eigenvector analysis is performed, the LTI method computes all valid Floquet exponents (system eigenvalues) and the corresponding eigenvectors. Thus one can simply select the mode with the

corresponding imaginary part that is most relevant since all modes have already been computed.

3.3 Modal Participation Analytical Example

For illustrative purposes, simplified rotor blade flapping of a single blade is examined here. The modal participation of this example has been previously examined using the Floquet method by Peters and Leib (Ref. 11). Here, the modal participation computed using the LTI methodology is compared with the Floquet method results. The equation of motion for rotor blade flapping is given by

$$\ddot{\beta}(t) + C(t)\dot{\beta}(t) + K(t)\beta(t) = 0 \tag{56}$$

$$C(t) = \frac{\gamma}{8}\left[1 + \frac{4\mu}{3}\sin(t)\right] \tag{57}$$

$$K(t) = p^2 + \frac{\gamma}{8}\left[\frac{4\mu}{3}\cos(t) + \mu^2\sin(2t)\right] \tag{58}$$

where $\beta(t)$ is the flapping angle, γ is the Lock number, μ is the advance ratio, and p is the non-dimensional blade flapping frequency. For illustrative purposes, a Lock number γ of 12 and a flapping frequency p of 1.0 is used, with advance ratio μ varying from 0 to 3.

The modal participation was computed using both the Floquet method and the LTI method. Figure 2 shows the flapping angle modal participation for harmonics 0 through 4 as they change with advance ratio. Each harmonic term is indicated by

29

brackets labelling each line segment. For example, the line segment labeled [+0] for advance ratios 0 to 0.3 corresponds to the modal participation of the +0 harmonic term for $\beta(t)$. At advance ratio 0.3, the branches labeled [+0] and [-1] merge. For advance ratios 0.3 to 0.9, the branch labeled [-1/+0] indicates the same modal participation for both -1 and +0 harmonic terms. Both -1 and +0 are the harmonics with the highest modal participation for advance ratios from 0.3 to 0.9. At advance ratio 0.9, the -1 and +0 harmonics separate, and the +0 harmonic continues on by itself for advance ratio 0.9 to 3 as indicated by the [+0] label.

In Figure 2, the solid lines correspond to the Floquet method results, the circles correspond to the LTI method results, and colors correspond to particular harmonic numbers. For every point, the LTI and LTP methods result in nearly the same modal participations as shown by the circles (LTI method) laying on top of the solid line (LTP method). This indicates that the LTI method can be used to compute modal participation as accurately as the LTP method.
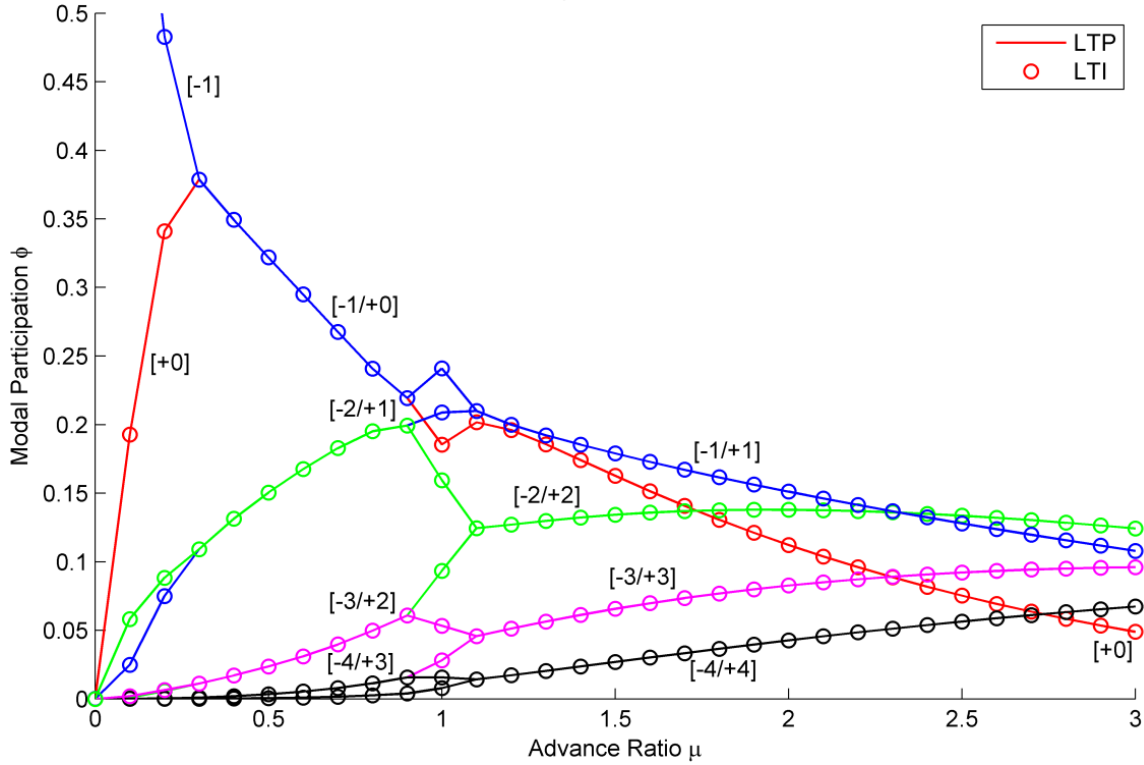
Figure 2. Modal Participation ϕ for Rotor Blade Flapping

3.4 Modal Participation Numerical Example

For the UH-60A, the modal participations were computed for each state, each harmonic term, and each mode using both Floquet theory and the LTI direct method presented here. Each of the 73 modes were examined and found to have similar trends. For brevity, only 5 sample modes are shown here. These 5 sample modes reflect the modal participation trends seen in all 73 modes. The modal participation is shown for rotor coning state in Figure 3 as computed both by the LTP and LTI methods. For a 4

bladed rotor, the harmonics with the highest modal participation are the 0th, 1st, and even numbered harmonics up to 8.

An example for reading the modal participation in Figure 3 is as follows: the top sub-plot shows the modal participation for mode 61, for the rotor coning state, for harmonics -12 through +12. The modal participation for rotor coning state, mode 61, +2 harmonic is 0.5; the modal participation for rotor coning state, mode 61, -2 harmonic is 0.4. Mode 61 and mode 62 are complex conjugate pairs, so the modal participations are reflected across the 0th harmonic (positive and negative harmonics are interchanged). Hence, as shown in the sub-plot second from the top in Figure 3, the modal participation for rotor coning state, mode 62, -2 harmonic is 0.5, and the modal participation for rotor coning state, mode 62, +2 harmonic is 0.4. Also, the LTI and LTP computations result in nearly identical rotor coning modal participations, indicating that the LTI captures modal participation as accurately as the LTP.

The modal participation for average inflow state is shown in Figure 4 and the modal participation for pitch attitude is shown in Figure 5. Again, the LTI and LTP computations show similar results, indicating that the LTI captures modal participation to be very close to that of the LTP. It is clear that similar to rotor degrees of freedom, body and inflow degrees of freedom also have contributions from harmonics 0, 1, and even numbered harmonics up to 8 (i.e. harmonics 0, 1, 2, 4, 6, and 8). These trends were observed for all modes and for every rotor, body, and inflow state. Thus, it is clear that in addition to rotor harmonics, body and inflow harmonics are important and need to be included in the LTI approximation.
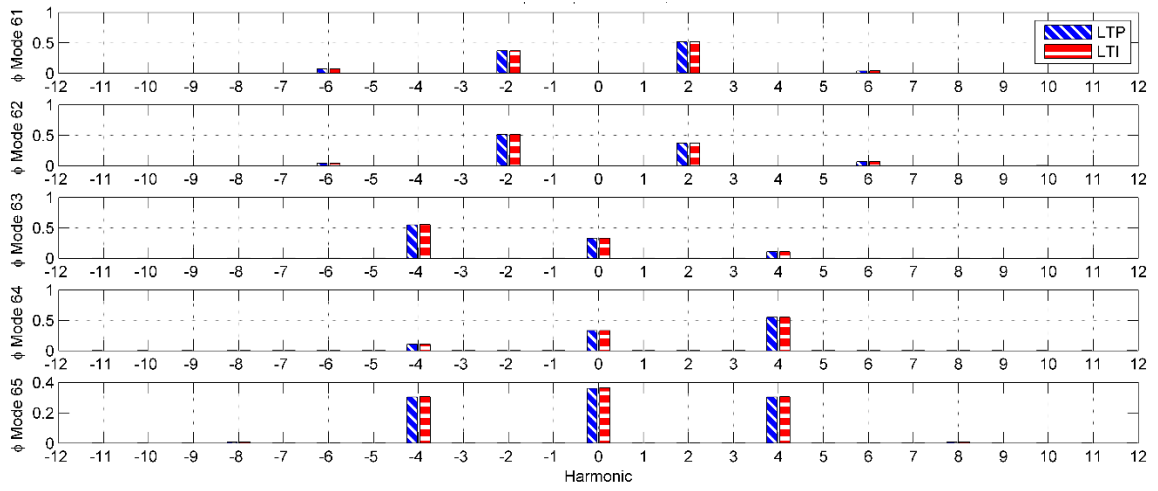
Figure 3. Modal Participation ϕ for Rotor Coning State
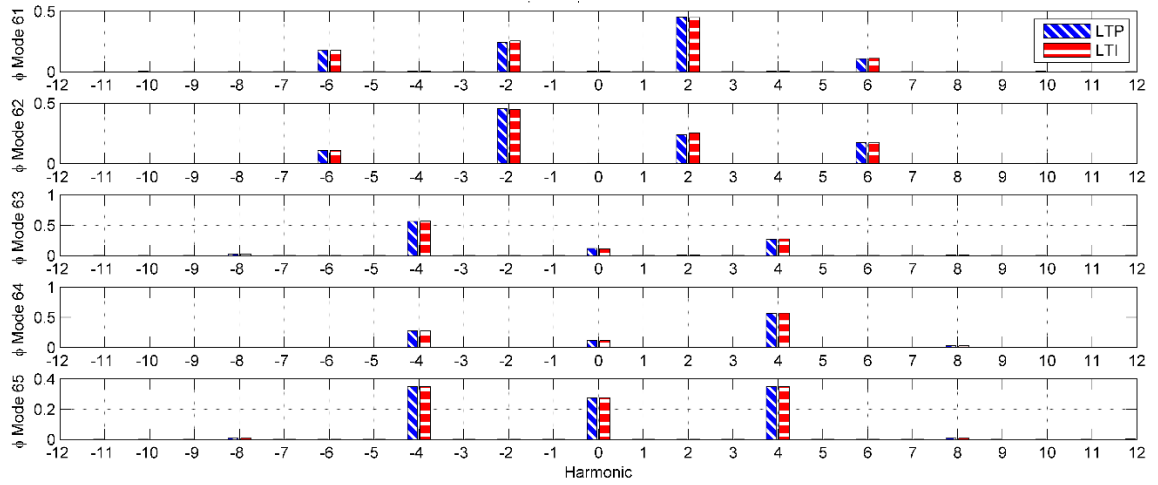
Figure 4. Modal Participation ϕ for Average Inflow State

33

Figure 5. Modal Participation ϕ **for Pitch Attitude**

CHAPTER 4. INPUT-OUTPUT FIDELITY

At this point, two different evaluation techniques have been used to analyze the LTI model. The error response and cost functions have been used to show that the LTIfull3577 model is nearly indistinguishable from the nonlinear model in terms of IBC inputs and 4/rev output transfer functions. Having shown that the LTIfull3577 model is accurate, modal participation is then used as an indication of which harmonic terms are important for each state.

Often for control design, state information itself is not necessary, but rather the input-output fidelity is what is important. This can be characterized using error response functions as shown previously, which indicate the relative differences or errors between two bare airframe (open-loop) models. Alternatively, the bare airframe frequency responses themselves can be compared, which also provides insight on the actual transfer functions themselves. In addition, metrics such as the normalized additive error (Ref. 29) from additive uncertainty analysis and the nu-gap metric (Ref. 30) can be computed directly from the open-loop frequency responses and used to evaluate input-output fidelity. In contrast to error response and cost functions which indicate bare airframe fidelity, normalized additive error and nu-gap metric focus on fidelity with respect to controller synthesis and design.

4.1 Normalized Additive Error

Although for the examples presented in this work the LTI reduction was formed using the methodology previously described, all of the input-to-output fidelity analysis described in this paper can be performed to compare any full and reduced LTI models irrespective of how the reduced LTI model was formed from the full LTI model. In fact, one could use the input-to-output fidelity as a basis for the LTI model order reduction itself. However, in this study the modal participation criterion is first applied to obtain a reduced order LTI model and then the resulting reduced LTI model is analyzed for input-to-output model fidelity.

Once an LTI reduction has been selected, the input-to-output fidelity of the reduced LTI model can be compared to the full LTI model by considering the normalized additive error to be the normalized additive uncertainty (Ref. 29). The full LTI model is considered as the truth model and the reduced LTI model is considered as the approximation. Additive uncertainty is used because the truth model is known. Although the normalized additive error can be calculated for a multiple input and multiple output (MIMO) system, here it is calculated for a single input and a single output (SISO) using the H_∞ norm of the difference between the full and reduced LTI models normalized by the H_∞ norm of the full LTI model:

$$Normalized\ Additive\ Error = \frac{\left\|P_1 - P_2\right\|_\infty}{\left\|P_1\right\|_\infty} \tag{59}$$

where, P_1 is the full LTI model transfer function, P_2 is the reduced LTI model transfer function, and $\left\|\cdot\right\|_\infty$ is the H_∞ norm.

The normalized additive error is interpreted to be a measure of the percentage difference between the full and reduced LTI models. A small error corresponds to full and reduced LTI models being close. The additive uncertainty value so obtained can form the basis for additional controller robustness to be considered in the design process.

4.2 Nu-Gap Metric

The nu gap metric is used to evaluate the change in generalized stability margin between the full and reduced LTI systems (Ref. 30). The nu-gap metric δ_v is defined as follows:

$$\delta_v(P_1, P_2) = \begin{cases} \left\| \tilde{G}_2 G_1 \right\|_\infty & \text{if } \det(G_2^* G_1)(j\omega) \neq 0 \forall \omega \in (-\infty, \infty) \text{ and } wno \det(G_2^* G_1) = 0 \\ 1 & otherwise \end{cases} \quad (60)$$

where wno(g) denotes the winding number about the origin of g(s), as s follows the standard Nyquist D-contour. G_1 is the normalized right graph of P_1 and $\tilde{G}_2$ is the normalized left graph of P_2. Alternatively, the nu gap metric can be computed directly from the transfer function matrices without the normalized coprime factorization or graphs. This can be done through the following relations:

$$\kappa(P_1, P_2) = \tilde{G}_2 G_1 \quad (61)$$

$$\kappa(P_1, P_2) = [I + P_2 P_2^*]^{-\frac{1}{2}} [P_1 - P_2][I + P_1^* P_1]^{-\frac{1}{2}} \quad (62)$$

37

where $P^*(s) = P^T(-s)$ for real rational $P(s)$ which is the case here. Similarly, the winding number condition for $\delta_v(P_1, P_2) < 1$ can also be formulated in an alternative manner and is easier to compute:

$$\det(I + P_2^* P_1) \neq 0 \forall \omega \tag{63}$$

$$wno \det(I + P_2^* P_1) + \eta(P_1) - \eta(P_2) - \eta_0(P_2) = 0 \tag{64}$$

Here, the winding number condition is formed into the requirement of both Eqs, (63) and (64) to be satisfied for $\delta_v(P_1, P_2) < 1$. Like the normalized additive error, the nu gap metric can be computed as a MIMO system, but it is computed here as a SISO system. The nu gap metric calculation can be further simplified for the SISO case as

$$\|\kappa(P_1, P_2)\|_{\infty, SISO} = \frac{\sup}{\omega} \frac{|P_1(j\omega) - P_2(j\omega)|}{\sqrt{1 + |P_1(j\omega)|^2} \sqrt{1 + |P_2(j\omega)|^2}} \tag{65}$$

The nu gap metric is a number from 0 to 1 where 0 corresponds to the models being close (Ref. 30). It is bounded from above by the gap metric δ_g, which can be useful if there is numerical difficulty in calculating the nu gap metric. The nu gap metric relates the generalized stability margins through the following inequality:

$$\arcsin b_{P_2, C} \geq \arcsin b_{P_1, C} - \arcsin \delta_v(P_1, P_2) \tag{66}$$

where $b_{P_i, C}$ is the generalized stability margin of the feedback connection of P_i with compensator C, $[P_1, C]$.

It is clear from Eq. (66) that if the nu gap metric between P_1 and P_2 is small, then any compensator designed to stabilize P_2 will also stabilize P_1 since the change in generalized stability margin will be small. It is common to consider that a gap metric less than 1/3 corresponds to the models being close. Any input-to-output mappings with small nu gap metrics would be good candidates for closing loops for feedback. Any input-to-output mappings with comparatively larger nu gap metric would need additional stability margin designed into the compensator for closing feedback loops.

4.3 Open versus Closed Loop Validation

It is important to note that although both normalized additive error and nu-gap metric measure differences in the input-output characteristics of two systems, the characteristics that they measure are not the same. The nu-gap metric is a measure of the loss of stability margin between the two systems, and thus is related to the closed loop behavior of the two systems. The normalized additive error is associated only with the open loop behavior of the two systems, and hence, can provide a basis for additional controller robustness to be considered in the design process. A small normalized additive error would indicate that the open loop behaviors of the two systems are similar. On the other hand, a small nu-gap metric indicates that there is minimal change in generalized stability margin, thus closed loop behaviors of the two are similar; that is to say, any controller that stabilizes one will also stabilize the other. It has been shown in Ref. 30 that closeness in one measure does not imply the closeness in the other measure, thus both should be considered to evaluate the full input-output characteristics. This is demonstrated in Figure 6, where P_0 and P_2 behave similarly in open loop, but very

differently in closed loop. The normalized additive error between P_0 and P_2 (taking P_0 as the truth model) is 1 and the nu-gap is 0.8988. The nu-gap of 0.8988 is very large, which is reflected in the very different closed loop behaviors. In addition, P_0 and P_1 behave very similarly in closed loop, but very differently in open loop. The normalized additive error between P_0 and P_1 (taking P_0 as the truth model) is 2, which is larger than the normalized additive error between P_0 and P_2 and results in very different open loop behaviors. The nu-gap between P_0 and P_1 is 0.02 which is very small and is reflected in the very different closed loop behaviors. Thus, both open and closed loop fidelity needs to be evaluated.
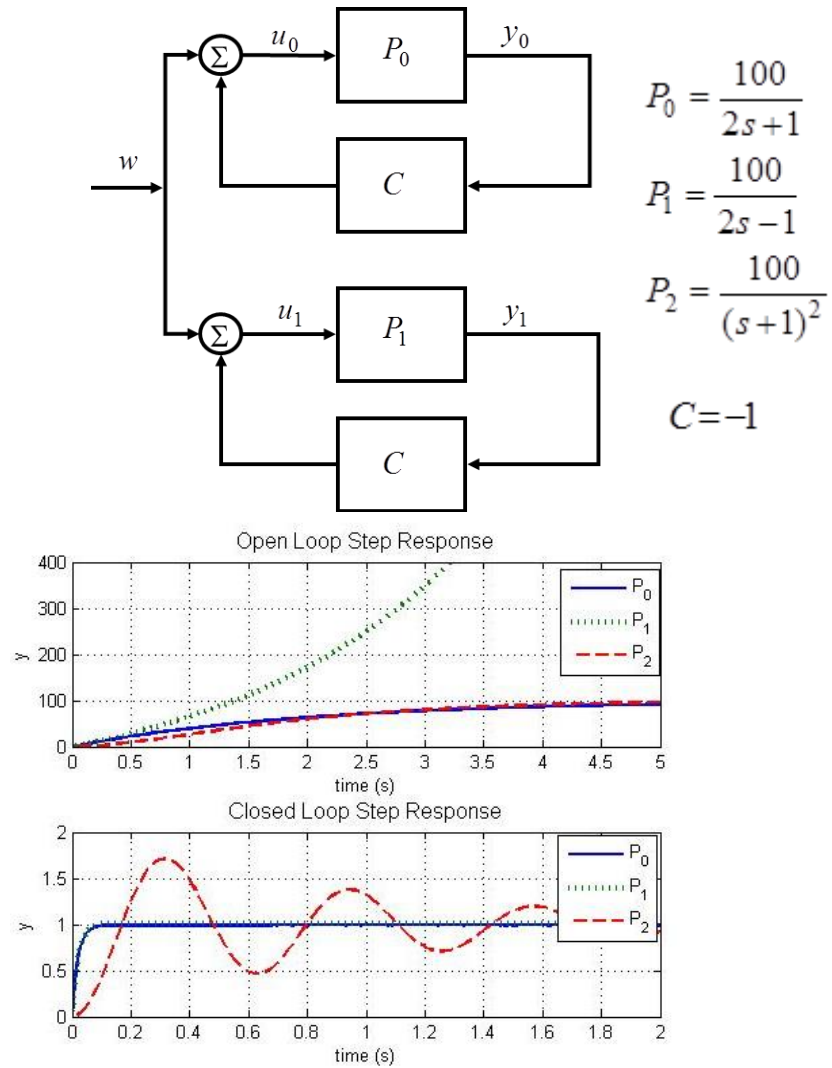
Figure 6. Example Open versus Closed Loop Response from Vinnicombe (Ref. 30)

## 4.4 Model Reduction and Input-Output Fidelity Example

Looking again to the UH-60A model, the significance of particular harmonic states can then be evaluated by comparing the full model LTIfull3577 with reduced LTI models that do not include particular harmonic states. The first reduction is formed by excluding the least significant harmonics, as shown by the modal participation evaluations.

41

Specifically, harmonics 3, 5, 7, 9 and all above 9 are removed. The resulting LTI retains the 0th, 1st, and 2-8 even numbered harmonics of all body, inflow and rotor states, resulting in 803 states (referred to as LTIred803). The second reduction is formed by starting with LTIred803 and removing any body harmonic states. The resulting LTI has only 723 states (referred to as LTIred703) and contains only the 0th harmonic body states, and the 0th, 1st, and 2-8 even numbered harmonic inflow and rotor states. The third reduction is formed by starting with LTIred803 and removing any inflow harmonic states. The resulting LTI has only 473 states (referred to as LTIred473) and contains only the 0th harmonic inflow states, and the 0th, 1st, and 2-8 even numbered harmonic body and rotor states. Finally, the fourth reduction is formed by starting with LTIred803 and removing both body and inflow harmonic states. The resulting LTI has only 393 states (referred to as LTIred393) and contains only the 0th harmonic body and inflow states, and the 0th, 1st, and 2-8 even numbered harmonic rotor states.

The frequency responses for the various LTI model approximations considered above are used in evaluating the individual model fidelity. For example, comparisons of bare airframe frequency responses from various LTI model approximations from IBC4C input to hub force and moment outputs F_{x4C}, F_{y4C}, F_{z4C}, M_{x4C}, and M_{y4C} are shown in Figures 7, 8, 9, 10 and 11, respectively. For all of the frequency responses examined, LTIred803 is nearly indistinguishable from LTIfull3577. Thus it is clear that in this case, any harmonic terms 3, 5, 7, 9 and any above 9 do not significantly influence overall model fidelity. Comparing LTIred723 with LTIfull3577, there is a maximum of a 3 dB difference in magnitude at 6 rad/s for F_{x4C}, and otherwise a maximum of 1 dB differences in magnitude over all frequency responses examined. Comparing LTIred473

with LTIfull3577, for M_{y4C} there is a maximum difference of 26 dB at 16 rad/s, and for all other outputs a maximum of 9.5 dB differences in magnitude below 7 rad/s, and 2.5 dB differences above 7 rad/s. Comparing LTIred393 with LTIfull3577, differences are similar to those from LTIred473 with M_{y4C} having a maximum difference of 26 dB at 16 rad/s, and for all other outputs a maximum of 10 dB differences in magnitude below 7 rad/s, and 2.5 dB differences above 7 rad/s. Thus, it is clear that inclusion of harmonics terms for both body and inflow states are important, although body harmonic terms less so than inflow harmonic terms.
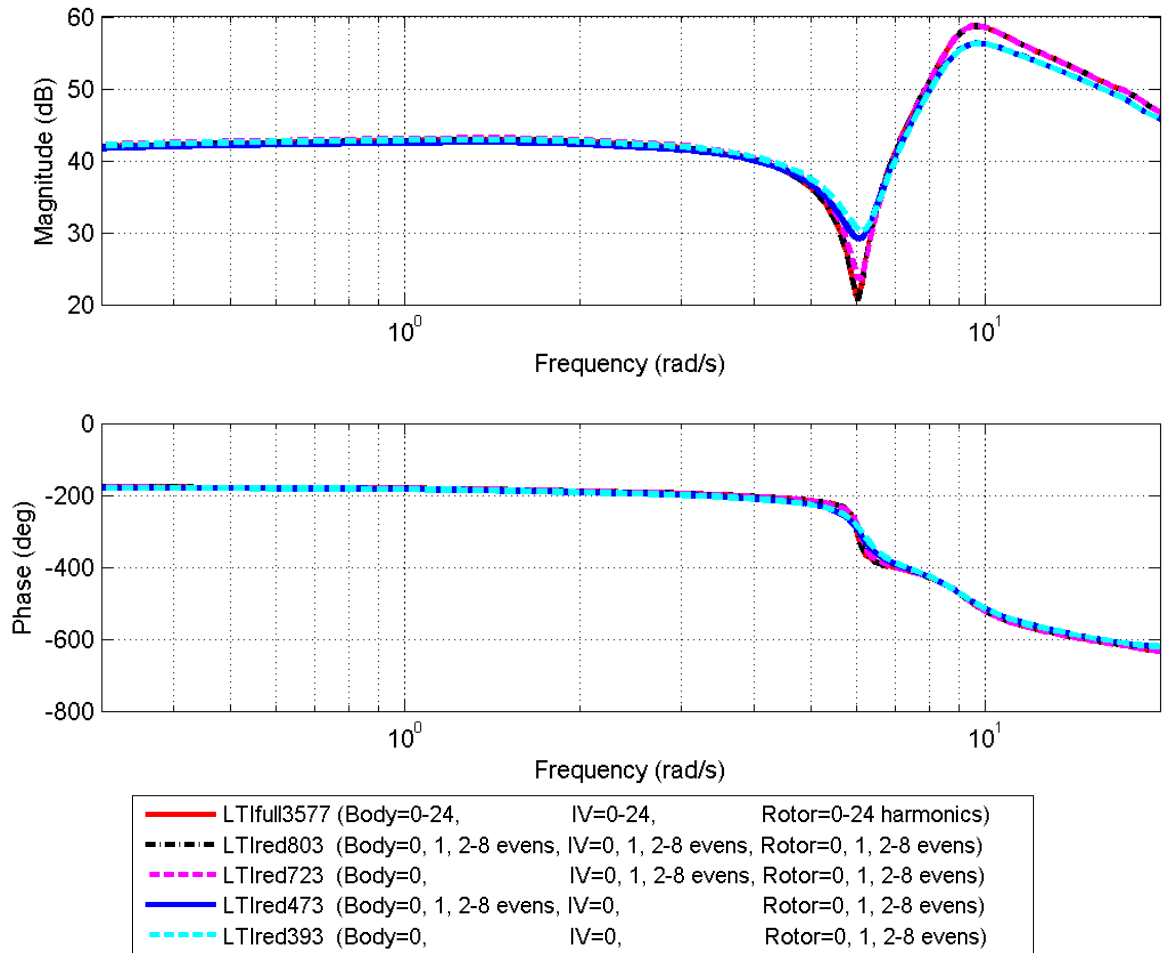
Figure 7. Frequency Response Comparison for IBC4C to F_{x4C}
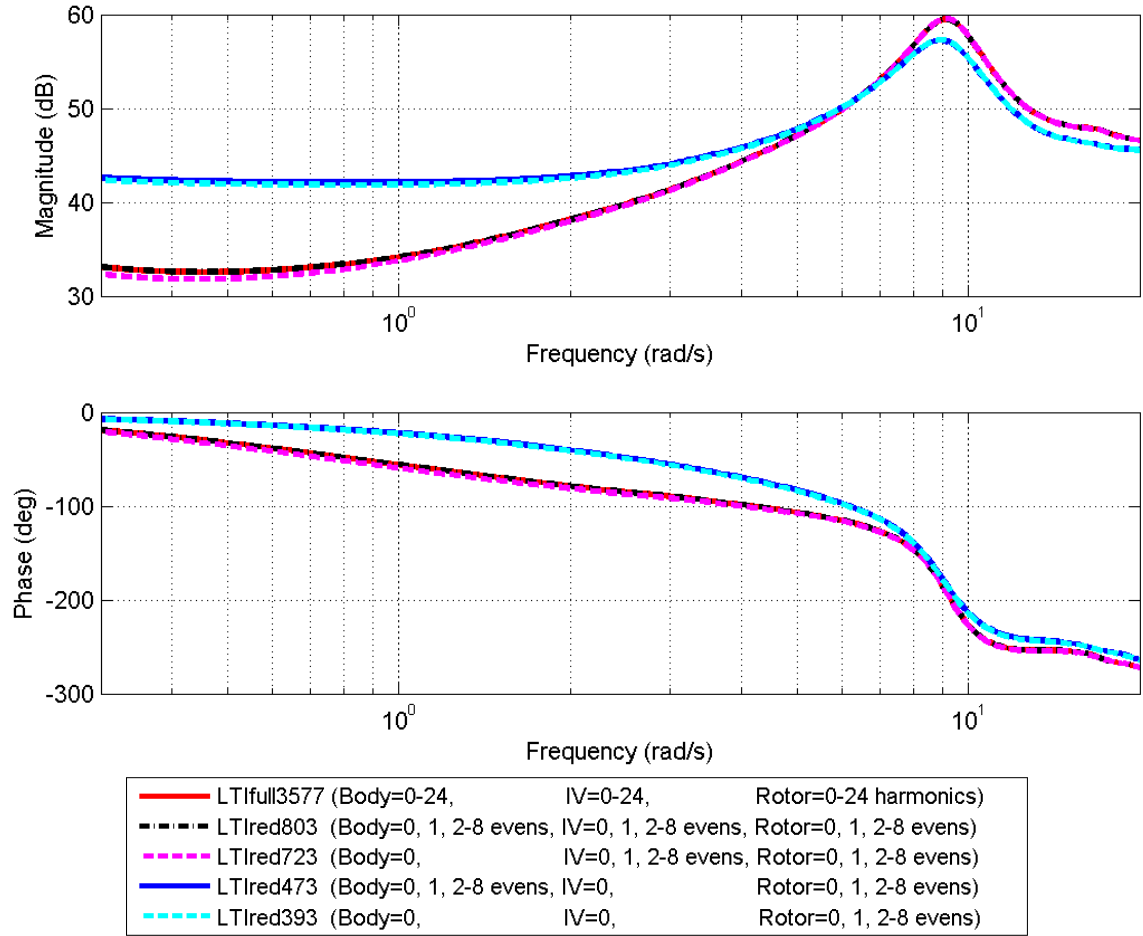
Figure 8. Frequency Response Comparison for IBC4C to F_{y4C}
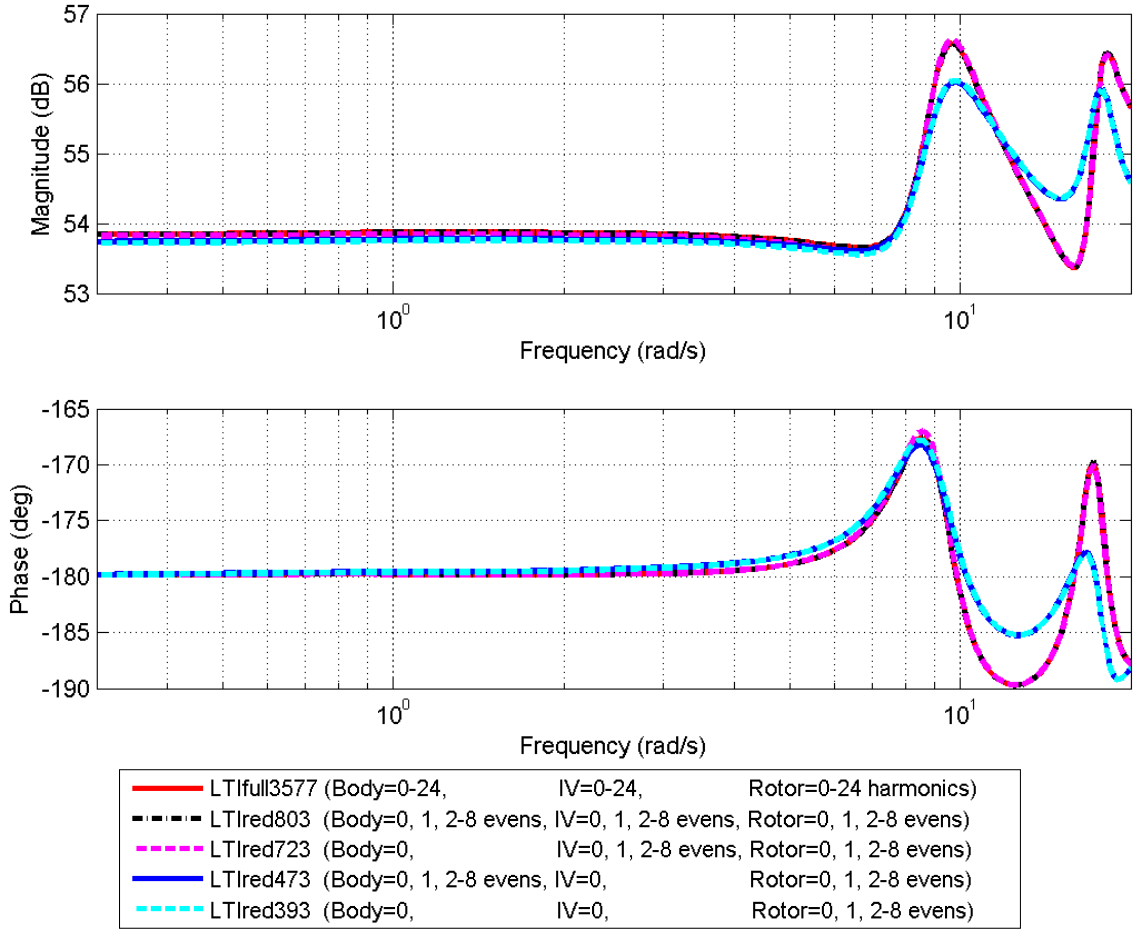
Figure 9. Frequency Response Comparison for IBC4C to F_{z4C}
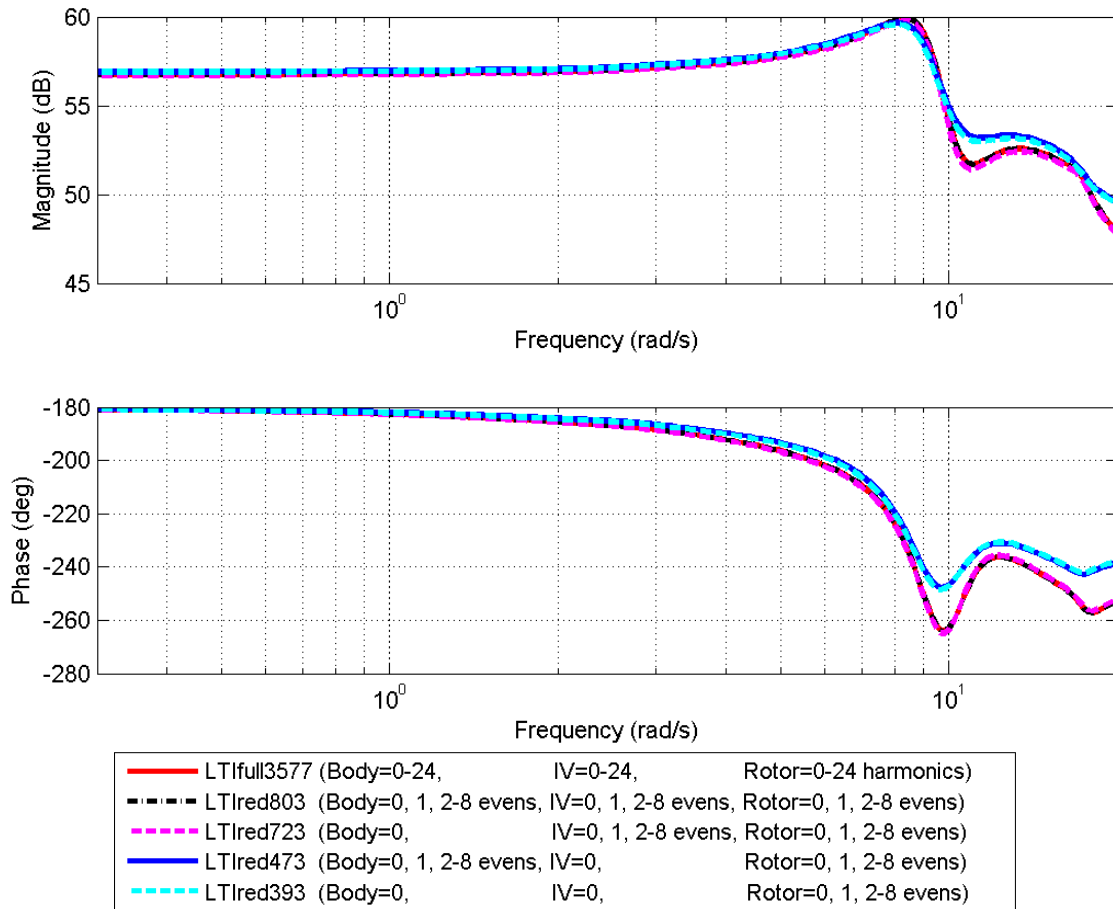
Figure 10. Frequency Response Comparison for IBC4C to M_{x4C}
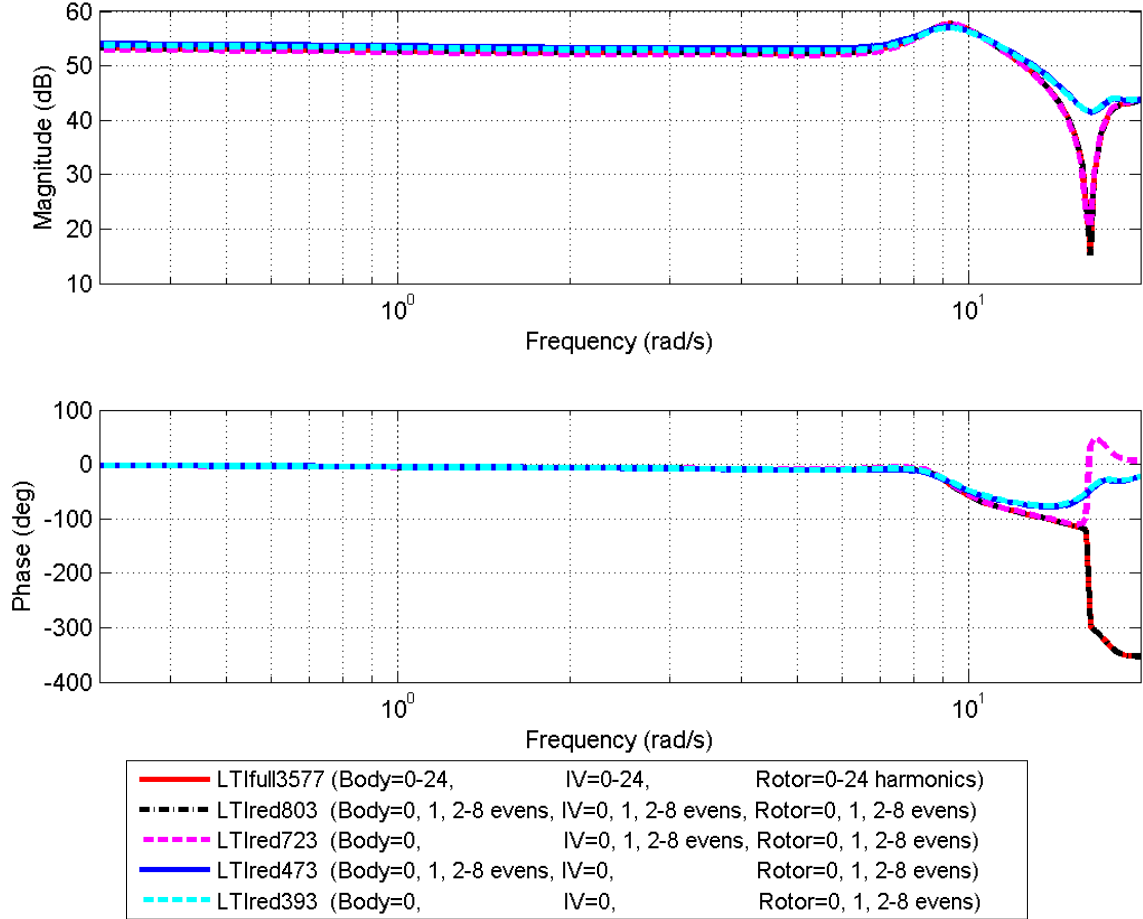
Figure 11. Frequency Response Comparison for IBC4C to M_{y4C}

The normalized additive error (Ref. 29) for IBC4C input for each reduction is shown in Figure 12 for F_{x4C}, F_{y4C}, F_{z4C}, M_{x4C}, and M_{y4C}. Each reduction is compared with LTIfull3577, with LTIfull3577 taken as the truth model. Here it is clear that there is very small normalized additive error for LTIred803, meaning that virtually no additional robustness would be needed for designing a controller based on the LTIred803 model compared to the LTIfull3577 model. Normalized additive error for LTIred723 is on the

order of 0.01~0.05 meaning that some additional robustness would be needed for designing a controller using the LTIred723 model compared to the LTIfull3577 model. Normalized additive error for LTIred473 and LTIred393 are both on the order of 0.2, meaning that additional robustness would be needed for designing a controller using either reduced model compared to the LTIfull3677 model. Thus, it is again clear that retaining harmonic terms for body and inflow states is important for reducing additional robustness needed in controller design.
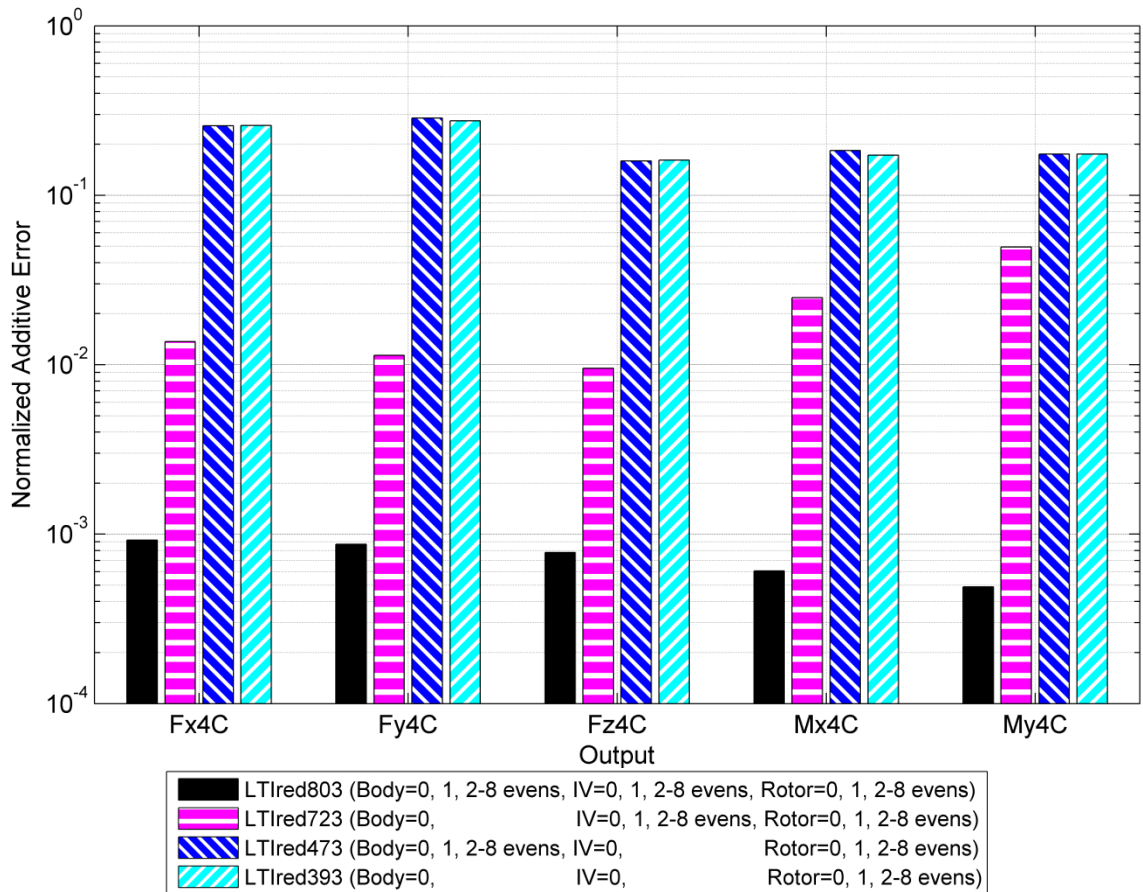
Figure 12. Normalized Additive Error Comparison for IBC4C to 4C Outputs

The nu-gap metric (Ref. 30) for IBC4C input for each reduction is shown in Figure 13 for F_{x4C}, F_{y4C}, F_{z4C}, M_{x4C}, and M_{y4C}. Each reduction is compared with LTIfull3577, with LTIfull3577 taken as the truth model. Here it is clear that there is very small nu-gap metric for LTIred803, meaning that there would be very little losses in stability margin if a controller were designed using the LTIred803 model and applied to the LTIfull3577 model. Nu-gap metric for LTIred723 is at most on the order of 0.1 meaning that there would be very little loss in stability margin if a controller were designed using the LTIred723 model and applied to the LTIfull3577 model. Nu-gap metric for LTIred473 and LTIred393 are both at most on the order of 0.2, meaning that there would be small losses in stability margin if a controller were designed using either model and applied to the LTIfull3577 model (small, but still larger compared to the LTIred723 and LTIred803 cases). Thus, it is again clear that retaining harmonic terms for body and inflow states is important for reducing losses in stability margin when designing controllers based on the reduced models. In the context of vibration reduction considered here, the LTIred803 model is used for further analysis and control design.
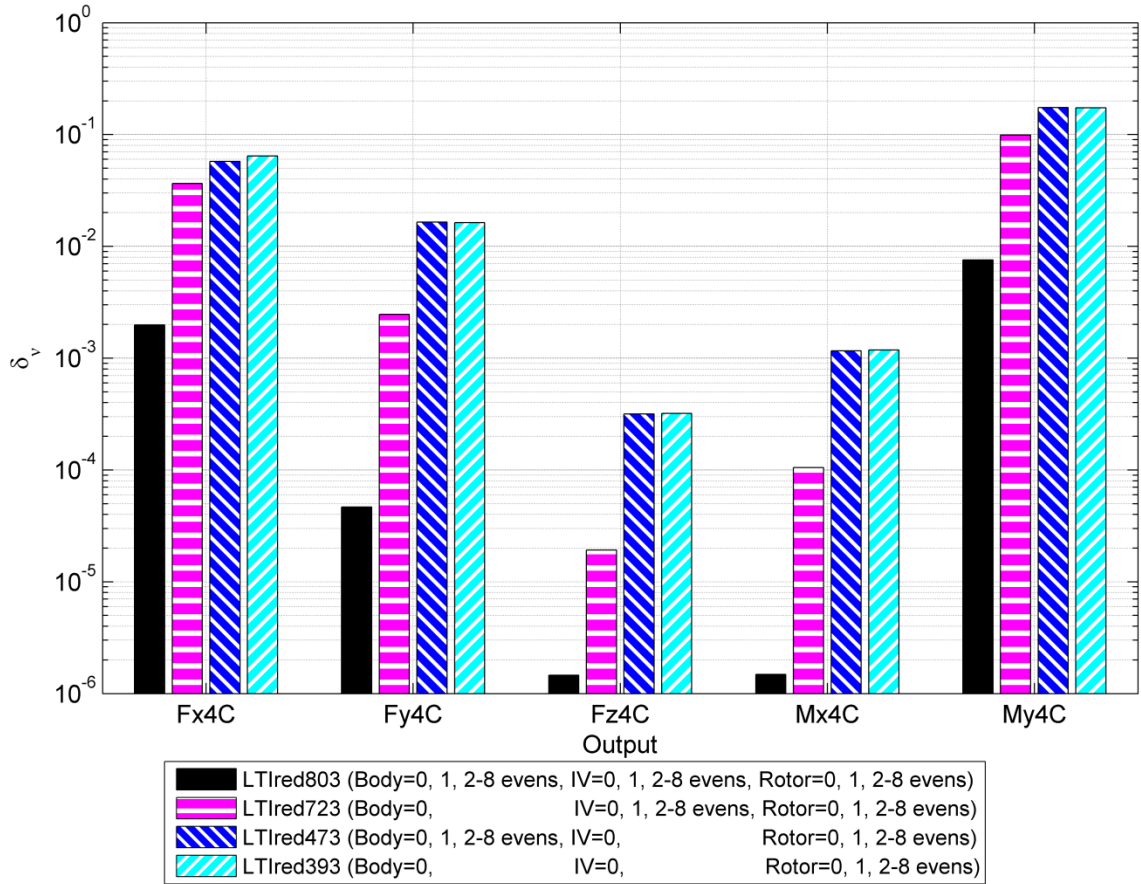
Figure 13. Nu-gap Metric Comparison for IBC4C to 4C Outputs

4.5 Balanced Model Reduction

For the purposes of CONDUIT® optimization (Ref. 31), a model of approximately 100 states or less is desired for computational efficiency. The reduction techniques discussed in Section 4.4 have the benefit of preserving the physical meaning of each state, which is useful when state information is important (e.g. modal analysis or state-feedback control design). For cases where only input-output information is important and state information is not important (e.g vibration reduction), an alternate realization

51

for the LTI model can be used for model reduction. For the example examined here, LTIred803 is reduced by first putting it into a balanced realization form (Ref. 32), which makes the input, output, and state energies all equal. Although it is possible to directly put LTIfull3577 into a balanced realization form, for computational efficiency LTIred803 is used instead. The associated Hankel Singular Values reflect the overall importance of each state for controllability and observability, thus states with low energy can be truncated.

The Hankel Singular Values for each state are shown in Figure 14 on a log scale. The maximum Hankel Singular values are nearly 50,000, while the minimum singular values for the 200 states with the least amount of energy are too small to be computed accurately due to machine precision. It was found that most of the energy is contained in approximately 100 states, corresponding to Hankel Singular Values of 20 or larger. Thus, only these 100 states with the most state energy are kept in the reduction (referred to as LTIred100).
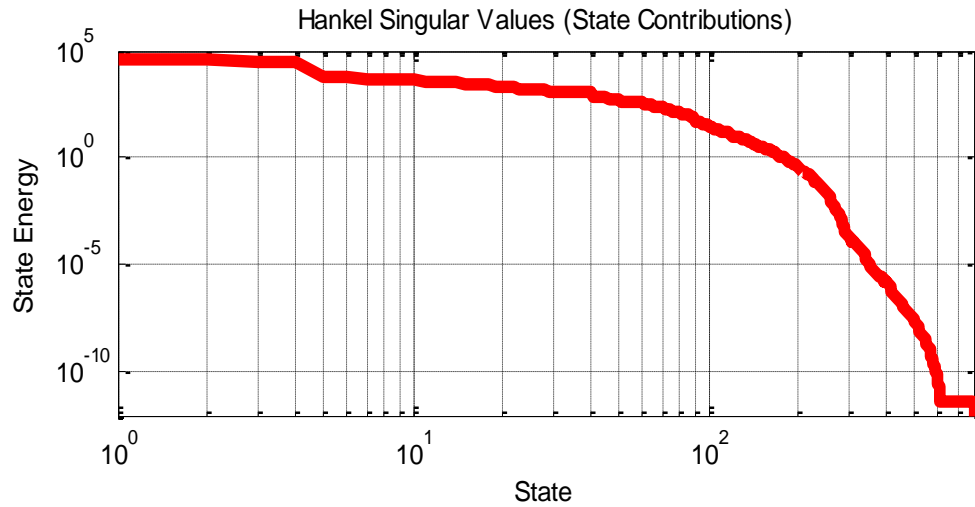
Figure 14. Hankel Singular Values (State Energy)

The bare airframe response for IBC4C to Fz4C is shown in Figure 15 for the LTI models before and after the balanced reduction. The two models are essentially identical in terms of frequency response with any differences being negligible. It is also important to note that there are 2 modes that severely affect HHC performance: a mode at 9 rad/s and another mode at 17 rad/s. Both modes can clearly be seen as very large peaks in the bare airframe response. These modes have been previously identified to be coupling between the dynamic inflow and body response (Ref. 33) and must be taken into account in the HHC and crossfeed design.
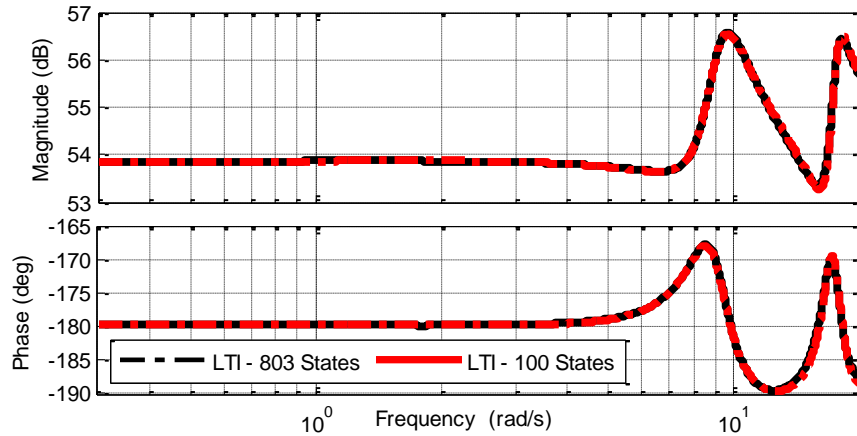
Figure 15. Bare Airframe Response IBC4C to Fz4C for LTIred100

The 100 state reduced order linear model is compared against the nonlinear model using error response plots between linear and nonlinear model bare airframe responses. An example error response plot is given in Figure 16. In Figure 16, the cost functions J are 0.137 and 2.219 for IBC4C to Fz4C and Fz4S respectively. The average cost function over all IBC input and 4/rev output transfer functions is 4.92, meaning that the LTIred100 model time response data is nearly indistinguishable from the nonlinear model time response data in the frequency range of concern to the controller ($\omega_c \approx 3$ rad/s).
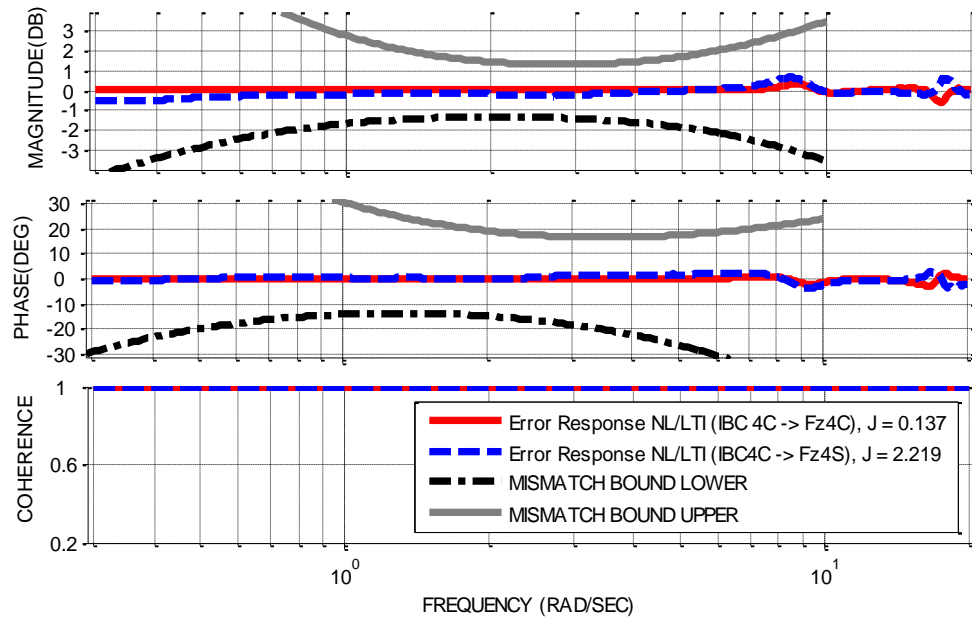
Figure 16. Error Response Plot for Fz4C and Fz4S for LTIred100

CHAPTER 5. INTEGRATED FLIGHT AND VIBRATION CONTROL

Having developed a methodology for extracting and validating reduced order linear time invariant approximation models, the next step is to use these models in the design and validation of an integrated flight and vibration controller.

5.1 Integrated Flight and Vibration Control

Vibration reduction is an important and well understood field of rotor dynamics as demonstrated by the fundamental work of Friedmann and Teves (Refs. 1 and 2). Using the LTI models developed here, a higher harmonic controller (HHC) using a nominal T-Matrix (Ref. 34) architecture can easily be extracted which will reduce steady state vibrations.

The model examined is the UH-60A full vehicle nonlinear model (NL) in FLIGHTLAB® (Ref 25.) The NL model is used in conjunction with a control system in Simulink. The flight control system used is the Advanced Digital Optical Control System (ADOCS) (Ref. 35) shown in the top loop of Figure 17. Additionally, the HHC loop is shown as the bottom loop of Figure 17.

The ADOCS architecture includes feedback for stabilization as well as explicit model following which uses feed forward and inverse plant dynamics. Piloted handling qualities are desirable or adequate for all low, medium, and high gain pilot tasks.

The HHC considered here is implemented for the purpose of vibration reduction. Specifically, the objective of the HHC is to minimize outputs consisting of the 4/rev cosine and sine components of hub forces and moments except rotor torque (Fx4C, Fy4C, Fz4C, Mx4C, My4C, Fx4S, Fy4S, Fz4S, Mx4S, My4S).

Both the AFCS and HHC loops are traditionally designed independently, as shown in Figure 17. Because they are designed independently, there may be one way coupling from the AFCS onto the HHC. This coupling can result in significantly degraded vibration reduction performance during maneuvering flight. This coupling is addressed in this chapter by development of an integrated flight and vibration controller though the use of dynamic crossfeeds.
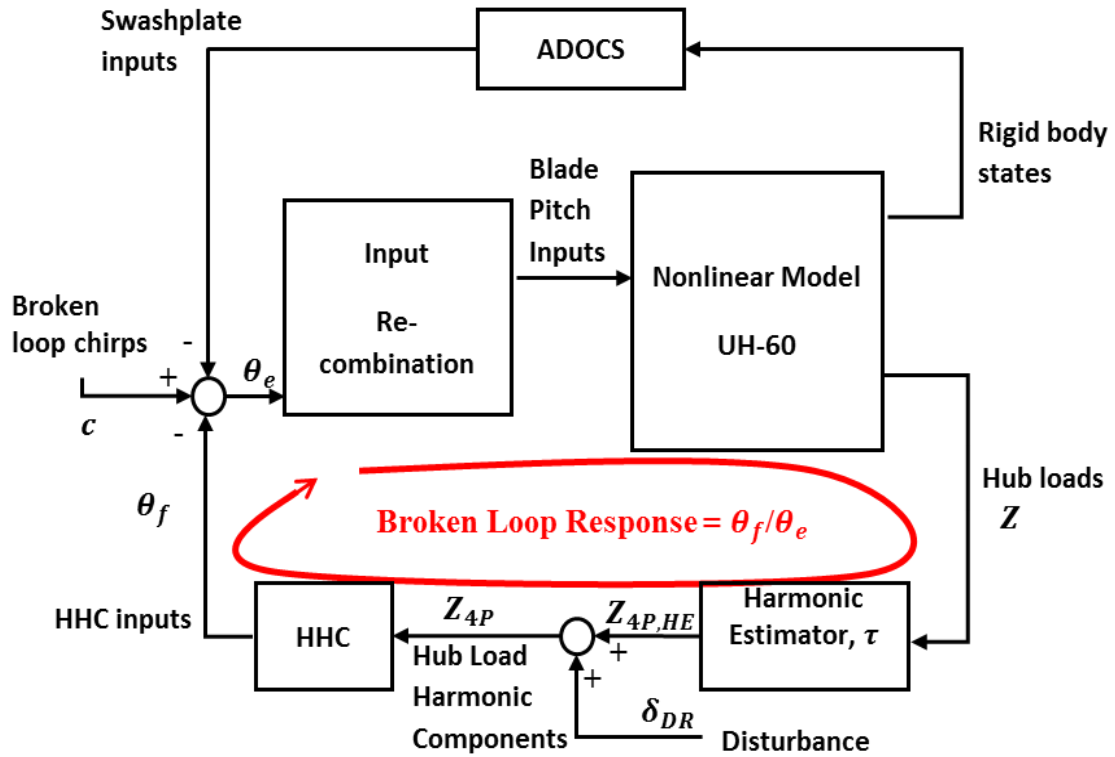
Figure 17. HHC/AFCS Architecture from Ref. 9 showing two independent loops

5.2 Baseline Higher Harmonic Control Laws

The HHC design uses a Transfer matrix (T-Matrix) approach (Ref. 34), which assumes that the 4/rev harmonic load outputs Z_{4P} are a linear static mapping from the higher harmonic control inputs θ

$$Z_{4P} = T\theta \tag{67}$$

where, the T-matrix is extracted directly from the linear model as it is simply the DC gain matrix between IBC inputs and 4/rev outputs. To put the 4/rev moments into comparable units as the 4/rev forces, the 4/rev moments are weighted by $1/\Delta Z$ where ΔZ is the vertical displacement of the rotor hub from the vehicle center of gravity. These weightings are used when computing the pseudo inverse T^{+} (Ref. 8) and for any 4/rev load comparisons. The T-Matrix controller can be implemented using either a proportional or an integral type of controller. Here, an integral controller is preferred as integral controllers can better address steady state errors and thus better reduce steady state vibrations levels. The resulting integral controller in the Laplace domain is then simply defined as

$$\theta = -\frac{1}{s}T^{+}Z_{4P} \tag{68}$$

Substituting Eq. (67) back into the T-matrix controller Eq. (68) results in the broken-loop response θ_{f}/θ_{e} as indicated in Figure 18

$$\frac{\theta_{f}}{\theta_{e}} = \frac{1}{s}T^{+}T \approx \frac{1}{s} = \frac{K}{s} \tag{69}$$

where K/s is the broken-loop response with K set to 1 for the nominal T-matrix case and results in a crossover frequency of $\omega_{c} = 1$ rad/s.

The nominal T-matrix was implemented both in the nonlinear and linear systems to verify the linear analysis is consistent with the nonlinear analysis. Figure 18 shows the weighted nonlinear steady state 4/rev loads for the no T-Matrix case and the nominal T-matrix case (K = 1). All 4/rev loads are decreased in the K = 1 case except Fz4. In the

no T-matrix case Fz4 is much smaller compared to all other 4/rev loads which corroborates comparisons with wind tunnel data (Ref. 9). Therefore, Fz4 is allowed to increase for overall increased benefit of minimizing the average 4/rev loads in the K = 1 case.
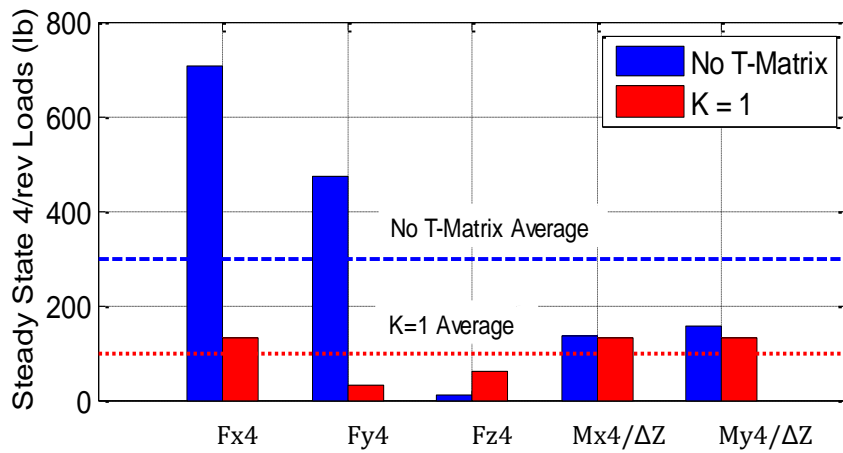
Figure 18. Weighted Steady State 4/rev Loads (Nonlinear Model)

The broken-loop and disturbance rejection responses are now compared for the nonlinear and linear models. For the K = 1 case, both nonlinear and linear models predict similar broken-loop responses (Eq. (69)) as shown in Figure 19. For the IBC4C broken-loop response both linear and nonlinear models have similar crossover frequencies ω_c of about 1 rad/s (as expected for the K = 1 T-matrix controller). The margins using the linear and nonlinear models are in good agreement, where the nonlinear gain margin

(GM) is 10.48 dB and the linear gain margin is 10.42 dB. Likewise, the nonlinear phase margin (PM) is 78 deg and the linear phase margin is 79 deg.
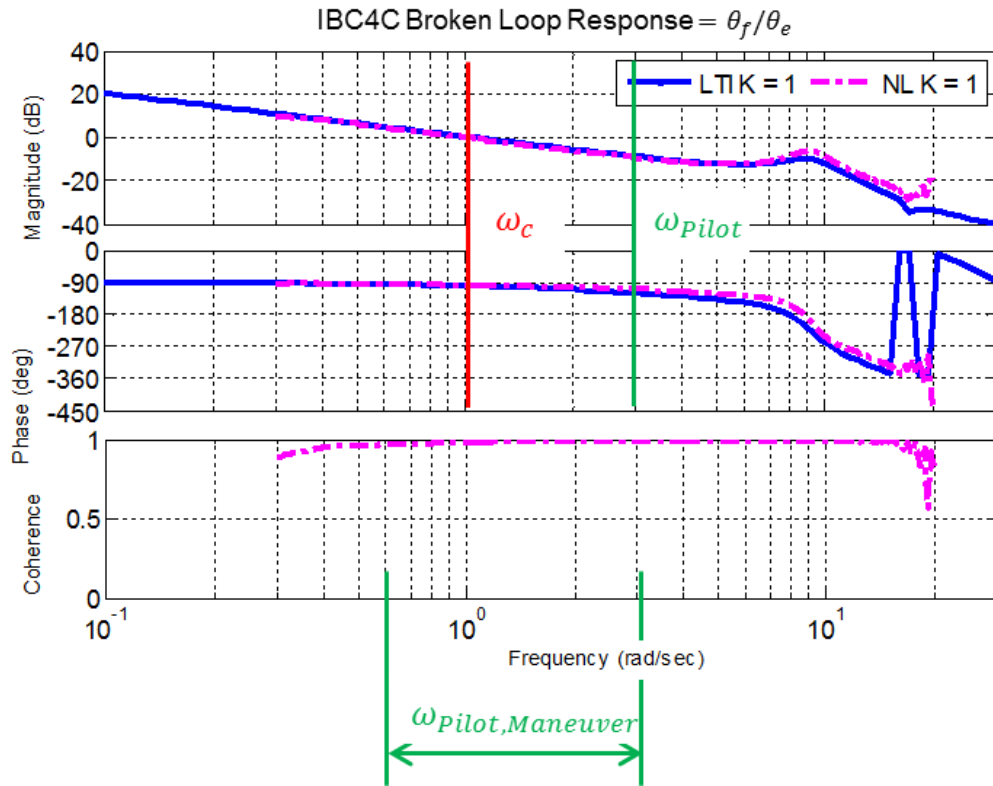
Figure 19. IBC4C Broken-Loop Response for K=1

The disturbance rejection response is the 4/rev load response to a 4/rev load disturbance which is defined in Figure 17 as Z_{4P}/δ_{DR}. The disturbance rejection bandwidth (DRB) is the frequency at which the disturbance rejection response falls below

-3 dB (Ref. 26). The disturbance rejection peak (DRP) is the largest magnitude of the disturbance rejection response.

For the K = 1 case, both nonlinear and linear models also predict similar disturbance rejection responses, as shown in Figure 20 for the Fz4S. For Fz4S the DRB for the nonlinear model is 0.75 rad/s while the DRB for the linear model is 0.79 rad/s, which is as expected near the broken-loop crossover frequency $\omega_c = 1$. Similarly, the DRP for the nonlinear model is 0.81 dB while the DRP for the linear model is 0.76 dB. Having validated the bare airframe, broken-loop, and disturbance rejection responses of the linear model against the nonlinear, the linear model is considered accurate to the nonlinear model. Thus, the linear model can be used to make further HHC performance improvements, such as use in CONDUIT® (Ref. 31) for optimization of the T-matrix controller.
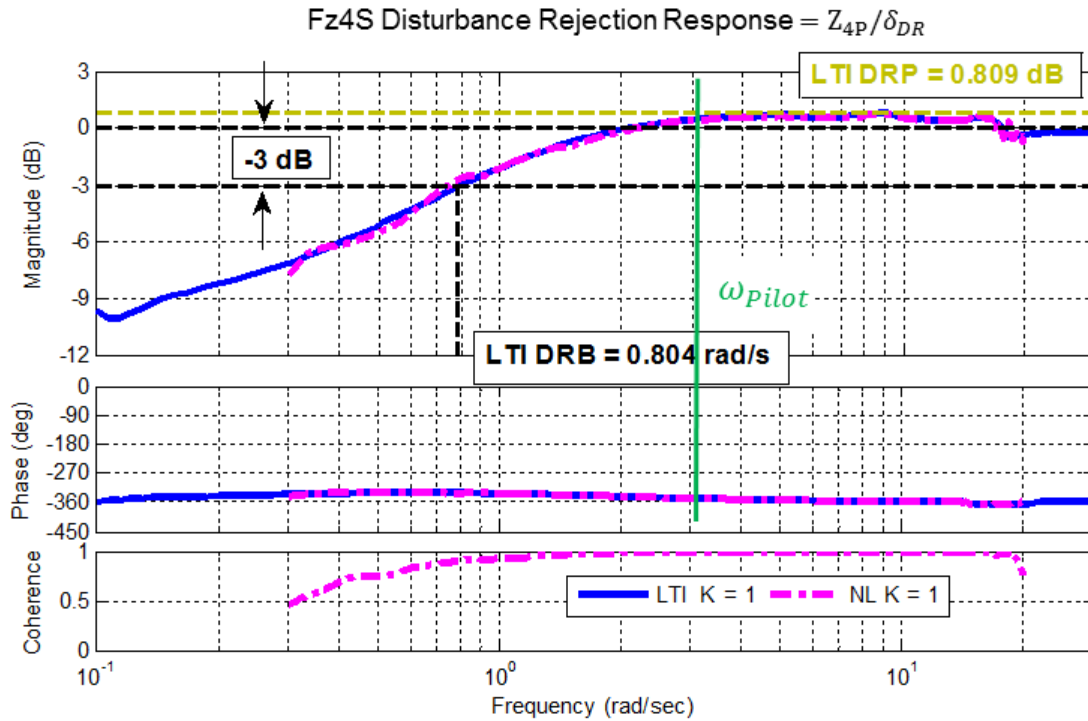
Figure 20. Fz4S Disturbance Rejection Response

5.3 Optimized Higher Harmonic Control Laws

Having developed and verified the baseline K=1 T-Matrix performance, further vibration reduction performance can be achieved through optimization using the LTI model in CONDUIT® (Control Designer's Unified Interface) (Ref. 31). CONDUIT® is a state-of-the-art computational software tool for flight control design and optimization. It is jointly developed by the U.S. Army Aeroflightdynamics Directorate (AFDD) and the University Affiliated Research Center (UARC). CONDUIT® provides a comprehensive

analysis environment which allows for rapid evaluation of control law design against a defined set of handling-qualities and performance specifications. A multi-objective function optimization engine is also integrated into CONDUIT® which provides the capability to automate tuning of user-defined design parameters in order to meet these competing specifications. A collage of the CONDUIT® environment is shown in Figure 21.

CONDUIT® optimization is performed by first determining which handling qualities specifications to use. The stability and performance specifications used here are given in Table 1. Specifications include classic broken-loop gain margin and phase margin for stability; in addition, broken-loop crossover frequency, disturbance rejection peak and disturbance rejection bandwidth specifications are included to improve performance. Furthermore, damping ratio specifications for specific frequency ranges are used to address the coupled inflow/body modes at 9 rad/s and 17 rad/s.

Table 1. Stability and Performance Specifications used in CONDUIT®

Description of Specifications Used	Comments
Broken-Loop Gain and Phase Margins	Ensure adequate stability margins
Broken-Loop Crossover Frequency	Ensure good controller crossover frequencies
Disturbance Rejection Bandwidth	Ensure good disturbance rejection bandwidth
Disturbance Rejection Peak	Ensure satisfactory damping of disturbance response
Damping Ratio	Ensure coupled inflow/body modes well damped
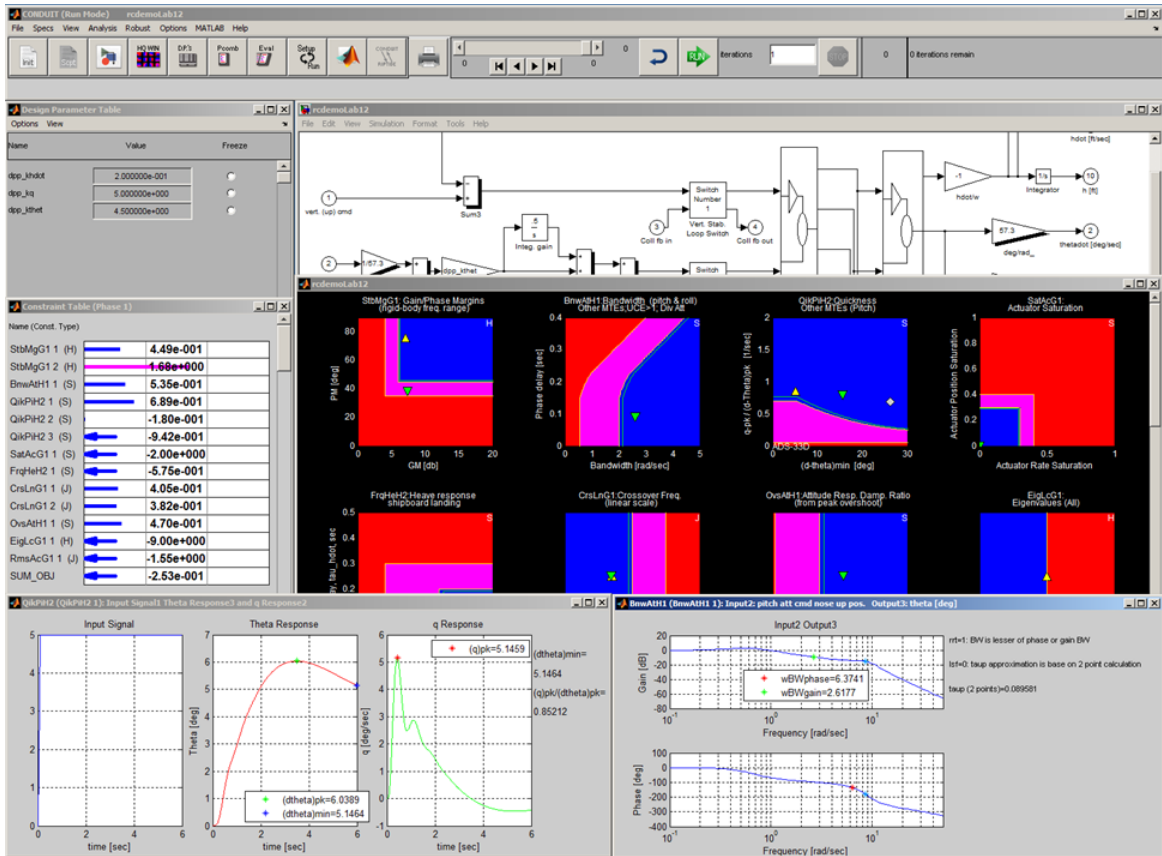
Figure 21. CONDUIT® Environment

Having identified the desired handling qualities specifications, the next step is to define the Level 1 handling qualities specification boundaries. Here, this is defined as having in each broken-loop at least 7.5 dB of gain margin and 55 degrees of phase margin. Also, for each crossover frequency, DRB, and 3 damping ratio specifications (1-8 rad/s, 8-12 rad/s, and 12-20 rad/s), the Level 1 specifications are defined to perform at least as well as the K = 1 case. For each DRP, the Level 1 boundary is defined as 10% higher than the K = 1 case. For illustrative purposes, the handling qualities specifications

for IBC4C and Fz4S are shown in Figure 22 while the entire size of the CONDUIT®

problem is summarized in Table 2 as defined by Mansur et al (Ref. 36).
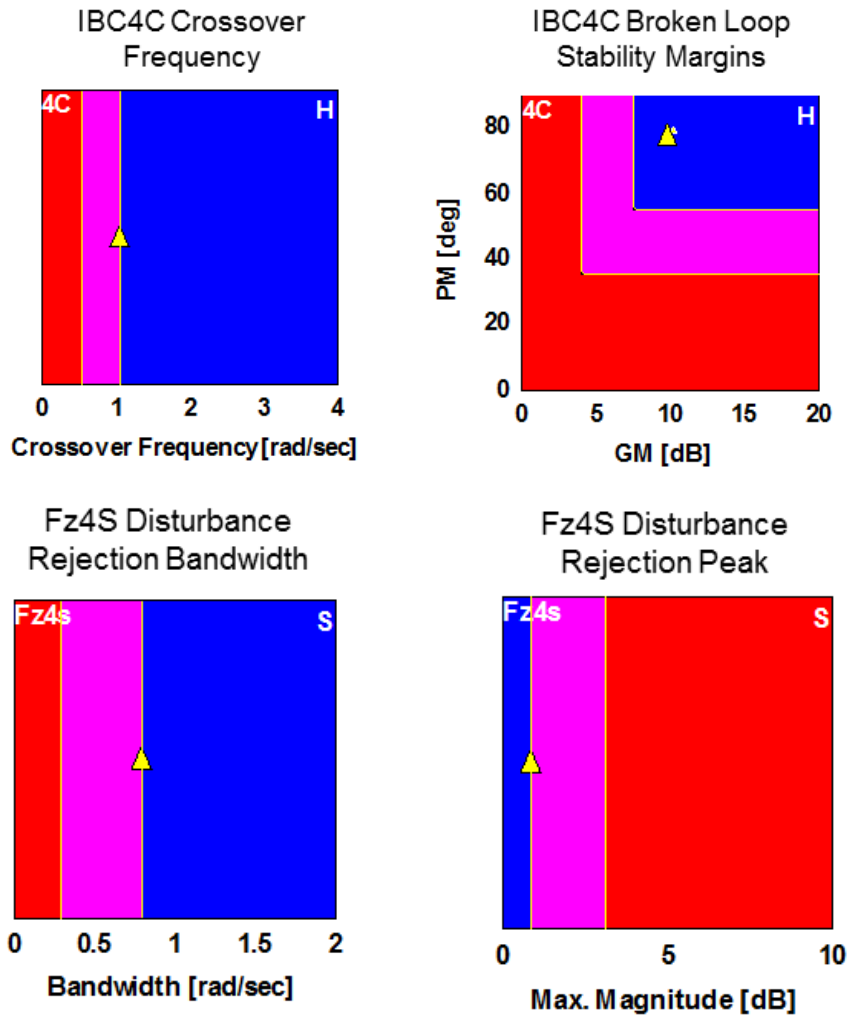
Figure 22. CONDUIT® Specifications for IBC4C and Fz4S

Table 2. CONDUIT® Problem Size

Total Number of States in CONDUIT® System	118
Number of Specifications	$n_{spec} = 41$
Number of Design Parameters	$n_{DP} = 20$
Total Size of CONDUIT® Problem	$n_{spec}n_{DP} = 820$

Optimization was attempted for only the T-matrix gains, but no significant improvement was found. Instead more sophisticated compensation is needed to improve each of the performance specifications while maintaining stability margin; specifically, a first-order dynamic compensator was added to each loop of the form:

$$\frac{\theta}{Z_{4P}} = -\frac{K}{s}\frac{(s+a)}{(s+b)}$$

(70)

The dynamic compensators trade phase margin against gain margin. Also, a second-order Bessel filter is added on Fz4C and Fz4S to prevent the controller from amplifying responses associated with the 9 and 17 rad/s modes. Optimization is then performed to tune each dynamic compensator, forming a lead or lag filter. This design is referred to as the "Opt" design.

The optimized controller design was then implemented in the nonlinear simulation. Figure 23 shows a sample broken-loop response for the K = 1 and the Opt cases for IBC4C. The linear broken-loop responses match well with the nonlinear responses. Also, the Opt case has the same IBC4C crossover frequency as the K=1 case while still maintaining gain and phase margin for IBC4C.
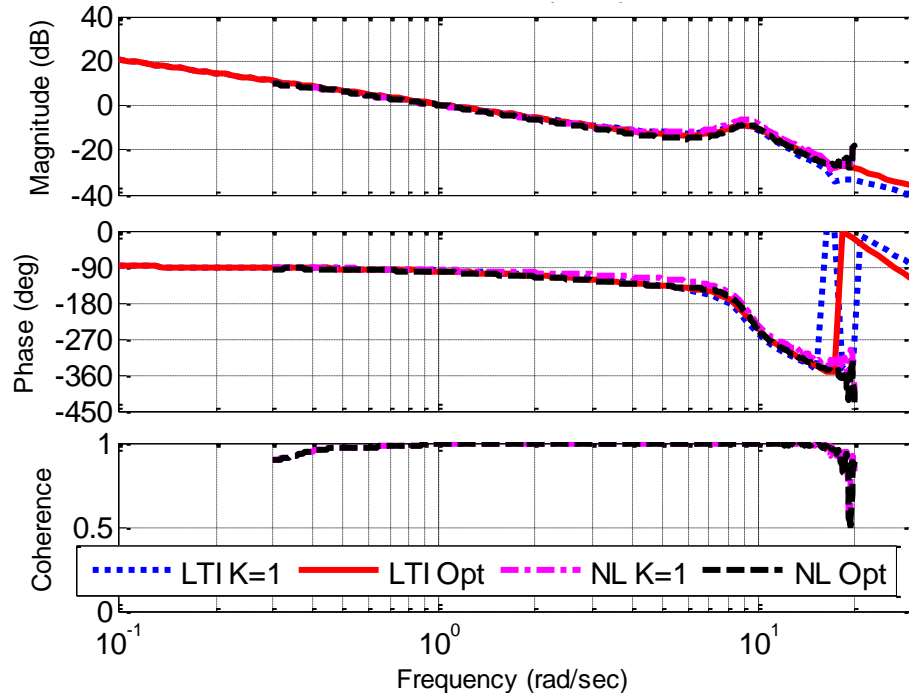
Figure 23. IBC4C Broken-Loop Response

Table 3 compares the specifications between the K = 1 and Opt cases based on the LTI model in CONDUIT®. The Opt case has the improved average crossover frequency by 11% resulting in the average DRB improving by 12%. Similarly, the Opt case has a 17% improvement in the 12-20 rad/s damping ratio.

Table 3. Stability and Performance Specifications from LTI in CONDUIT®

Specs	K = 1	Opt
IBC4C ω_c [rad/s]	1.06	1.07
IBC4S ω_c [rad/s]	0.95	1.00
Average ω_c over all IBC 3,4,5 inputs [rad/s]	0.98	1.09
IBC4C GM [dB]	10.39	9.84
IBC4S GM [dB]	11.55	10.47
Average GM over all IBC 3,4,5 inputs [dB]	16.11	14.98
IBC4C PM [deg]	79.09	77.65
IBC4S PM [deg]	80.17	78.19
Average PM over all IBC 3,4,5 inputs [deg]	76.89	77.67
Damping Ratio [1-8 rad/s]	0.968	0.957
Damping Ratio [8-12 rad/s]	0.120	0.110
Damping Ratio [12-20 rad/s]	0.0596	0.0700
Fz4C DRB [rad/s]	0.832	0.830
Fz4S DRB [rad/s]	0.804	0.800
Average DRB over all 4/rev load components [rad/s]	0.760	0.851

The baseline K = 1 and Opt cases are then compared in the nonlinear simulation using pulse responses. Figure 24 shows the Fz4S response to a 3-inch pitch stick doublet which starts at 35 seconds and has a period of 6 seconds. The Opt case is clearly improved over the baseline K = 1 case, having significantly reduced oscillatory response. Specifically, the Opt case has a 7 percent reduction in peak-to-peak magnitude compared to the K = 1 case, where the peak-to-peak value is considered the largest value throughout the entire response as indicated in Figure 24. It should be noted that the vehicle starts in trim at 35 seconds at 120 knots. Due to the doublet input the vehicle has changed flight condition and finished 20 knots slower resulting in a different steady state condition at the end.
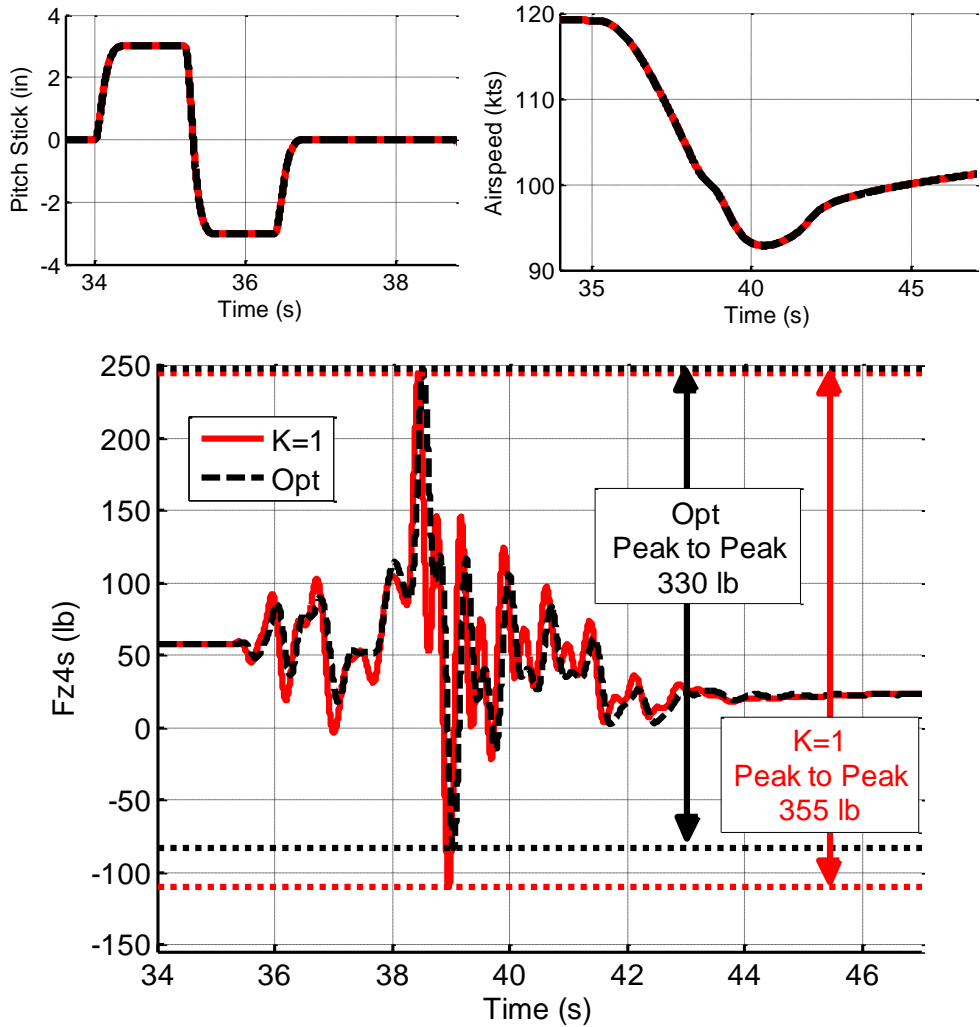
Figure 24. Pitch Stick Doublet Response

5.4 Performance During a Realistic Maneuver

The piloted pullup/pushover maneuver implemented here is based on ADS-33E Mission Task Elements (MTEs) (Ref. 37) which are representative of realistic pilot maneuvers. The maneuver starts at 120kts, followed by a pullup which subjects the vehicle to a high load factor, and then transitions to a pushover and a low load factor. The

ADS-33 pullup/pushover MTE is similar to the Utility Tactical Transport Aircraft System (UTTAS) maneuver (Ref. 38). Both result in the same desired specifications for duration and load factors, except the ADS-33 maneuver has extra specifications on maintaining roll and yaw attitudes.

The maneuver was performed in a real-time piloted simulator; the recorded pilot inputs were then used to reproduce the maneuver in the high-fidelity nonlinear simulation offline. Figure 25 shows the pilot inputs that were recorded and replayed to perform the identical maneuver in the high fidelity simulation case. The HHC is turned on 15 seconds before the maneuver to allow the vehicle to reach a new steady state condition.
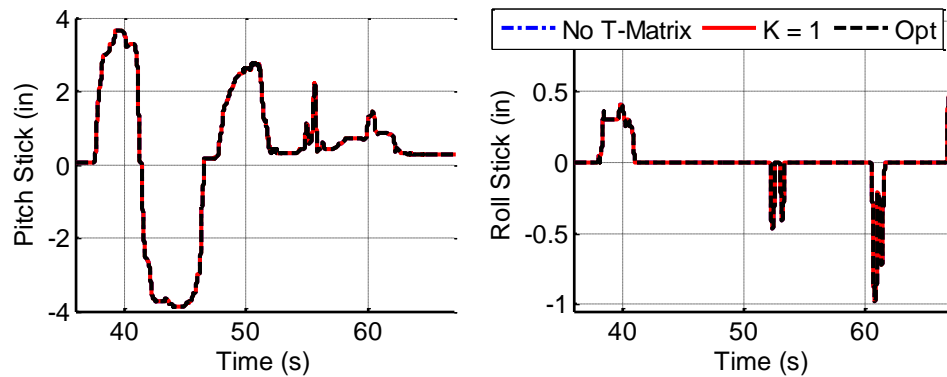
Figure 25. Pullup/Pushover Pilot Inputs

The Fz4S response during the maneuver is shown in Figure 26. The Opt case is improved over the K = 1 case in terms of having reduced oscillatory response. Specifically, the Opt case has a 10 percent reduction in peak-to-peak magnitude compared to the K = 1 case during the pullup/pushover maneuver. This is clearly illustrated in Fz4S power spectral density in Figure 27. After 3 rad/s, the Opt case has consistently the same or less activity than the K = 1 case as shown in the green dotted circle. Therefore, for Fz4S, the Opt case is better than the K = 1 case (being the same at low frequency, but improved at high frequency).
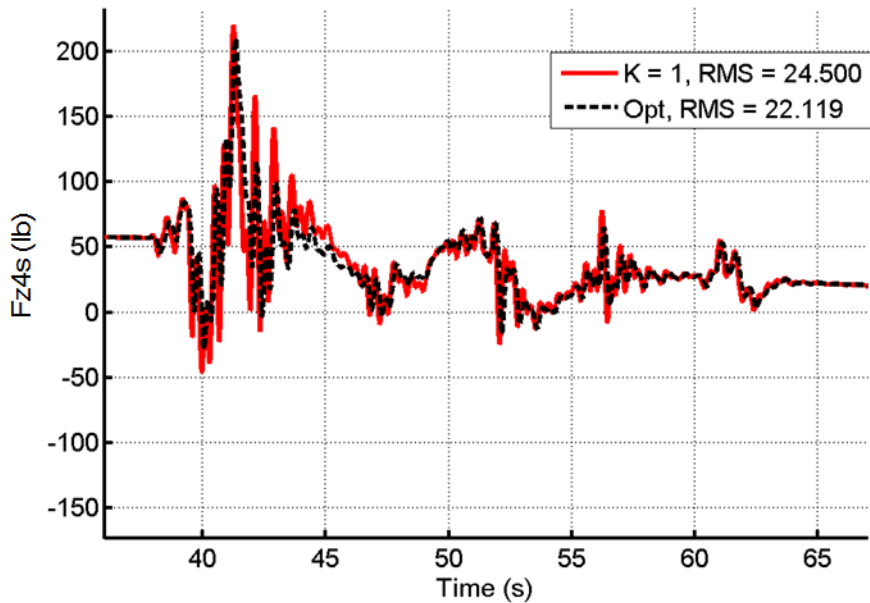
Figure 26. Pullup/Pushover Fz4S Response
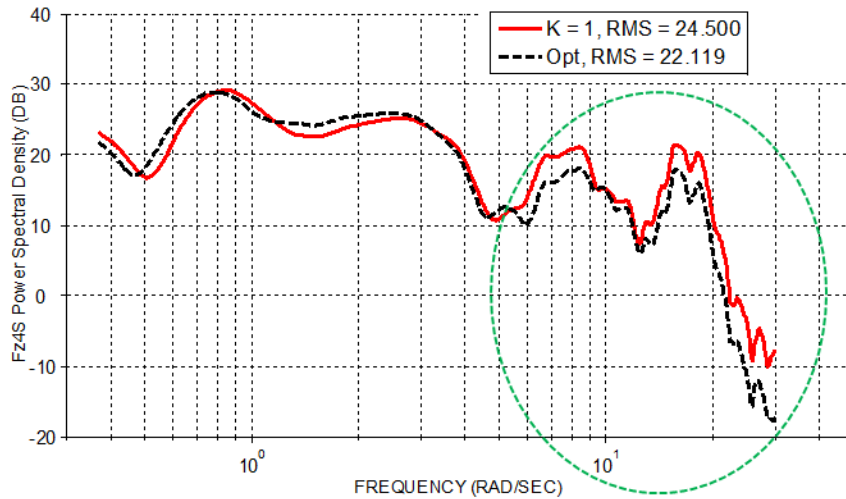
Figure 27. Pullup/Pushover Fz4S Power Spectral Density

5.5 Integrated HHC/AFCS Design

Having improved the T-Matrix controller using optimization techniques, piloted inputs were taken into consideration to further improve performance during maneuvering. Specifically, an integrated controller using dynamic crossfeeds further improved the transient response. Dynamic crossfeeds were developed and shown to be effective on LTI models in Abraham et. al. (Ref. 9). The idea is to feed pilot or swashplate inputs from the AFCS loop into the HHC inputs in the HHC loop. Thus, the 4/rev outputs caused by swashplate inputs can be anticipated and cancelled out via the HHC. Specifically, the crossfeed design considered here is with the AFCS open-loop swashplate inputs crossfed into the HHC closed-loop input as shown in Figure 28, where H is the dynamic crossfeed controller.
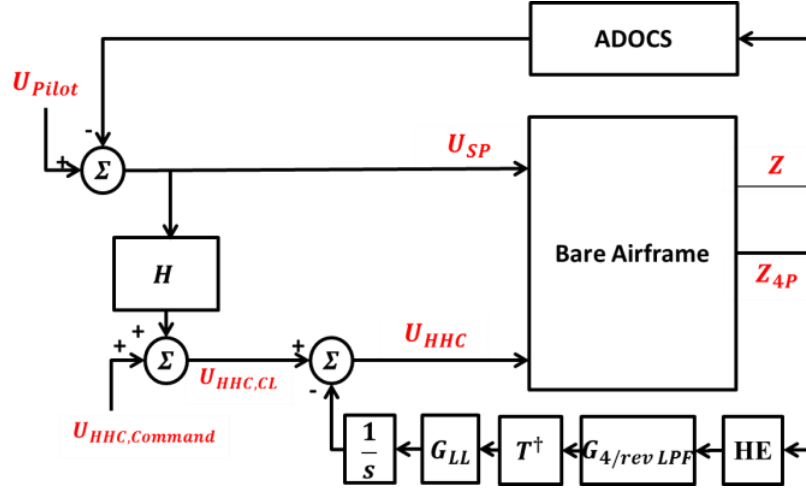
Figure 28. Crossfeed Architecture

From Abraham et. al. (Ref. 9) the ideal crossfeed is given by

$$H_{ideal} = -G^+_{2,CL} G_1 \tag{71}$$

$$G_1 = \frac{U_{SP}}{Z_{4P}} \tag{72}$$

$$G_{2,CL} = \frac{U_{HHC,CL}}{Z_{4P}} \tag{73}$$

$G_{2,CL}$ is the CONDUIT® optimized closed-loop HHC design (Opt). The pseudo inverse $G^+_{2,CL}$ weights are selected to be the same as those used in the T-Matrix controller, minimizing all 4/rev cosine and sine components of hub forces and moments except torque, and weighting moments by $1/\Delta Z$. The ideal crossfeeds H_{ideal} can be

calculated pointwise at every frequency and then fitted using low-order approximations

(Ref. 26). For longitudinal swashplate to IBC3C, the low order approximation is

$$H_{IBC3C,Lon} = \frac{[\zeta = 0.21, \omega_n = 3.2]}{[\zeta = 0.86, \omega_n = 1.8][\zeta = 0.39, \omega_n = 9.4]} \tag{74}$$

where $[\zeta, \omega_n]$ represents a complex pair of poles or zeros with

$$s_{1,2} = -\zeta\omega_n \pm \omega_n\sqrt{\zeta^2 - 1} \tag{75}$$

The ideal crossfeed and low-order approximation for longitudinal cyclic to IBC3C is

shown in Figure 29 and is shown as the red dashed, whereas the ideal crossfeed is the

solid black line. The low order approximation matches very well with the ideal crossfeed

with a cost function J of 9.7 indicating a near exact match.
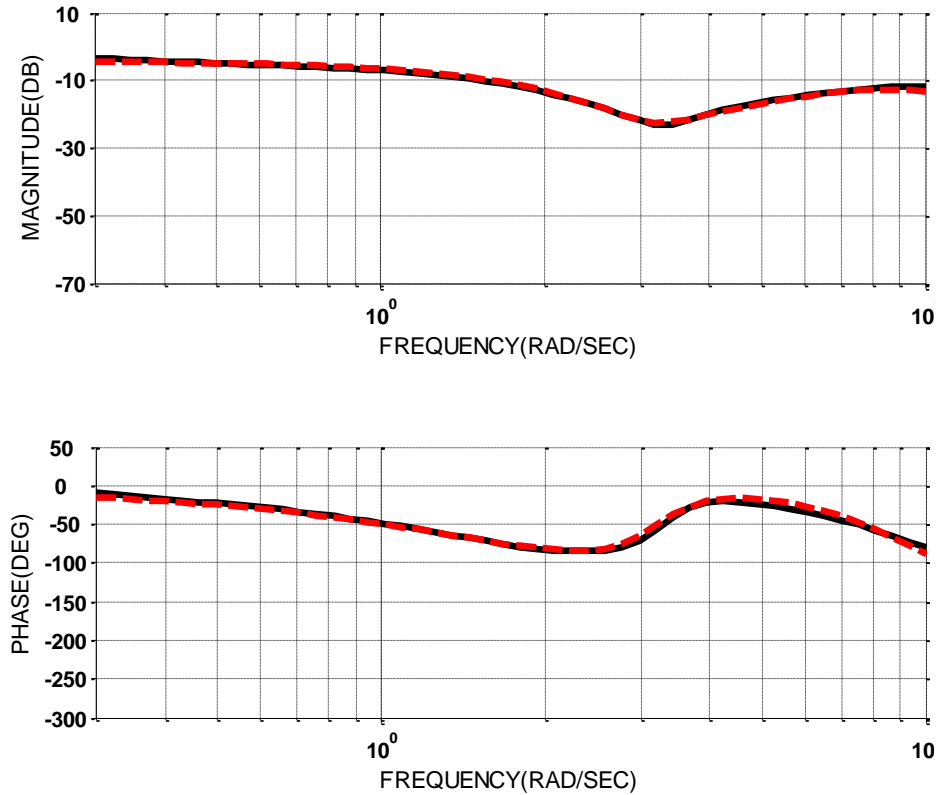
Figure 29. Crossfeed for Longitudinal Cyclic to IBC3C

These ideal crossfeeds are fitted such that the approximations are causal, asymptotically stable, and bounded-input-bounded-output stable. It should be noted that there is no requirement for the low order fits to be minimum phase. The low-order fits are then implemented in the NL model. This case is referred to as the Opt + H case and is used in the pullup/pushover maneuver. The 4/rev loads are the magnitude of the 4/rev cosine and sine components, therefore, for Fx, the 4/rev load can be calculated as:

$$F_{x4} = \sqrt{(F_{x4C})^2 + (F_{x4S})^2} \tag{76}$$

A similar calculation can be performed on the Fy4, Fz4, Mx4, and My4 outputs. The 4/rev load responses of the Opt + H case are shown in Figure 30 for the pullup/pushover maneuver. It is important to note that the body response is unchanged with the inclusion of both the T-Matrix and dynamic crossfeeds, and that there is little influence of the HHC on body response. Specifically, as shown in Figure 30, the primary body response parameters, maneuver airspeed and load factor, remain unchanged when the vibration controller is active. Thus, for the maneuver shown, there is little or no compensation needed by the pilot or in the AFCS design for HHC inputs, thus, there is no effect on handling qualities. This result is in agreement with Cheng et. al. (Ref 8).
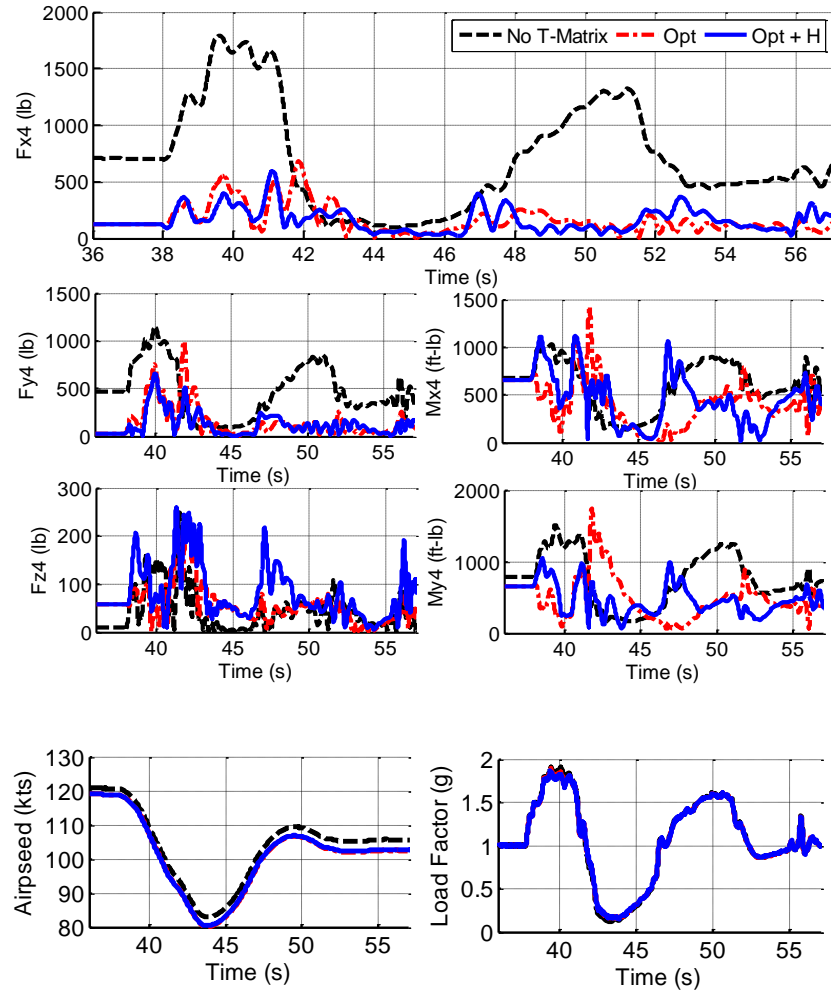
Figure 30. Pullup/Pushover Response

To characterize the vibration reduction performance, each output is examined in terms of root mean square, standard deviation, and the peak-to-peak value previously defined. Here, root mean square (RMS) is defined as:

$$RMS = \sqrt{\frac{1}{N} \sum_{i=1}^{N} x_i^2} \tag{77}$$

where x_i is the ith value of the sequence of values $(x_1, x_2,...,x_i,....,x_N)$ and N is the number of values considered. Furthermore, standard deviation (STD) is defined as:

$$STD = \sqrt{\frac{1}{N}\sum_{i=1}^{N}(x_i - \bar{x})^2}$$ (78)

where $\bar{x}$ is the arithmetic mean of the sequence $(x_1, x_2,...,x_N)$ defined as:

$$\bar{x} = \frac{1}{N}\sum_{i=1}^{N}x_i$$ (79)

The STD is a good measure of how much transient and oscillatory response exists, while RMS is a good measure of how much total response exists.

Fx4 has the largest response for the No T-Matrix case, and the HHC performance is examined with the RMS, STD, and peak-to-peak values given in Table 4. It is clear from the table that, the Opt case has improved RMS, STD, and peak-to-peak values over the No T-Matrix case for Fx4. Furthermore, despite large variations in flight condition, the crossfeeds in Opt + H have further improved RMS, STD, and peak-to-peak values compared to the no crossfeeds Opt case.

Table 4. Pullup/Pushover Performance for Fx4

Specs	No T-Matrix	Opt	Opt+H
Fx4 RMS [lb]	844.3	206.2	191.0
Fx4 STD [lb]	460.7	124.5	102.3
Fx4 Peak-to-Peak [lb]	1696.9	680.0	572.0

It was determined that Fx4S has the largest maximum PSD value among all 4/rev hub load components for the Opt case. The Fx4S PSD for both the Opt case and the Opt + H case is shown in Figure 31. Here it is clear that the Opt + H case has improved the PSD up until the crossover frequency (ω_c =1 rad/s). The difference is as large as 8 dB at 0.7 rad/s. Past the crossover frequency, the HHC has little effect.
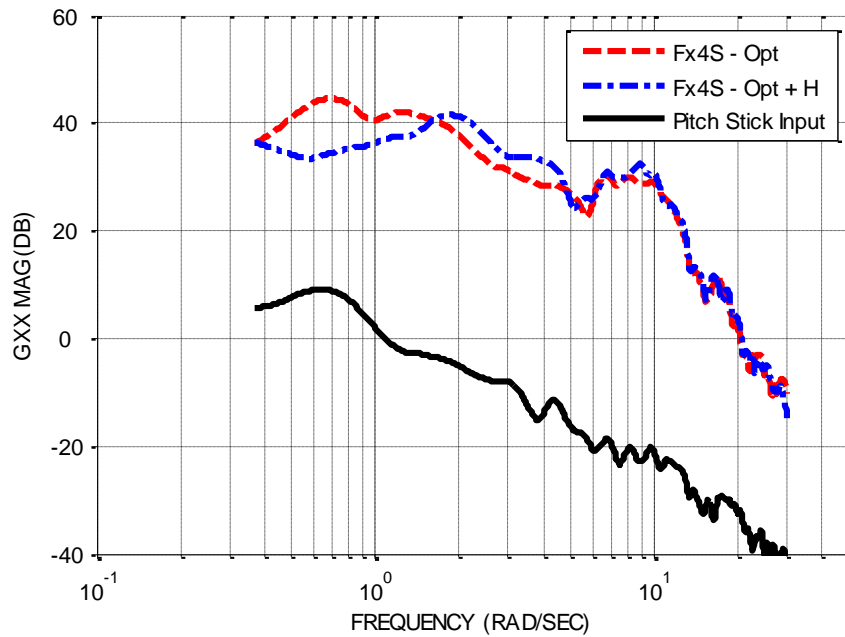
Figure 31. Power Spectral Density for Fx4S

An overall performance improvement can be seen by examining the average RMS. The RMS is calculated for each 4/rev load (Fx4, Fy4, Fz4, Mx4, and My4). The

RMS for Mx4 and My4 are then weighted by $1/\Delta Z$, the same weights chosen for both pseudo inverse calculations. The weighted values are then averaged over Fx4, Fy4, Fz4, Mx4, and My4 to give a single weighted average value for RMS. Specifically, the weighted average for RMS is calculated as follows:

$$RMS_{avg} = \frac{RMS_{Fx4} + RMS_{Fy4} + RMS_{Fz4} + \dfrac{RMS_{Mx4}}{\Delta Z} + \dfrac{RMS_{My4}}{\Delta Z}}{5} \tag{80}$$

A similar process can be done to calculate the averages for STD and peak-to-peak.

The average RMS, STD, and peak-to-peak 4/rev load values are given in Table 5 along with the percent improvement of the HHC cases over the No T-Matrix case shown in parenthesis. It is clear that in terms of average RMS, STD, and peak-to-peak, the Opt case is improved over the No T-matrix case and the Opt + H case is further improved over both cases. Specifically, the Opt + H case has the following improvements over the Opt case: 5% improvement in average RMS, 15% improvement in average STD, and 24% improvement in average peak-to-peak. Overall, the Opt + H case has the following improvements over the No T-Matrix case: 61% improvement in average RMS, 58% improvement in average STD, and 44% improvement in average peak-to-peak.

Table 5. Pullup/Pushover Performance Averages

Specs	No T-Matrix	Opt	Opt + H
Average RMS [lb] (%)	349.8	143.4 (5%)	135.7 (61%)
Average STD [lb] (%)	180.4	89.3 (15%)	75.5 (58%)
AveragePeak-to-Peak [lb] (%)	692.3	507.4 (24%)	384.4 (44%)

CHAPTER 6. ROBUSTNESS EVALUATIONS

Having developed an integrated flight and vibration controller to improve vibration reduction performance during maneuvering flight, the next step will be to evaluate the robustness of the vibration controller. Previous studies examined the sensitivity of vibration levels to flight conditions as well as robustness of traditional HHC designs. Studebaker used flight test data of a UH-60A and found that advance ratio had a significant impact on steady state vibration levels (Ref. 39). Patt et. al. studied the traditional HHC algorithm and found that the fixed-gain HHC performed satisfactorily within 20 kts of design speed (Ref. 40). Fan and Hall recently examined the use of gain-scheduling techniques to develop a full flight envelope vibration controller (Ref. 41). They found that HHC performance is strongly dependent on advance ratio, and weakly dependent on shaft angle and blade loading. They developed a full flight envelope controller using a gain-scheduling techniques. The controller was scheduled at 4 advance ratios (0.15, 0.2, 0.3, and 0.375). An H-infinity controller at each scheduled anchor point was continuously run, and their outputs were blended together using linear interpolation.

Robustness of the integrated flight and vibration controller will be examined in off-design conditions selected based on the previous studies of Studebaker, Patt, and Fan et al. The robustness results will then be used to develop a full flight envelope controller.

The nominal design conditions for the integrated flight and vibration controller developed here are at a true air speed of 120 kts, steady level flight, sea level, standard

day, with gross vehicle weight of 16,300 lb, and a 360 inch moment arm from the nose to the C.G. From previous literature, it is expected that there will be gradual changes of HHC performance as flight speed deviates away from the design speed. From Patt et. al. (Ref. 40), the fixed-gain HHC is expected to perform well within approximately 20 kts of the design speed, thus, deviations of 20 and 30 kts will be examined.

To explore other flight conditions, descending flight, turning flight, variations in altitude and an alternate weight and C.G. configuration will also be examined. From the UH-60 service manual, the UH-60A operating limits define a maximum descent rate of 1,000 feet per minute. Descent rates of 425 and 850 feet per minute, corresponding to flight path angles of 2 and 4 degrees respectively at 120 kts, are chosen to fall safely within the operating limits. The UH-60 service manual also defines a max bank angle of 30 degrees, thus 2 different turning conditions are examined: 4 and 27 degree bank angles at 120 kts. From Tobias and Tischler, gradual variations in flight dynamics due to altitude changes were observed (Ref. 42). This will also be explored for the HHC by considering alternative altitudes of 3,000 and 6,000 feet. Finally, to explore alternate vehicle inertial configurations a gross vehicle weight of 20,000 lb with a 350 inch C.G. moment arm is examined, which falls within the acceptable operating C.G. limits defined by the UH-60 service manual. The full off-design conditions for robustness evaluation are given in Table 6, known as the robustness test matrix.

Table 6. Robustness Test Matrix: Off-Design Conditions for Robustness Evaluation

Case Number	Off-Design Type	Deviation From Nominal Conditions
1	Speed	140 kts (20 kts increase)
2	Speed	150 kts (30 kts increase)
3	Descent	2 deg flight path angle (425 fpm)
4	Descent	4 deg flight path angle (850 fpm)
5	Turning	4 deg bank angle
6	Turning	27 deg bank angle
7	Altitude	3,000 ft
8	Altitude	6,000 ft
9	Inertia	20,000 lb, 350 inch moment arm

6.1 LTI Robustness Evaluations of Fixed Point Controller

With the 9 off-design cases defined in the robustness test matrix, the robustness of the optimized HHC is evaluated first using LTI evaluations. For each off-design condition, an LTI model is extracted at those conditions, and this model is then used as the plant in CONDUIT® while keeping the controller fixed at the design based on nominal conditions. This is similar to how a fixed-gain HHC would operate under different operating conditions (the HHC is fixed, but the plant varies due to changes in operating conditions). For every off design case, each CONDUIT® design specification was examined in terms of crossover frequency, gain margin, phase margin, disturbance rejection bandwidth, disturbance rejection peak, and eigendamping specifications. The average crossover, GM, PM, DRP, and DRP are listed for each case in Table 7.

Table 7. Off-Design LTI Robustness Evaluations

Case	Conditions	Average Crossover (rad/s)	Average GM (dB)	Average PM (deg)	Average DRB (rad/s)	Average DRP (dB)
-	Nominal	1.085	14.98	77.67	0.851	0.991
1	140 kts	1.109	14.53	78.47	0.875	0.993
2	150 kts	1.120	14.49	78.68	0.890	1.018
3	2 deg descent	1.092	14.72	77.97	0.856	0.979
4	4 deg descent	1.099	14.25	78.63	0.864	0.991
5	4 deg bank	1.084	14.98	77.77	0.850	0.990
6	27 deg bank	1.065	14.74	76.77	0.844	1.058
7	3,000 ft altitude	0.968	15.41	78.61	0.764	0.909
8	6,000 ft altitude	0.856	15.88	79.37	0.680	0.858
9	Weight and C.G.	1.084	14.98	77.74	0.850	0.991

Compared to the nominal conditions case, all CONDUIT® specifications examined showed minor changes in stability and performance specifications for descending flight, turning flight, and the alternate weight and C.G. configuration. It is very clear, however, that there are gradual changes in stability and performance when there are changes in flight speed and altitude as indicated by the small changes seen in cases 1 and 2. For example, the average crossover frequency for the nominal conditions (120 kts) is 1.085 rad/s, but this increases to 1.109 rad/s at 140 kts (case 1), and further to 1.120 rad/s for 150 kts (case 2). Similarly, there are gradual changes with average crossover as altitude changes: at sea level (nominal conditions) the average crossover is 1.085 rad/s, but at 3,000 ft the average crossover drops to 0.968 rad/s, and further drops to 0.856 rad/s at 6,000 ft.

6.2 NL Robustness Evaluations of Fixed Point Controller

At this point, the LTI results showed that very little impact on stability and performance of the HHC for descending flight, turning flight, alternate weight and C.G. configuration. However; the LTI results do show gradual changes in stability and performance of the HHC with respect to changes in speed and altitude. The robustness of the HHC has been examined with respect to stability and performance using CONDUIT®; however, this CONDUIT® evaluation has not included dynamic crossfeeds. To evaluate the full integrated controller, performance evaluations using the nonlinear model during maneuvering flight will be used here.

For simplicity, the integrated flight and vibration controller is evaluated using generic pilot doublets. The generic maneuvers will be performed at each off-design test condition both with and without the fixed-gain vibration controller active. Figure 32 shows the pilot stick inputs, with the pitch stick doublet starting at 35 seconds and ending at 41 seconds. Figure 33 shows the response to the pitch stick doublet at the nominal design conditions (120 kts). The response with the HHC off is shown by the red solid line, while the response with the fixed-gain integrated flight and vibration controller (optimized with dynamic crossfeeds) is shown in dashed black. Figure 34 shows the pitch stick doublet 4/rev magnitude response at 140 kts (test case 1). In off design cases, the vibration controller is the same fixed-gain integrated design (designed at the 120 kts, nominal conditions), but the controller is used at off-design conditions – in the case Figure 34, 140 kts.

The steady state vibration levels are different between the 120 kts (Figure 33) and 140 kts responses (Figure 34) making direct comparison of responses difficult. Instead,

the performance is evaluated using a percent improvement compared to the HHC off cases. Table 8 shows the average 4/rev magnitude RMS, STD, and peak-to-peak (P2P) values for each off design case. The values are listed for HHC and no HHC, and also the HHC percent improvement is shown, which allows off-design cases to be compared with the nominal design HHC percent improvement. For example, for the nominal conditions, the fixed-gain HHC improves average RMS by 61%, STD by 42%, and peak-to-peak by 30%. At 140 kts flight conditions, the fixed gain HHC (designed at 120 kts) improves average RMS by 59%, STD by 41%, and peak-to-peak by 32%. At 150 kts flight conditions, the fixed gain HHC (designed at 120 kts) improves average RMS by 50%, STD by 21%, and peak-to-peak by 17%.

From Table 8 it is clear that for a pitch stick maneuver, there are gradual changes in HHC performance as flight speed and altitude deviate from the design conditions. Also, descending flight, turning flight, and alternate weight and C.G. location has very little impact on HHC performance.
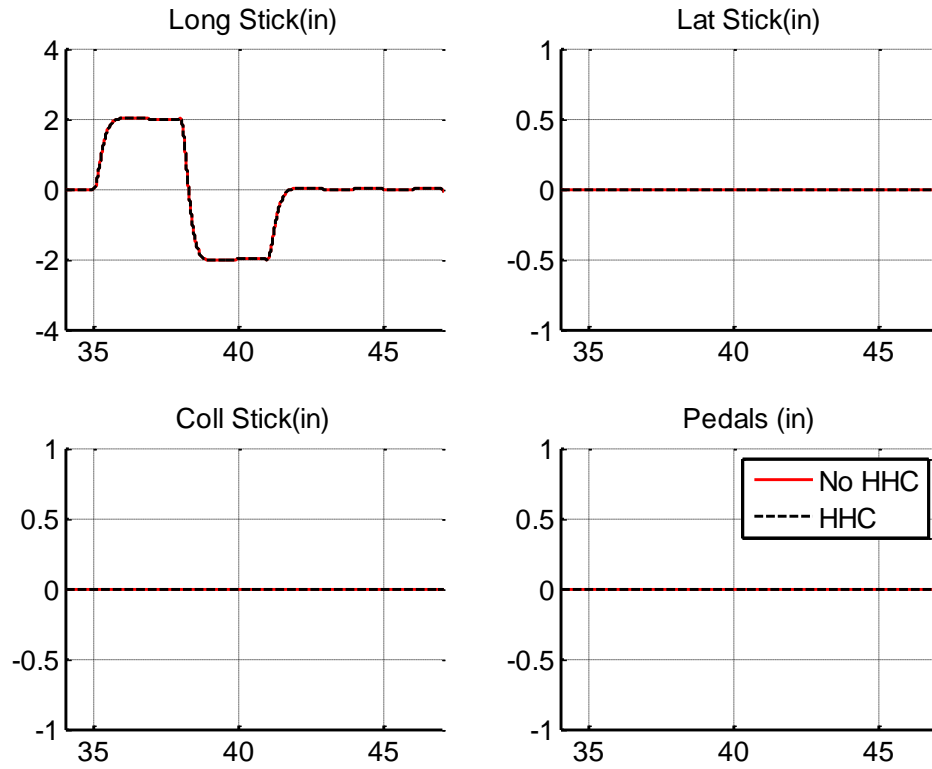
Figure 32. Pitch Stick Doublet for Robustness Evaluations
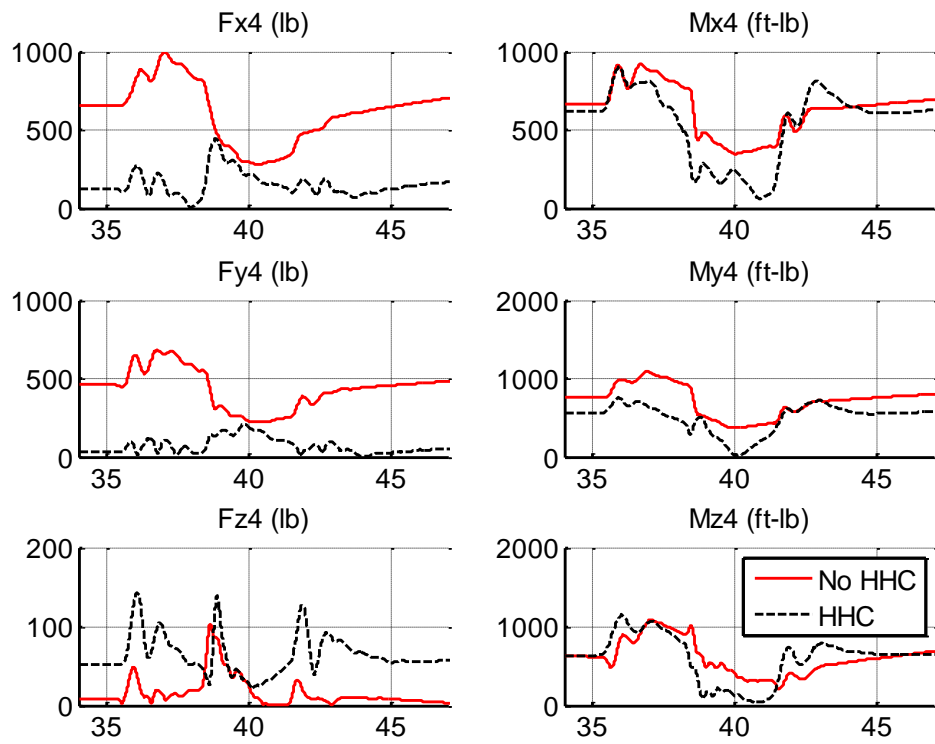
Figure 33. Doublet Response for 120 kts Nominal Conditions
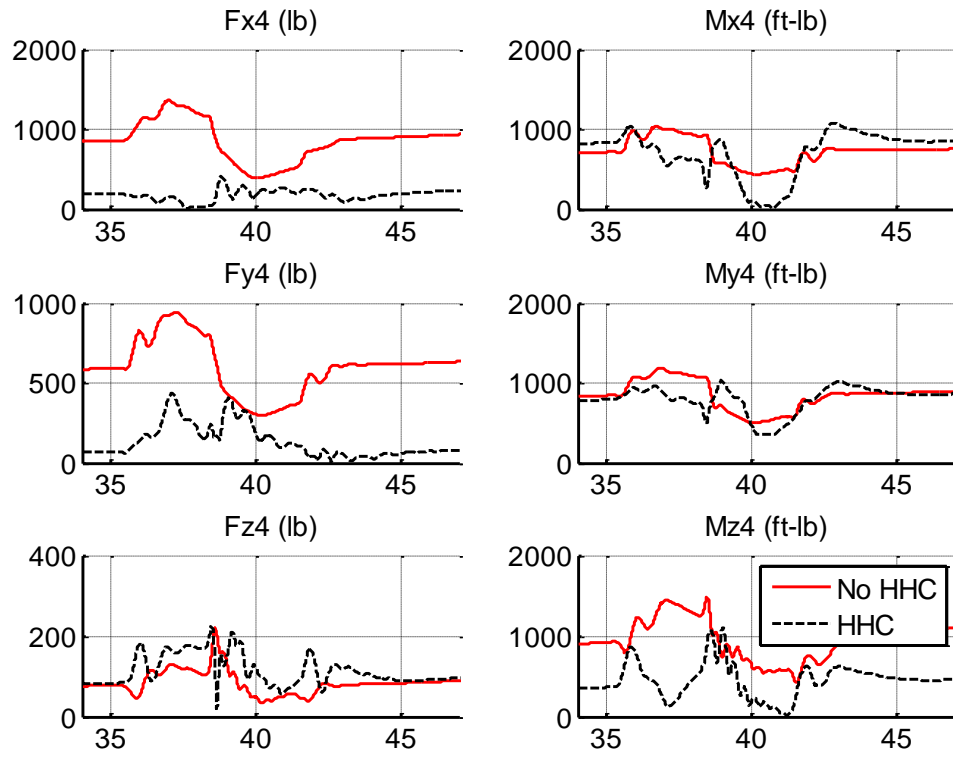
Figure 34. Doublet Response for 140 kts Flight Condition

Table 8. Off Design Pitch Doublet Performance

Case	Conditions	No HHC			HHC			HHC % Improvement		
		RMS	STD	P2P	RMS	STD	P2P	RMS	STD	P2P
-	Nominal	279.4	79.99	307.7	109.7	46.69	216.9	61%	42%	30%
1	140 kts	385	102.1	411.2	158.7	60.22	280.1	59%	41%	32%
2	150 kts	448.6	129	516.6	225.7	101.6	426.2	50%	21%	17%
3	2 deg descent	281.7	78.66	292.1	112	45.75	211	60%	42%	28%
4	4 deg descent	297.8	83.49	302.2	115.3	46.31	218.2	61%	45%	28%
5	4 deg bank	286.7	75.65	287.4	114.6	41.16	193.8	60%	46%	33%
6	27 deg bank	345.7	102.1	403.5	163.3	71.1	323.7	53%	30%	20%
7	3,000 ft altitude	266	72.71	271.3	104.4	41.97	193.8	61%	42%	29%
8	6,000 ft altitude	307	84.33	339.1	145.9	65.08	271.4	52%	23%	20%
9	Weight and C.G.	338.9	89.9	326.5	127	54.67	272.2	63%	39%	17%

For turning flight conditions, a more useful maneuver to evaluate robustness would be a roll type of maneuver. A generic roll stick doublet is shown in Figure 35, where the doublet starts at 35 seconds and ends at 41 seconds. Figure 36 shows the resulting swashplate inputs during the generic roll doublet maneuver. Figure 37 shows the roll doublet 4/rev magnitude response for 3 different flight conditions: black corresponds to nominal straight level flight at 120 kts, red corresponds to turning flight with a 4 deg bank angle, and blue corresponds to turning flight with a 10 deg bank angle. For all 3 flight condition cases, the response is presented with no vibration controller (solid lines) and with the fixed-gain integrated flight and vibration controller active (dashed lines). The fixed-gain vibration controller again is designed using the nominal, straight and level flight condition, but the same controller is used in both nominal and turning flight conditions.

Table 9 shows the average 4/rev magnitude RMS, STD, and peak-to-peak (P2P) values for each off design case. The values are listed for HHC and no HHC, and also the HHC percent improvement is shown, which allows off-design cases to be compared with the nominal design HHC percent improvement. For example, for the nominal conditions, the fixed-gain HHC improves average RMS by 53%, STD by 25%, and peak-to-peak by 26%. At 4 deg bank angle turning flight conditions, the fixed-gain HHC (designed at straight level flight) improves average RMS by 65%, STD by 46%, and peak-to-peak by 34%. One thing to note is that it may appear that the fixed-gain HHC actually performs better at 4 deg compared to nominal level flight when comparing the percentage improvements; however, this is due to the No-HHC case having significantly higher vibrations at 4 deg bank angle compared to nominal level flight conditions. When comparing the raw HHC RMS, STD, and peak-to-peak shows the fix-gain HHC does show small performance degradation. At 10 deg bank angle turning flight conditions, the fixed-gain HHC (designed at straight level flight) has larger performance degradation with the percent improvements at 44% for RMS, 13% for STD, and only 4% for peak-to-peak. Thus, for reasonable turning flight roll maneuvers, there is little effect on vibration reduction performance.

It is clear that both LTI and NL robustness evaluations indicate that there are gradual changes in HHC performance as flight speed and altitude deviate from the design conditions. Specifically, controller performance is satisfactory out to approximately +/- 20 kts, which corroborates previous literature (Ref. 40). Also, descending flight, turning flight, and alternate weight and C.G. location has very little impact on HHC performance.
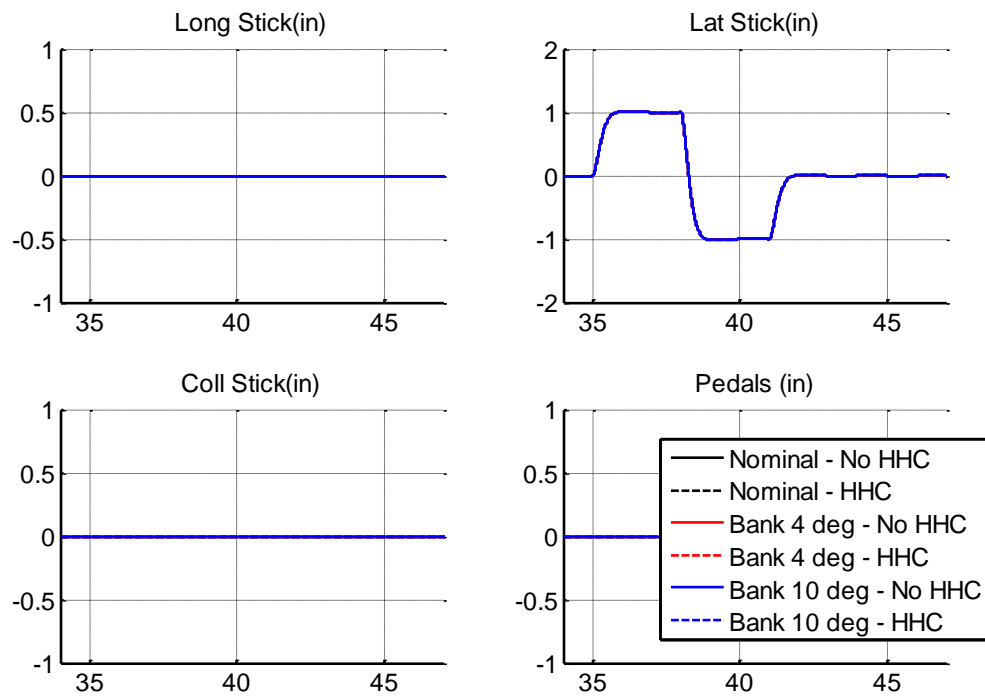
Figure 35. Roll Stick Doublet for Robustness Evaluations
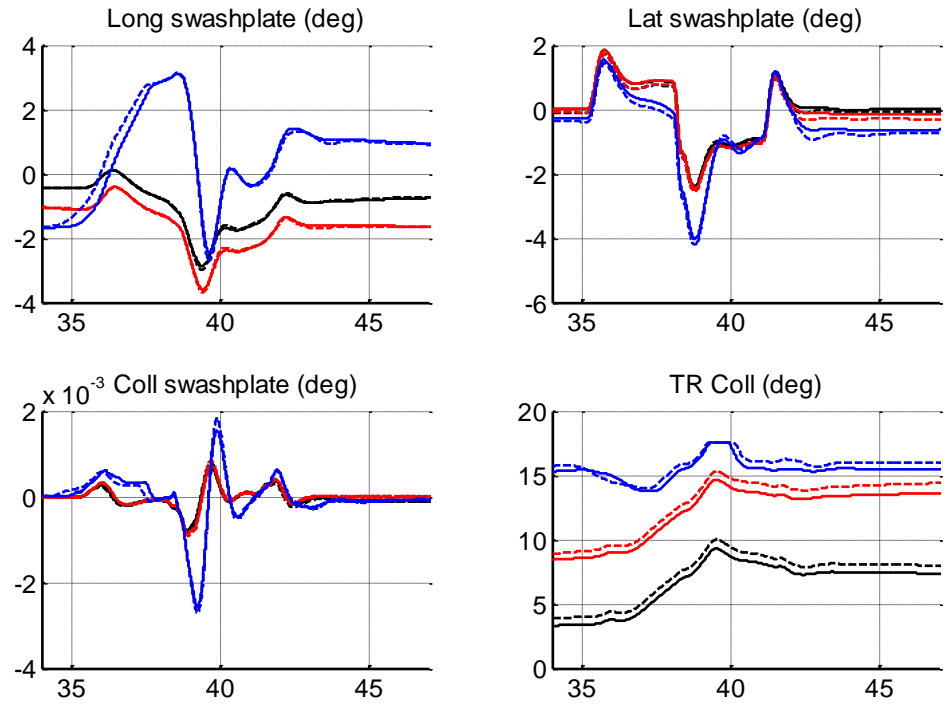
Figure 36. Roll Stick Doublet Resulting Swashplate Inputs
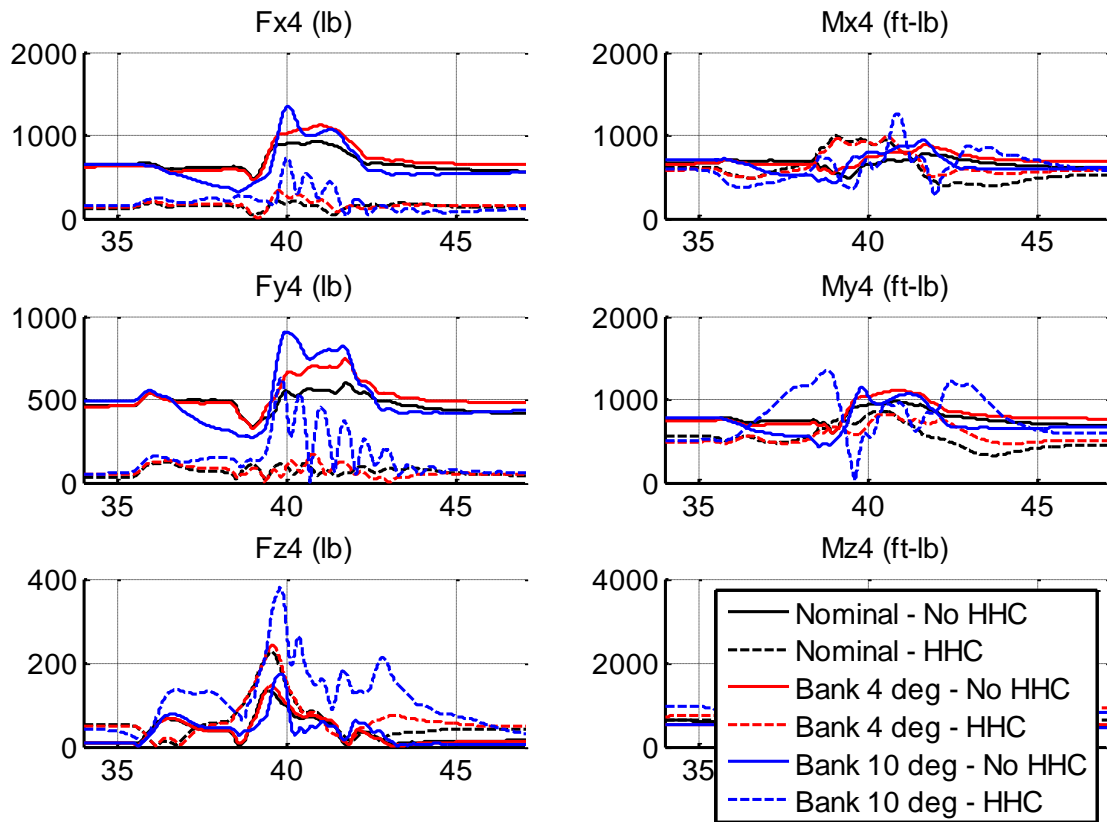
Figure 37. Doublet Response for Turning Flight Conditions

Table 9. Off Design Roll Doublet Performance

	4/rev Magnitude Average	Nominal	Bank 4 deg	Bank 10 deg
No HHC	RMS	229.2	323.6	305.8
	STD	44.83	66.26	93.82
	P2P	197.1	277.5	416.3
HHC	RMS	106.6	114.6	171.6
	STD	33.45	35.69	81.7
	P2P	146.7	182	431.8
HHC % Improvement	RMS	53%	65%	44%
	STD	25%	46%	13%
	P2P	26%	34%	4%

CHAPTER 7.FULL FLIGHT ENVELOPE CONTROLLER

Having conducted robustness evaluations using both LTI and NL models, it is clear that the integrated flight and vibration controller is robust to reasonable changes in descent, turning, as well as vehicle weight and C.G. location. There are gradual changes in controller stability and performance due to changes in speed and altitude. To address these changes, a full flight envelope controller was developed using controller scheduling techniques.

Based on the robustness evaluations, the controller performance is satisfactory out to approximately +/- 20 kts. Thus, the controller was scheduled with speed at every 40 kts – specifically 40, 80, and 120 kts were chosen as the scheduling anchor points (design points at which a particular controller is extracted for use in the scheduled controller). Based on the robustness evaluations, it is also suggested that the controller should be scheduled with altitude. This could likely be done by simply linearly scheduling with altitude, as Tobias and Tischler have demonstrated for the purposes of a model-stitched full flight envelope simulation (Ref. 42). However, the purpose here is to illustrate a methodology to develop a full flight envelope controller– not to actually provide a field-ready full flight envelope controller. Thus, although scheduling with altitude is suggested, here only speed was used for scheduling.

7.1 Additional Scheduling Anchor Points

To construct a scheduled full flight envelope controller, an integrated flight and vibration controller (including optimization and dynamic crossfeeds) were extracted at each scheduling anchor point. Since the initial integrated controller design was first done at a nominal design condition of 120 kts, the controller corresponding to the 120 kts anchor point was already complete. However, the integrated flight and vibration controllers were also needed at 40 and 80 kts.

At 40 and 80 kts, obtaining the integrated flight and vibration controllers was straightforward as one can simply repeat the process performed for extracting the 120 kts design. As demonstrated for 120 kts, the design procedure is as follows:

1) Trim the NL model about the design conditions (40 or 80 kts).

2) Generate a LTP model about the periodic equilibrium for which the NL model has been trimmed.

3) Construct an LTI approximation from the LTP model using the LTP in first order form as developed here.

4) If necessary for computational efficiency, formulate a reduced order LTI approximation. This can be done using modal participation or using state energy via Hankel Singular Values.

5) Extract a T-Matrix from the LTI model. Here the DC gain matrix is used as the T-Matrix which is consistent with interpretations of the T-Matrix from previous literature; however, other frequency points along the bode plot can also be chosen.

97

6) Use the LTI model and extracted T-Matrix in CONDUIT® to add dynamic compensation and optimize performance (broken-loop crossover frequency, DRB, DRP, and damping) while maintaining adequate stability margins.

7) Compute the ideal dynamic crossfeeds at various frequency points using the optimized HHC

8) Extract low order fits of the dynamic crossfeeds which can be implemented in the integrated flight and vibration controller.

This design procedure was followed with no issues for both 40 and 80 kts flight conditions.

To further demonstrate the effects of speed variations on the HHC, the baseline closed-loop T-Matrices are examined (without any optimization or dynamic crossfeeds) using roll doublet maneuvers. Table 10 shows the 4/rev average RMS, STD, and peak-to-peak (P2P) values of a roll doublet maneuver at a 80 kts flight speed using: no HHC, the T-Matrix extracted at 120 kts (extracted at 120 kts, but used here at 80 kts), and also the T-Matrix extracted at 80 kts (extracted and used here at 80 kts). At 80 kts flight condition, there is little improvement of the 80 kts design over the 120 kts design. This is likely due to the estimate of satisfactory controller performance within +/- 20 kts being a conservative estimate, and in actuality the HHC may have satisfactory performance outside of the +/- 20 kts estimate.

Table 10. 80 kts Roll Doublet T-Matrix Performance

	No HHC	T-Matrix 120 kts	T-Matrix 80 kts
4/rev RMS Average	160.6	21.7	19.2
4/rev STD Average	8.38	4.39	3.95
4/rev P2P Average	37.4	18.7	18.6
RMS Percent Improvement	-	86.5%	88.0%
STD Percent Improvement	-	47.6%	52.9%
P2P Percent Improvement	-	50.0%	50.3%

Table 11 shows the performance of a roll doublet maneuver at 40 kts flight speed using no HHC, the T-Matrix extracted at 120 kts (extracted at 120 kts, but used here at 40 kts), and also the T-Matrix extracted at 40 kts (extracted and used here at 40 kts). At such extreme deviations from the design conditions, the T-Matrix designed at 120 kts and used at 40 kts actually performs worse than having no HHC looking at transient performance measures of average STD and peak-to-peak. Although the actual raw values are small, the percent degradations are large, with 22.8% and 24.3% losses in performance for STD and peak-to-peak respectively. The T-Matrix designed and used at 40 kts performs as well as expected, having greatly improved percentage improvements of 72.7% for RMS, 44.7% for STD, and 37.4% for peak-to-peak.

Figure 38 shows the time response of the 4/rev magnitudes for the roll doublet maneuver at 40 kts. It is clear that the T-Matrix designed at 120 kts has very poor closed-loop transient response at 40 kts flight condition, as indicated by the dashed black line. The case with the T-Matrix designed at 120 kts has very large oscillations, likely due to poor damping and stability, which results in the poor STD and peak-to-peak performance from as seen in Table 11. It should also be noted that similar to the 120 kts design

evaluated at 120 kts (Figure 18), not all steady state vibration levels are improved for the

40 kts design evaluated at 40 kts. Specifically, for the 40 kts design in , Mx4 is allowed

to have increased steady state loads to allow for an overall improvement.

Table 11. 40 kts Roll Doublet T-Matrix Performance

	No HHC	T-Matrix 120 kts	T-Matrix 40 kts
4/rev RMS Average	80.5	26.5	22.0
4/rev STD Average	3.47	4.26	1.92
4/rev Peak to Peak Average	13.6	16.9	8.52
RMS Percent Improvement	-	67.1%	72.7%
STD Percent Improvement	-	-22.8%	44.7%
P2P Percent Improvement	-	-24.3%	37.4%
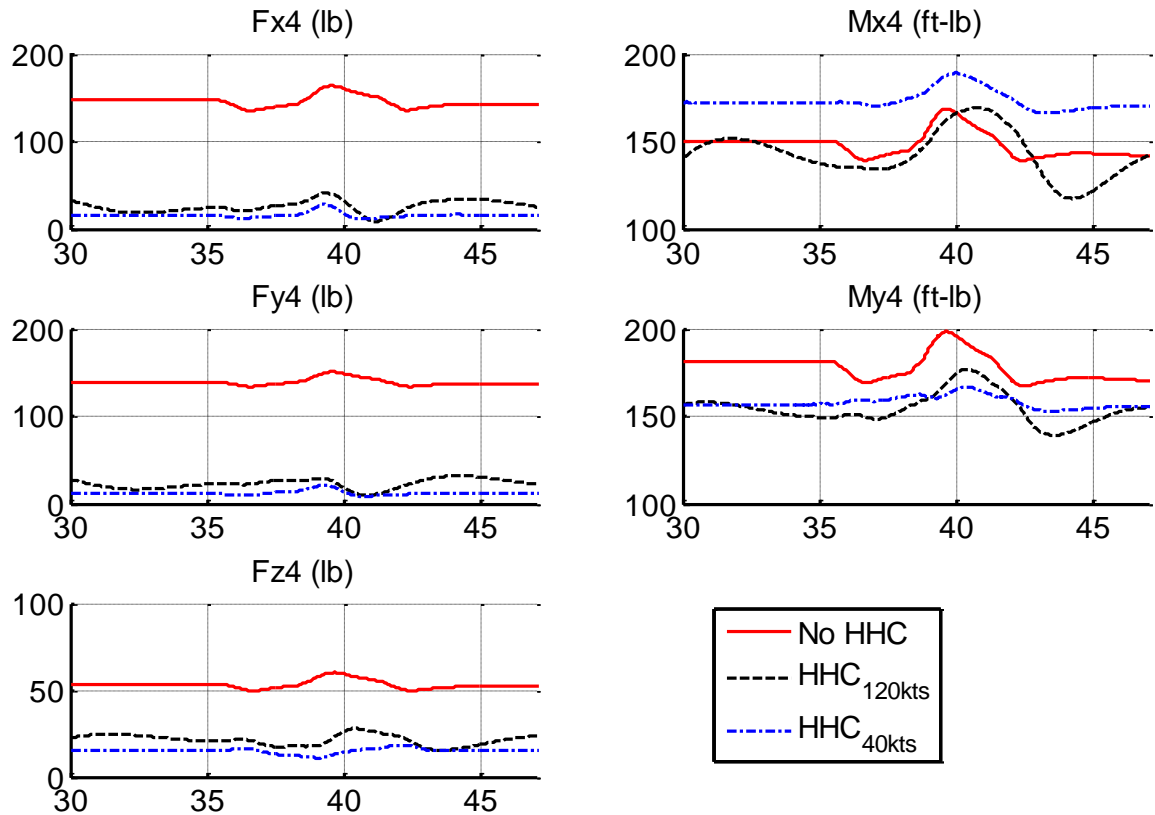
Figure 38. Roll Doublet Response at 40 kts Flight Speed

The integrated flight and vibration controllers (optimized with dynamic crossfeeds) were extracted at all 3 scheduling anchor points: 40, 80, and 120 kts. With the anchor points complete, each controller was then used in a scheduler to form the full flight envelope integrated flight and vibration controller. The way this was accomplished was using discrete controller scheduling. Discrete controller scheduling switches between entire anchor point controllers. This is in contrast to a continuous controller schedule, where controller gains are simply interpolated between anchor points. A discrete controller schedule is used due to issues with scheduling the dynamic crossfeeds

which are implemented are low order approximations of the ideal crossfeeds. While the ideal crossfeeds may smoothly vary with flight condition, the low order approximations may not be smoothly varying and can change structure, yielding interpolated controllers that may have no meaning. A discrete controller schedule avoids this issue as the controllers are not interpolated.

To implement the discrete controller schedule, only the controller with the anchor point nearest to the current speed is active. Specifically, the controller designed at 40 kts is active when the vehicle is below 60 kts, the controller designed at 80 kts is active when the vehicle is between 60 and 100 kts, and the controller designed at 120 kts is active when the vehicle is above 100 kts. It is also suggested that a hysteresis loop be added to avoid issues when the vehicle is operating close to the switching points. No issues with controller switching were observed during this work, but a hysteresis loop would help to alleviate any issues with switching should they arise.

Furthermore, it should be noted that all 3 controllers (40, 80, and 120 kts) are actually continuously running; however, each controller only receives inputs when the vehicle is within the activation envelope of that particular controller. This is in contrast to other discrete controller strategies, where either 1) all controllers receive the total input, and the controller outputs are interpolated, or 2) the inputs to controllers are interpolated, and the outputs of the controller are summed. All of these strategies were explored, and having only one controller receiving the entire input at any given moment was found to be the simplest and have the best performance.

At this point, a full flight envelope integrated flight and vibration controller has been developed and has been examined at each of the 3 design anchor points. However,

to fully examine the full flight envelope performance, a maneuver which covers the full flight envelope is necessary.

7.2 Full Flight Envelope Evaluation

To demonstrate the full flight envelope performance of the scheduled controller, a realistic maneuver is constructed based on the ADS-33 roll reversal MTE (Ref. 37). The standard ADS-33 roll reversal maneuver is a pullup/pushover maneuver followed by a roll and then back to level flight. The standard roll reversal maneuver however has two issues that require attention for the purposes of demonstrating full flight envelope performance. First, although the pullup/pushover maneuver phase subjects the vehicle to a wide range of speeds, the roll phase of the maneuver occurs after the pullup/pushover phase. To evaluate the roll performance of the full flight envelope controller, the roll maneuver must occur simultaneously with changes in speed. Secondly, the pullup/pushover that was previously examined here subjects the vehicle to a flight speed range of approximately 80 to 120 kts. As shown in the evaluation of the 80 kts anchor point design, the 120 kts anchor point design may actually have satisfactory performance at 80 kts. Thus, to show the full performance of the scheduled controller, it is desirable to lower the range of flight speed to reach the 40 kts anchor point.

To address issues with the standard ADS-33 roll reversal MTE, a modified roll reversal maneuver is constructed for the evaluation of the full flight envelope controller evaluation. First, the previously used pullup/pushover maneuver is used as a starting point. Next, the pilot inputs are extended to cover approximately 40 to 120 kts speeds during the entire maneuver. For the standard pullup/pushover maneuver, the pilots

tended to use most of the control authority nearly saturating the pitch stick inputs. Rather than increasing the magnitude of inputs and saturating the pilot authority, the duration of inputs is extended by 65% (pilot inputs are stretched over an additional 65% of time). This duration increase subjects the vehicle to speeds ranging from 40 to 120 kts during the maneuver. Next, the generic roll doublet is superimposed during the pushover phase. Thus, the pushover and roll doublet actually occur at the same time. The roll doublet is added during the pushover phase to avoid large deviations during the latter portions of the maneuver (i.e., despite the roll doublet, the vehicle returns back to level at the end of the maneuver without additional modification of the pilot inputs). It should be noted that although the entire maneuver covers 40 to 120 kts, the roll portion of the maneuver covers only 40 to 80 kts.

The resulting maneuver is referred to as the "modified roll reversal maneuver" and has the following key features:

1) Based on ADS-33 roll reversal MTE which is representative of realistic maneuvers.

2) Generated from realistic piloted inputs.

3) Excites both longitudinal and lateral dynamics via the pullup/pushover and roll reversal portions respectively.

4) Covers a wide range of flight speeds from 40 to 120 kts.

The modified roll reversal maneuver is examined for 3 cases: with no HHC, with the fixed-point HHC (fixed at the 120 kts design – optimized with dynamic crossfeeds), and with the full flight envelope HHC (scheduled, optimized, and with dynamic crossfeeds). The pilot inputs are shown in Figure 39. The maneuver starts at 41 seconds,

and completes at 75 seconds when the vehicle is back to level. The roll doublet portion starts at 50 seconds and completes at 58 seconds. The HHC inputs are shown in Figure 40. The No HHC case is shown in solid red lines, the HHC Fixed at the 120kts design is shown in black dashed lines, and the scheduled HHC is shown in blue dashed-dotted lines. The HHC is turned on at 20 seconds to allow the HHC to reach a steady state before the maneuver starts.

Translational speed response is shown in Figure 41. The vehicle starts at 120 kts, slows down to 40 kts during the pullup portion, and then accelerates back up to 80 kts during the pushover portion before leveling out. Figure 42 shows the attitude and attitude rate response with the vehicle reaching 45 deg in pitch attitude and 25 deg in roll attitude. Figure 43 shows the load factor, with the vehicle being subjected to a high load factor during the pullup portion followed by a low load factor during the pushover portion. Similar to the pullup/pushover maneuver, again it can be seen that the addition of scheduled HHC, optimized with dynamic crossfeeds has little impact on the body response and needs little or no compensation by the pilot inputs and AFCS design.

Figure 44 shows the 4/rev weighted amplitude response, with Figure 45 showing a zoom in of the 4/rev weighted amplitude response to better illustrate the HHC cases. From Figure 44, it is clear that both HHC cases perform better than compared to No HHC, with both HHC cases being mostly below the No HHC case. From Figure 45, it is clear that the scheduled HHC does consistently better than the 120 kts fixed-design HHC. Table 12 shows the performance measures of 4/rev amplitude average RMS, STD, and peak-to-peak as well as the percentage improvements for both HHC designs over the No HHC case. The HHC using a fixed-point, 120 kts design does considerably well, having

a 52% improvement in average RMS, 50% improvements in average STD, and 42% improvement. Scheduling further improves performances by an additional 5% for RMS, 8% for STD, and 11 % for peak-to-peak. Thus the full flight envelope controller clearly outperforms the fixed-point controller design for the maneuver considered here.
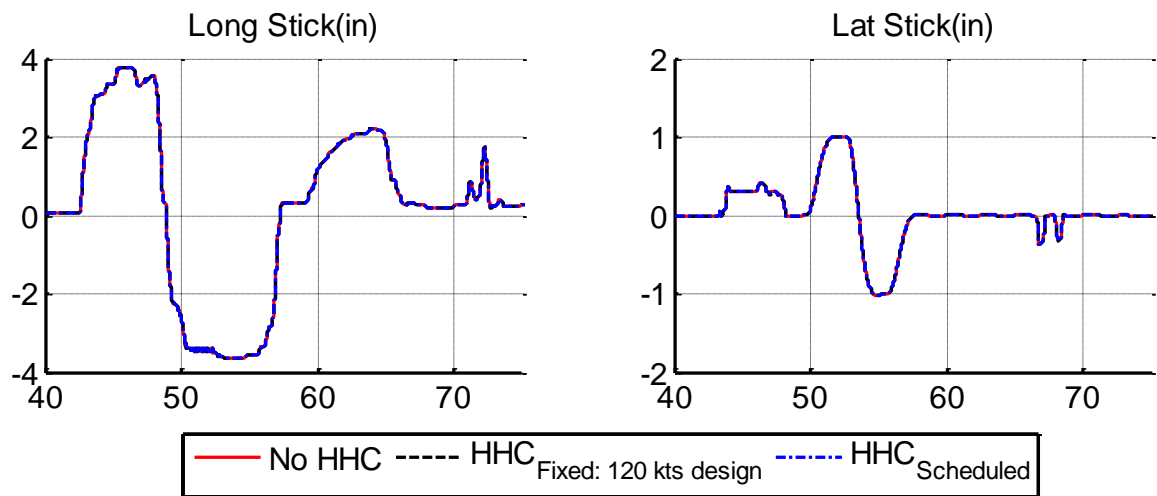
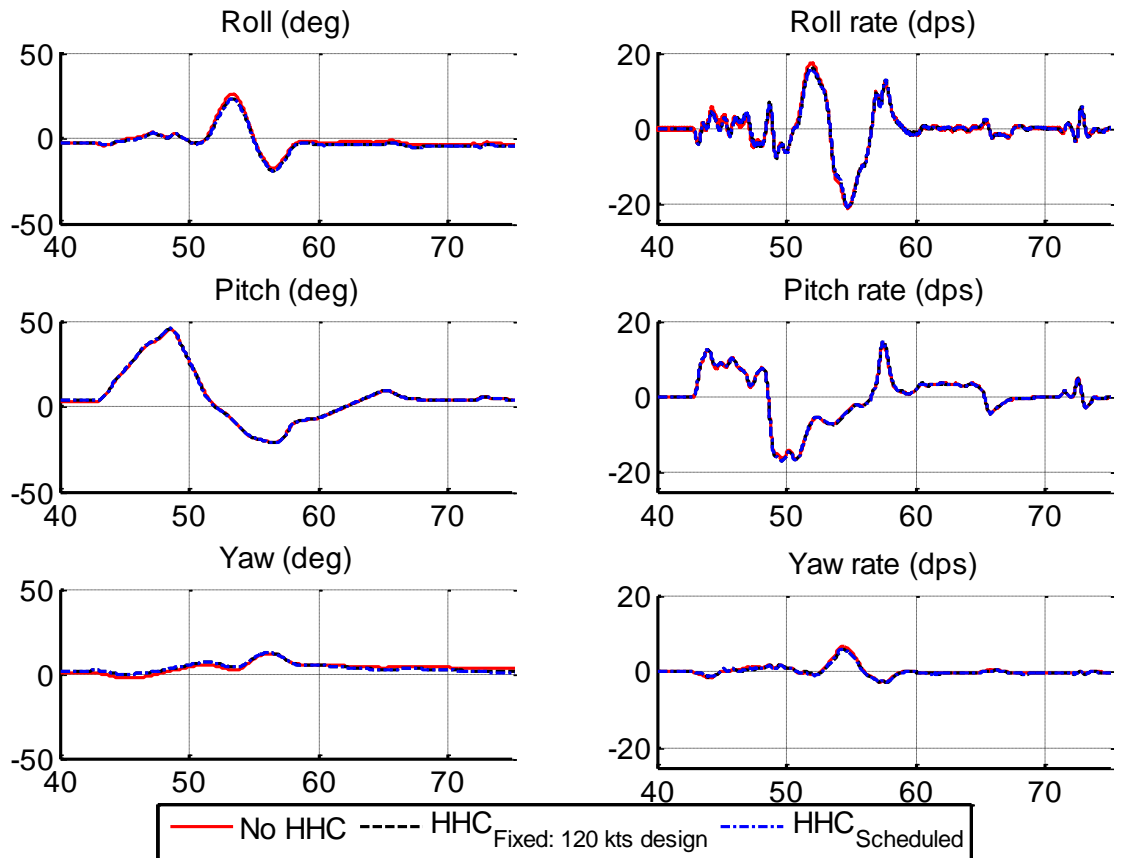**Figure 39. Modified Roll Reversal Pilot Inputs**
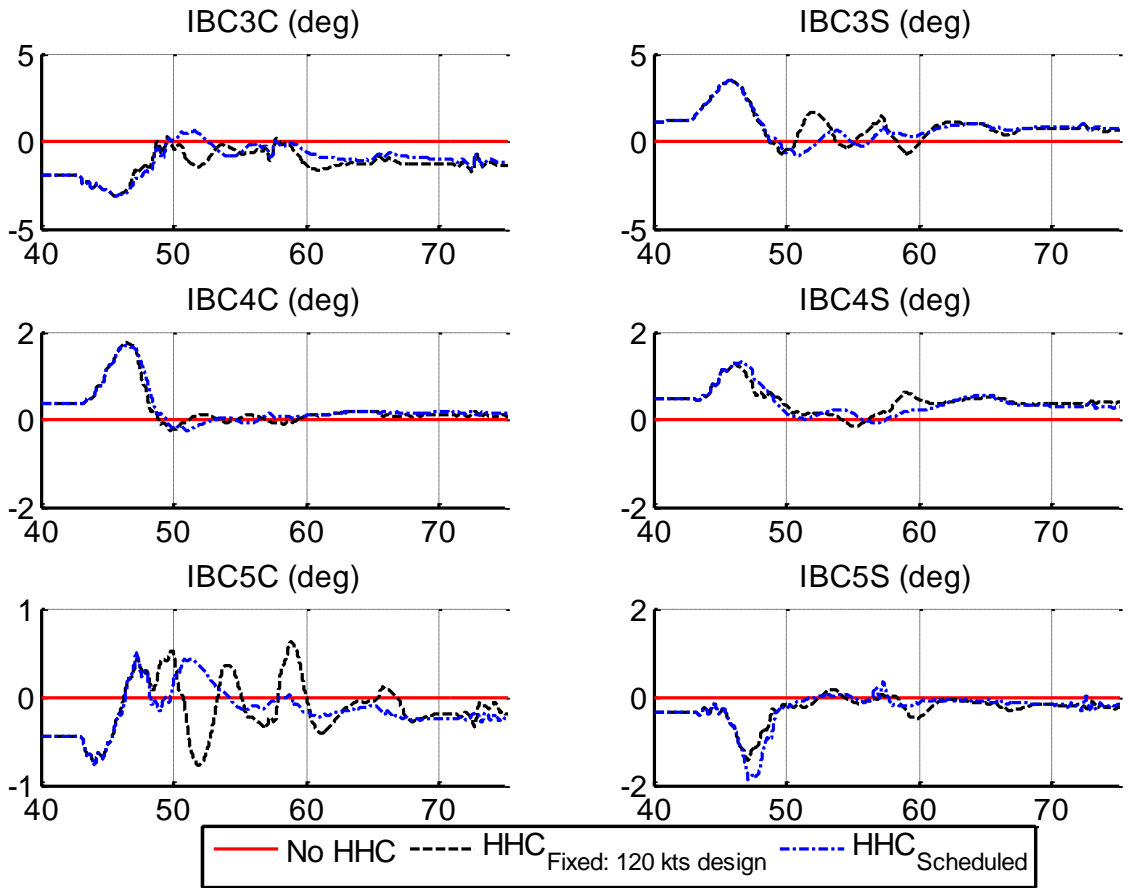
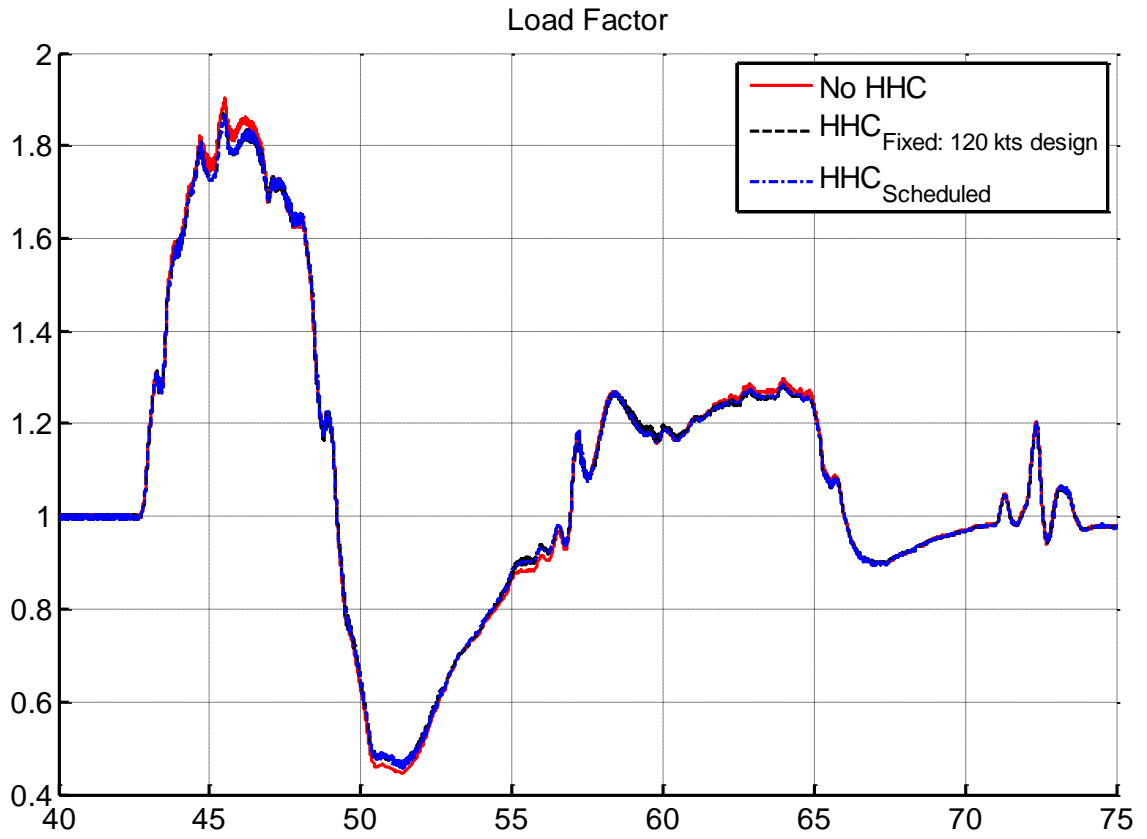**Figure 40. Modified Roll Reversal Higher Harmonic Control Inputs**
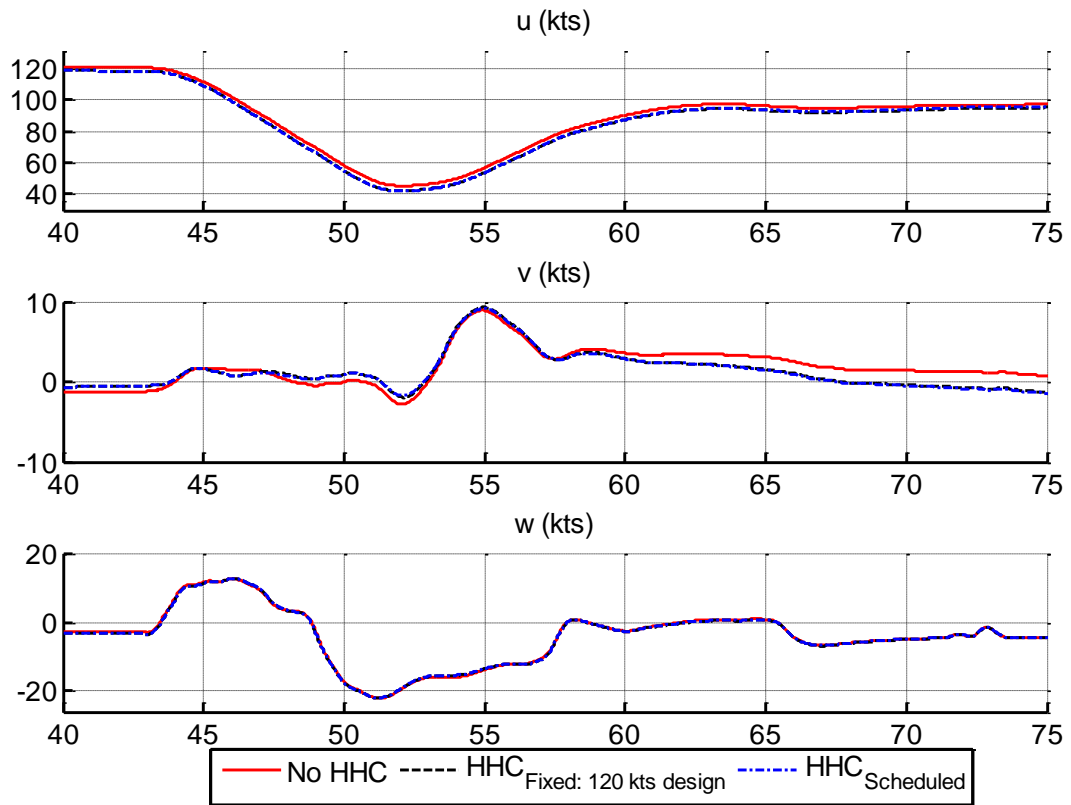
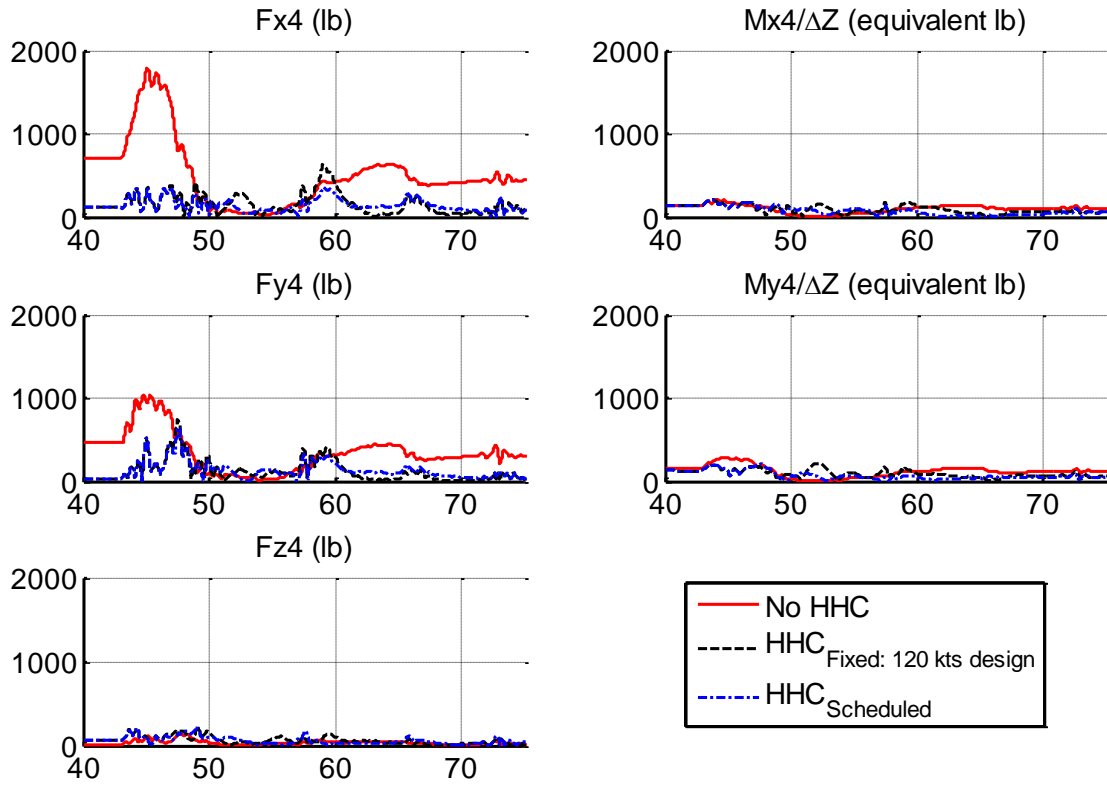**Figure 41. Modified Roll Reversal Translation Speed Response**

Figure 42. Modified Roll Reversal Attitude and Attitude Rate Response

Figure 43. Modified Roll Reversal Load Factor Response

Figure 44. Modified Roll Reversal 4/rev Amplitude Response
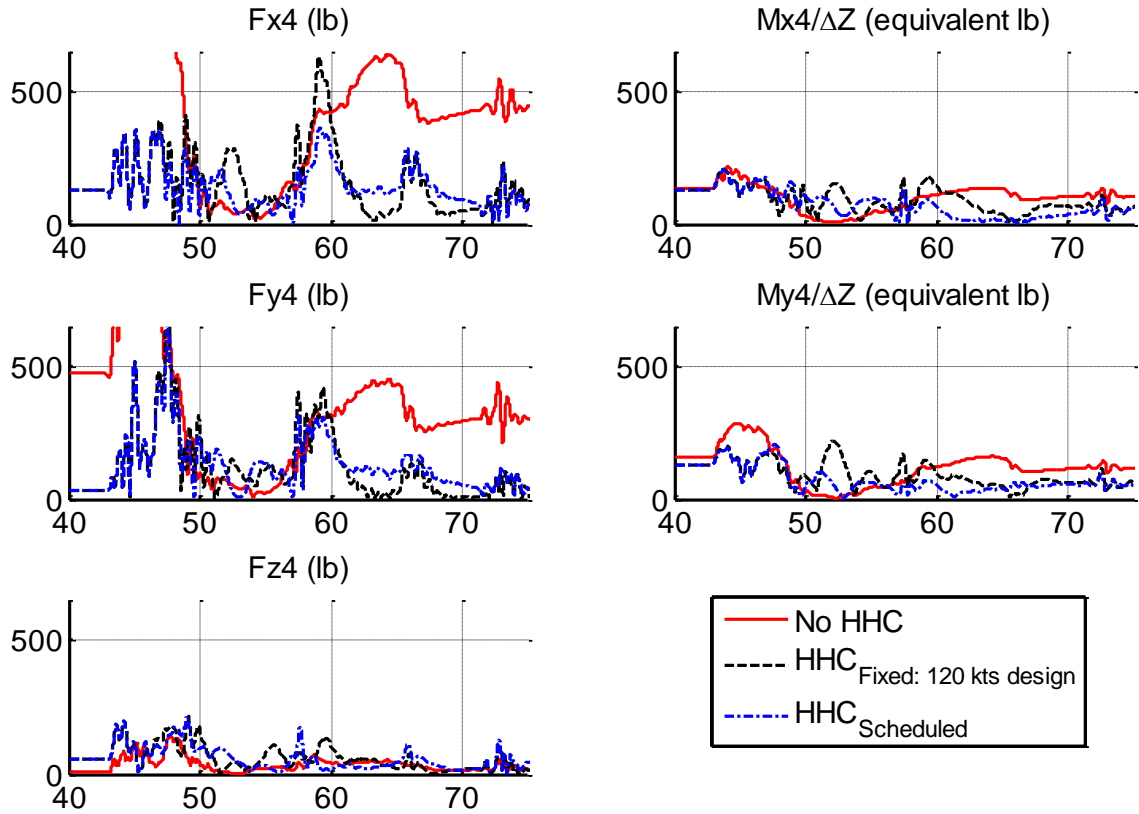
Figure 45. Modified Roll Reversal 4/rev Amplitude Response (Zoom In)

Table 12. Modified Roll Reversal Performance

Pullup/Pushover	No HHC	HHC Fixed Point 120 kts Design	HHC Scheduled
4/rev RMS Average	273.0	130.8	115.3
4/rev STD Average	156.6	77.30	64.70
4/rev Peak to Peak Average	686.7	400.5	324.6
4/rev RMS Average Percent Improvement	-	52.08%	57.76%
4/rev STD Average Percent Improvement	-	50.63%	58.68%
4/rev Peak to Peak Average Percent Improvement	-	41.67%	52.73%

CHAPTER 8. CONCLUSIONS AND RECOMMENDATIONS

A generalized linear time invariant (LTI) approximation is developed from a linear time periodic (LTP) model using a first order formulation for the LTP system. Explicit formulas for LTI state space matrices are presented. A complete numerical example is given for a generic UH-60A rotorcraft configuration. The resulting LTI is validated against the original nonlinear model, and is shown to be very accurate in the frequency domain. The modal participation is calculated directly from the LTI and compared with modal participation calculated from the LTP. Modal participation, additive uncertainty, and nu-gap metric analysis are used to evaluate the significance of particular harmonic terms. The LTI model is then used for vibration control design and optimization. Dynamic crossfeeds are constructed to formulate an integrated flight and vibration controller. The integrated flight and vibration controller is evaluated for performance using generic and realistic piloted maneuvers in a nonlinear simulation. The robustness of the integrated controller is evaluated and a full flight envelope controller is designed and evaluated.

8.1 Conclusions

The results presented here support the following conclusions:

1) A nonlinear time periodic rotorcraft model can be accurately approximated by a linear time invariant model, using harmonic decompositions and a first order representation.

2) Modal participation can be accurately and easily obtained from a linear time invariant approximation, avoiding ambiguities of obtaining modal participation from the linear time periodic model.

3) Body and inflow degrees of freedom have harmonic terms with significant modal participation. For the 4 bladed rotor considered here, body, inflow, and rotor harmonic terms with the highest modal participation are harmonics numbered 0, 1, 2, 4, 6, and 8.

4) Coupling of harmonic terms for body, inflow, and rotor degrees of freedom have a significant role in the input-output fidelity for the purpose of predicting vibratory loads.

5) Using Hankel Singular Values, a linear time invariant model can be significantly reduced to less than 100 states while maintaining adequate accuracy for the purpose of CONDUIT® optimization of vibration controllers.

6) HHC has little impact on body response and needs little or no compensation by pilot inputs and AFCS design for the realistic piloted maneuvers considered here.

7) Optimized HHC design improves average RMS by 59%, STD by 50%, and peak-to-peak 4/rev loads by 27% for the pullup/pushover maneuver considered here.

8) Ideal crossfeeds can be accurately represented using low-order approximations.

9) As compared to a no crossfeed design, a crossfeed design improved average RMS by 5%, STD by 15%, and peak-to-peak 4/rev loads by 24% for the pullup/pushover maneuver considered here.

10) HHC performance gradually varies with speed and altitude, but is robust to turning maneuvers, weight and C.G. changes, and descent rate.

11) Controller scheduling can be used to create a full flight envelope integrated flight and vibration controller.

12) As compared to no scheduling, a scheduled HHC design further improved average RMS by 5%, STD by 8%, and peak-to-peak 4/rev loads by 11% for the modified roll reversal maneuver considered here.

8.2 Recommendations

The following are recommendations for future work:

1) Application of the LTI methodologies developed here for advanced configurations such as compound coaxial rotorcraft which have added complexity and travel at much higher speeds.

2) Application of the LTI methodologies developed here for estimator design such as for hub load harmonics estimation or rotor state estimation. The delay associated with the harmonic estimator is thought to be the largest limitation for improving HHC performance; addressing the harmonic estimator delay will allow for larger HHC improvements.

3) Consideration of HHC methodologies developed here for other purposes such as performance, BVI reduction, noise reduction, or coaxial rotor tip clearance.

4) Consideration of the HHC methodologies developed here combining LTI model with online identification of T-Matrix and real-time HHC control updates. Inclusion of realistic identification issues such as noise and limitations on inputs used for identification.

REFERENCES

[1]Friedmann, P.P. and Millott, T.A., "Vibration Reduction in Rotorcraft Using Active Control: A Comparison of Various Approaches," *Journal of Guidance, Control, and Dynamics*, Vol. 18, No. 4, 1995.

[2]Teves, D., Niesl, G., Blaas, A., and Jacklin, S., "The Role of Active Control in Future Rotorcraft," Proceedings of the 21st European Rotorcraft Forum, Saint-Petersburg, Russia, August 30 – September 1, 1995.

[3]Nguyen, K., Betzina, M., and Kitaplioglu, C., "Full-Scale Demonstration of Higher Hamonic Control for Noise and Vibration Reduction on the XV-15 Rotor," American Helicopter Society 56th Annual Forum Proceedings, Virginia Beach, Virginia, May 2-4, 2000.

[4]Friedmann, P.P., "Rotary-Wing Aeroservoelastic Problems," AIAA Paper 92-21070, April 1992.

[5]Arnold, U.T.P. and Strecker, G., "Certification, Ground and Flight Testing of an Experimental IBC System for the CH-53G Helicopter," American Helicopter Society 58th Annual Forum Proceedings, Montreal, Canada, June 11-13, 2002.

[6]Kessler, C., Fuerst, D., and Arnold, U.T.P., "Open Loop Flight Test Results and Closed Loop Status of the IBC System on the CH-53G Helicopter," American Helicopter Society 59th Annual Forum Proceedings, Phoenix, Arizona, May 6-8, 2003.

[7]Wood, E.R, Powers, R.W, Cline, J.H, and Hammond, C.E., "On Developing and Flight Testing a Higher Harmonic Control System," *Journal of the American Helicopter Society,* Vol. 30, No. 1, pp.3-20(18), 1 January 1985.

[8]Cheng, R.P., Tischler, M.B., and Celi, R., "A High-Order, Time Invariant Linearized Model for Application to HHC/AFCS Interaction Studies," American Helicopter Society 59th Annual Forum Proceedings, Phoenix, Arizona, May 6-8, 2003.

[9]Abraham, M.D., Olcer, F.E., Costello, M.F., Takahashi, M.D., and Tischler, M.D., "Integrated Design of AFCS and HHC for Rotorcraft Vibration Reduction using Dynamic Crossfeeds," American Helicopter Society 67th Annual Forum Proceedings, Virginia Beach, Virginia, May 3-5, 2011.

[10]Floquet, G., "Sur les équations différentielles linéaires à coefficients périodiques," *Annales scientifiques de l'École Normale Supérieure,2ᵉ* série (tome 12), 1883, pp. 47-88.

[11]Peters, D.A. and Lieb, S.M., "Significance of Floquet Eigenvalues and Eigenvectors for the Dynamics of Time-Varying Systems," American Helicopter Society 65th Annual Forum Proceedings, Grapevine, Texas, May 27-29, 2009.

[12]Varga, A. and Van Dooren, P., "Computational methods for periodic systems – an overview," Proceedings of IFAC Workshop on Periodic Control Systems, Como, Italy, 2001.

[13]Bittanti, S. and Colaneri, P., "Invariant Representations of discrete-time periodic systems," Automatica, Volume 36, Issue 12, December 2000, pp. 1777-1793.

[14]Varga, A., "An Overview of Recent Developments in Computational Methods for Periodic Systems," Proceedings of the 3rd IFAC Workshop on Periodic Control Systems, St. Petersburg, Russia, 2007.

[15]Lovera, M., Colaneri, P., Malpica, C., and Celi, R., "Discrete-Time Closed-Loop Aeromechanical Stability Analysis of Helicopters with Higher Harmonic Control," American Helicopter Society 60th Annual Forum Proceedings, Baltimore, Maryland, June 7-10, 2004.

[16]Celi, R., Lovera, M., Colaneri, P., and Bittanti, S., "Control of Systems with Periodic Coefficients with Application to Active Rotor Control," Contract Number DAAD19-01-1-0415, Project Number 41569-EG, Final Report, University of Maryland, College Park, Maryland, June 30, 2004.

[17]Hill, G.W., "Mean Motion of Lunar Perigee," *Acta Matematica¸* Vol. 8, January 1886.

[18]Crimi, P., "A Method for Analyzing the Aeroelastic Stability of a Helicopter Rotor in Forward Flight," NASA CR-1332, August 1969.

[19]Piarulli, V. J. and White, R. P., Jr., "A Method for Determining the Characteristic Functions Associated with the Aeroelastic Instabilities of Helicopter Rotor Blades in Forward Flight," NASA CR-1577, June 1970.

[20]Prasad, J.V.R., Olcer, F.E., Sankar, L,N. and He, C., "Linear Models for Integrated Flight and Rotor Control," Proceedings of the 34th European Rotorcraft Forum, Birmingham, UK, September 16-18, 2008.

[21]Prasad, J.V.R., Olcer, F.E., Sankar, L.N., and He, C., "Linear Time Invariant Models for Integrated Flight and Rotor Control," Proceedings of the 35th European Rotorcraft Forum, Hamburg, Germany, September 22-25, 2009.

[22]Olcer, F.E., *Linear Time Invariant Models for Integrated Flight and Rotor Control*, Doctor of Philosophy Thesis, Georgia Institute of Technology, July 2011

[23]Olcer, F.E and Prasad, J.V.R., "A Methodology for Evaluation of Coupled Rotor-Body Stability using Reduced Order Linear Time Invariant (LTI) Models," American Helicopter Society 67th Annual Forum Proceedings, Virginia Beach, Virginia, May 3-5, 2011.

[24]Padthe, A.K., Friedmann, P.P., Lopez, M., and Prasad, J.V.R., "Analysis of High-Fidelity Reduced-Order Linearized Time-Invariant Helicopter Models for Integrated Flight and On-Blade Control Applications," Proceedings of the 41st European Rotorcraft Forum, Munich, Germany, September 1-4, 2015.

[25]Advanced Rotorcraft Technology, Inc., "FLIGHTLAB Theory Manual (Vol. I)," March 2004.

[26]Tischler, M.B. and Remple, R. K., *Aircraft and Rotorcraft System Identification: Engineering Methods with Flight Text Examples*, 2nd Edition, Amerian Institute of Aeronautics and Astronautics, Inc., Reston, VA, 2012, pp. 332-333.

[27]Mohan, R. and Gaonkar, G.H., "A Unified Assessment of Fast Floquet, Generalized Floquet, and Periodic Eigenvector Methods for Rotorcraft Stability Predictions," *Journal of The American Helicopter Society*, Vol. 58, No. 4, June 2013.

[28]Mohan, R. and Gaonkar, G.H., "Mode Identification by Floquet-Eigenvector and Approximate Methods Including Comparisons with Aeromechanical Stability Measurements," American Helicopter Society 67th Annual Forum Proceedings, Virginia Beach, Virginia, May 3-5, 2011.

[29]Zhou, K. and Doyle, J., *Essentials of Robust Control*, Prentice Hall, Upper Saddle River, NJ, 1998, pp. 142-143.

[30]Vinnicombe, G., *Measuring the Robustness of Feedback Systems*, Doctor of Philosophy Dissertation, University of Cambridge, 1992.

[31]Tischler, M.B., Ivler, C. M., Mansur, M. H., Cheung, K. K., Berger, T., and Berrios, M., "Handling-Qualities Optimization and Trade-offs in Rotorcraft Flight Control Design," in Presented at the RAeS Rotorcraft Handling-Qualities Conference, University of Liverpool, U.K., 4-6 Nov 2008.

[32]Kenney, C. and Hewer, G., "Necessary and Sufficient Conditions for Balancing Unstable Systems," IEEE Transactions on Automatic Control, Vols. AC-32, no. No. 2, pp. 157-160, February 1987.

[33]Chen, R. T. and Hindson, W. S., "NASA-TM-88327 Influence of Dynamic Inflow on the Helicopter Veritcal Response," Ames Research Center, Moffett Field, CA, June 1986.

[34]Nguyen, K. and Chopra, I., "Effects of Higher Harmonic Control on Rotor Performance and Control Loads," *Journal of Aircraft*, Vol. 29, No. 3, May-June 1992.

[35]Tischler, M. B., Fletcher, J. W., Morris, P. M., and Tucker, G. E., "Flying Quality Analysis and Flight Evaluation of a Highly Augmented Combat Rotorcraft," Journal of Guidance, Control, and Dynamics, vol. 14, no. 5, pp. 954-963, 1991.

[36]Mansur, M.H and Tischler, M. B., "Flight Test Comparison of Alternate Strategies for Multi-Loop Control Law Optimization," American Helicopter Society 69th Annual Forum Proceedings, Phoenix, Arizona, May 21-23, 2013.

[37]"Handling Qualities Requirements for Military Rotorcraft," Aeronautical Design Standard-33 (ADS-33E-PRF), US Army Aviation and Missile Command, March 21, 2000.

[38]Yamakawa, G. M., Broadhurstm D. G., and Smith, J. R., "AD902767 Utility Tactical Transport Aircraft Systems (UTTAS) Maneuver Criteria," US Army Aviation Systems Test Activity, Edwards Air Force Base, California, 1972.

[39]Studebaker, K. "A Survey of Hub Vibration for the UH-60A Airloads Research Aircraft," American Helicopter Society Aeromechanics Specialists Confrence, San Francisco, CA, January 19-21, 1994.

[40]Patt, D. and Liu, L., Chandrasekar, J., Bernstein, D. S., and Friedmann, P.P.,, "Higher-Harmonic-Control Algorithm for Helicopter Vibration Reduction Revisited," *Journal of Guidance, Control, and Dynamics*, Vol. 28, No. 5, 2005.

[41]Fan., F. H. and Hall, S. R., "Gain-Scheduled Higher Harmonic Control for Full Flight Envelope Vibration Reduction," American Helicopter Society 70th Annual Forum Proceedings, Montreal, Quebec, Canada, May 20-22, 2014.

[42]Tobias, E. L. and. Tischler, M. B., "A Model Stitching Architecture for Continuous Full Flight-Envelope Simulation of Fixed-Wing Aircraft and Rotorcraft from Discrete Model Points," Technical Memorandum, U.S. Army Aviation Development Directorate – AFDD, Moffett Field, CA, May 19, 2015.

VITA

Mark Joseph Santos Lopez was born in Anaheim, California on October 30, 1989. He received his Bachelor of Science Degree in Aerospace and Mechanical Engineering at the University of California, Irvine in 2011. He was accepted to the School of Aerospace Engineering at the Georgia Institute of Technology in 2011. He received his Master of Science Degree in Aerospace Engineering at the Georgia Institute of Technology in 2014. He is actively involved in the U.S. Army sponsored Vertical Lift Research Center of Excellence (VLRCoE), collaboration work with the U.S. Army Aviation Development Directorate – AFDD at NASA Ames, and also the Georgia Tech Rotorcraft Flight Simulation Laboratory. He is a student member of the American Helicopter Society.